Politecnico di Torino

Unraveling the properties of defective WS_2 monolayers in a controlled gas atmosphere: a theoretical study

Master degree in Nanotechnologies for ICTs

Author: Michele Giovanni Bianchi

Supervisor: Giancarlo Cicero,

Co-supervisors: Michele Re Fiorentin, Francesca Risplendi

A.Y. 2021-2022

Abstract

Two-dimensional materials are emerging as the ideal candidates for innovative electronic and optoelectronic devices, since they intrinsically push the scaling process down to the atomic level, overcoming common technological limits. Among the plethora of two-dimensional materials, Transition Metal Dichalcogenide (TMD) monolayers, such as the direct-bandgap semiconducting WS_2, have been intensively studied since they exhibit a unique combination of atomic-scale thickness, optoelectronic and mechanical properties, resulting suitable for a wide range of applications. Moreover, Chemical Vapour Deposition (CVD) techniques allow for a fairly easy synthesis of large flakes. However, WS_2 properties are strongly influenced by the adsorption of chemical species in the surrounding environment due to the large surface-volume ratio in the monolayers. This process is enhanced in CVD samples due to the high defect density. Identifying the impact of adsorbed molecules on the material properties is fundamental for the design of effective technological applications since environmental conditions, such as humidity or the presence of oxidizing agents, can alter the performances in an unpredictable way. For that reason, this thesis focuses on *ab initio* Density Functional Theory (DFT) simulations of molecule adsorption on WS_2 monolayers, analysing the influence of defects in this process. Initially, the electronic properties of common unintentional defects, such as Cr as W substituent, O as S substituent and S vacancies, are analysed in order to identify their main geometrical and electronic features. Then, the adsorption of common gas molecules on the defect sites is studied to quantify the interaction strength and understand how the adsorbed molecules alter the characteristics of the system. According to simulations, molecular oxygen results to have the major influence on the material properties among the different analysed gases. Physisorption is the most common process also in presence of defects, but O_2 chemisorption can also occur on the S vacancy site. The main effects of the latter process are the local decrease of the band gap value and the passivation of the in-gap defect states that mediate non-radiative recombination mechanisms. Hence, the O_2 interaction has also beneficial effects in view of the photon emission enhancement. For that reason, the accidental gas exposure and a partial material oxidation can become an intentional strategy to passivate the reactive sites of the S vacancies and 'repair' the flakes.

Acknowledgments

I would like to thank Professor Giancarlo Cicero, Dr. Michele Re Fiorentin and Dr. Francesca Risplendi for their support, kindness and patience. Our discussions have always increased my knowledge and stimulated my scientific critical thinking.
Moreover, I am also thankful to Mattia Salomone, Federico Raffone and Clara Salvini for their advice during this period.
Finally, I wish to extend my special thanks to my parents and my sister for their understanding and support during all my studies.

Computational resources were provided by the High Performance Computing department of CINECA under the Iscra initiative.

Contents

Introduction

The development of innovative solutions for electronic and optoelectronic devices is one of the most important challenges in the ICT sector which calls for the search of new architectures and materials with superior physical properties. In particular, some commonly employed devices, as silicon-based Field Effect Transistor (FET), show limitations associated to the scaling process that could be overcome by employment of novel low-dimensional materials. In the field of quantum information technologies, precision metrology and imaging applications, nanomaterials could be employed as new optical sources with high photon yield, high spectral purity and controllable emission of correlated photons. Graphene, but above all other 2D materials with semiconducting nature, could be effectively employed for such purposes. In the framework, Transition Metal Dichalcogenides (TMDs), such as WS_2, are appealing since they are materials which are stable at the monolayer atomic level, whose surfaces have no dangling bonds. At the same time, WS_2 can be synthesized in large flakes (edges larger than tens of μm) with commonly employed growth techniques such as chemical vapor deposition (CVD). WS_2 monolayer (ML) is a semiconductor with a direct band gap in the visible range (≈ 2 eV). Its electrical and optical properties can be tuned by defect engineering, resulting in an optimal material for optoelectronics. However, WS_2 features are strongly influenced by gas adsorption due to the large surface-volume ratio of the monolayers. Hence, WS_2 flakes, exposed to the environment gases, are characterized by evident and unpredictable variations in the electrical and optical properties, which are still unclear. This results in limitations in WS_2-based device performance. The unambiguous identification of the gas adsorption effects on WS_2 is required to minimize or control the gas exposure and develop systems competitive with the current technology. For that reason, in this thesis work, the variations of the electronic properties of WS_2 monolayers due to the gas adsorption are analyzed by means of *ab initio* Density Functional Theory (DFT) simulations. Considering that CVD samples are characterized by a high defect density, adsorption processes are simulated considering unintentional point defects as adsorption sites. The aim of this thesis is the identification of the effects of common molecules on the electronic properties of WS_2. Different defects are analyzed to identify which ones are able to markedly enhance the molecular adsorption process if compared to the interaction with the basal plane of the pristine material. Moreover, both physisorption and chemisorption processes are in-

vestigated to reveal which property alterations are reversible and which are permanent.

This thesis work is organized in five chapters. In chapter 1 an overview of TMD materials is presented, focusing on WS_2. Its properties, its principal synthesis techniques and common unintentional defects are reviewed. The main applications for WS_2 monolayers are also reported, evidencing the implications of the gas exposure. Chapter 2 resumes the theoretical aspects underlying the analysis of the electronic properties of WS_2: a general description of DFT, along with some practical aspects associated to its implementation are discussed. Chapter 3 is devoted to preliminary computational accuracy tests on the pristine WS_2, aiming at the identification of the optimal simulation conditions. Chapter 4 is devoted to the analysis of the structural and electronic properties of common unintentional point defects (i.e., V_S, O_S and Cr_W). Formation energies, band diagrams, Projected Density of States (PDOS), charge density isosurfaces are discussed for each type of defect in order to identify their signature and effects on the WS_2 monolayer. Chapter 5 analyses the adsorption of common gas molecules (O_2, H_2O and NH_3) on the previous analyzed types of defects. Most of the discussion is reserved to O_2 since its adsorption has the major effects in the band diagram. Specifically, the interaction on the V_S site is carefully analyzed since both physisorption and chemisorption processes are possible, and the material properties are significantly modified when the transition between these adsorption states occurs. Finally, conclusions and future perspectives are drawn in the last section.

CHAPTER 1

WS_2: a 2D material in optoelectronics

1.1 Overview on 2D Transition Metal Dichalcogenides

Low-dimensional materials (0D, 1D and 2D) have received considerable research interest in the last decades. Specifically, from the first experimental evidence of graphene [1], 2D materials (i.e., crystalline solids composed by a single layer of atoms) have become a hot research topic. The main interest arises from the peculiar quantum phenomena occurring at low-dimension scale and the completely different properties of monolayers with respect to their bulk counterparts. For example, 2D materials are very interesting in nanoelectronics in view of the scaling trend characterizing the technological development. Indeed, 2D material systems are the atomic level limit of any 3D systems; hence synthesis and stability of 2D materials can be foreseen as a solution of common top-down fabrication limits and issues in the behaviour of nanoscale devices. Graphene is the most famous 2D material and it is commonly appreciated for its excellent electrical and thermal properties [1]. Nevertheless, it has a relevant limit: graphene is a zero-gap system. This implies that the optical emission is not possible in this material, resulting in a huge limit in optoelectronic applications. For that reason, research activity has moved to the analysis of other 2D materials with a semiconducting nature. Transition Metal Dichalcogenides (TMDs) are among the most interesting 2D semiconductors. Their general chemical formula is MX_2, where M is a transition metal as molybdenum (Mo) or tungsten (W), while X is a chalcogen such as sulphur (S), selenium (Se) or tellurium (Te). Examples of TMDs are MoS_2, $MoSe_2$, $MoTe_2$, WS_2 and WSe_2. A monolayer (ML) of TMD is actually an atomic trilayer composed by two layers of chalcogens connected by a layer of transition metal atoms [2]. These materials exist also in the bulk phase: bulks are composed by a stack of monolayers reciprocally interacting through van der Waals forces, as shown in Figure 1.1. The weakness of interlayer interactions and the strong covalent bonds between M and X atoms within the same layer allow TMDs to be stable both in the bulk and the monolayer phase. The perfect surface of a TMD monolayer does not expose any dangling bonds, hence

no surface relaxation or reconstruction mechanisms occur. This peculiarity is the main difference between 2D materials and bi-dimensional systems realized by an atomic scale deposition of a 3D material. This is the origin of the superior electrical and optical properties of TMD monolayers with respect to nanometric thickness layers of common materials employed in optoelectronics.

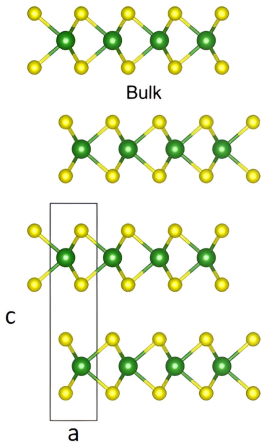

Figure 1.1: Structure of a TMD in bulk phase: green balls are transition metal atoms, yellow balls are the chalcogen ones [3]. The rectangular shape highlights the primitive cell.

.

Different polytype structures of TMD monolayers have been reported [2], as shown in Figure 1.2. The 1H polytype is a hexagonal phase, while the 1T is a tetragonal phase. The main structural difference is correlated to the chalcogen relative position: chalcogen atoms of the top and bottom planes are aligned in the 1H phase, while a 60° rotation in the monolayer plane separates the X atoms in the 1T phase. In some TMDs, such as MoS_2 and WS_2, the 1T phase is not thermodynamically stable, and it is structurally distorted, as shown in Figure 1.2. The 1H phase is the most relevant for optoelectronic applications since it is characterized by a semiconductor behaviour, while the 1T is metallic and its distorted phase has a very small gap [4].

The most studied TMD monolayer material is 1H-MoS_2. Electrical and optical properties of this material have been extensively studied from the theoretical and the experimental standpoint [5],[6]. Recently, research has progressively extended to other TMD materials, looking for superior properties with respect to MoS_2. For example, WS_2 has caught lots of attention. According to theoretical studies [7], WS_2 should have superior electrical properties with respect to MoS_2, due to lower effective masses and a higher mobility. Nevertheless, fabricated MoS_2-based devices are still better than WS_2 counterparts for both electrical and optical properties, when they are tested at ambient atmosphere [8]. This reveals that WS_2 is more sensitive to ambient conditions in comparison to MoS_2 and further studies are required in order to clarify the influence

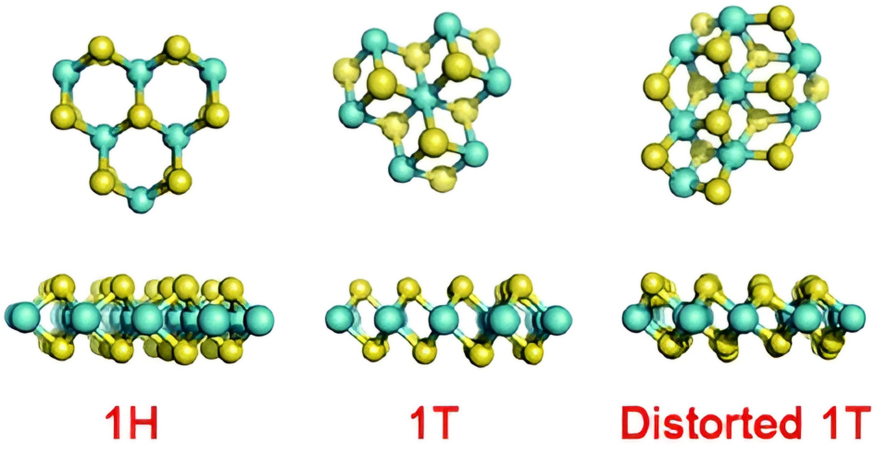

Figure 1.2: Polytype structures of a TMD monolayer: light blue balls are transition metal atoms, yellow balls are the chalcogen ones [2].

.

of the environment on the WS_2 properties. For that reason, this thesis focuses on WS_2 and the influence of molecule adsorption on this 2D material.

1.2 WS_2 monolayer

Tungsten disulfide (WS_2) is an inorganic compound that exists naturally as a rare mineral. It is usually observable in the bulk phase which is used as a dry lubricant. However, WS_2 is by far more appealing in the monolayer or few-layer structure, above all in the semiconductor polytype. As other TMDs, WS_2 is an indirect band-gap material in the bulk phase: experimentally the indirect gap is about 1.3 eV [9], a bit larger than the MoS_2 counterpart (1.23 eV [10]). Figure 1.3 shows the indirect transition between the valence band maximum at Γ and the conduction band minimum at T. These states are mainly originated from W d orbitals and S p_z orbitals [9]. The latter are susceptible to the presence of external layers, hence the minimum of the conduction band at T and the maximum of the valence band in Γ strongly depend on the number of the layers. This implies that the gap value changes progressively decreasing the thickness of the system. In the limit of monolayer, WS_2 1H polytype shows a direct gap at the K point, as reported in Figure 1.3. States at K are mainly due to W d orbitals, that are quite insensitive to layer number [9]. So, WS_2 progressively evolves from an indirect to a direct gap material reducing the number of the layers. The direct band gap of the monolayer is equal to 2.05 eV [9]. For comparison, MoS_2 shows a similar dependence on the layer number with a direct gap equal to 1.8 eV in the monolayer limit[11]. The size and the direct nature of ML 1H-WS_2 are the key elements for which this TMD is a suitable candidate for light emitting systems in the

visible range.

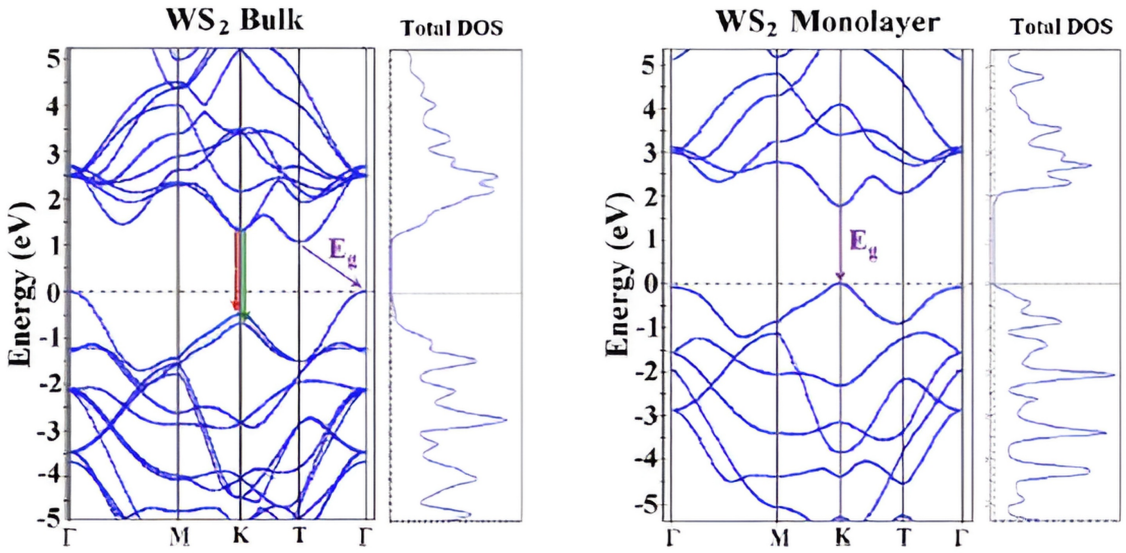

Figure 1.3: Band diagram and DOS of WS_2 in bulk (left) and 1H monolayer (right) phase [9].

Further electronic properties of WS_2 monolayer are also interesting. The effective electron mass (normalized to the electron mass at rest) is about 0.3, while the hole mass is about 0.41 [12]. For comparison, the corresponding effective masses of MoS_2 monolayer are 0.46 and 0.56 respectively. The electron mobility is also superior with respect to the MoS_2 (1100 and 340 cm^2 V^{-1} s^{-1} respectively [7]). The electronic properties of WS_2 can be also effectively tuned. Experimentally, the pristine material behaves as an n-type semiconductor [13], nevertheless it can turn into a p-type one incorporating foreign atoms [13],[14]. In conclusion, WS_2 monolayer is an ideal candidate for a wide range of applications in electronics as well as in optoelectronics, as more extensively discussed in section 1.2.5.

1.2.1 Synthesis techniques for WS_2 monolayers

The attractiveness of TMD monolayers is also associated to the availability of well-established methods for their synthesis: exfoliation, chemical vapor deposition, metal organic chemical vapor deposition, atomic layer deposition, molecular beam epitaxy etc [15]. Initially, WS_2 monolayers were mainly fabricated by exfoliation of the bulk phase, similarly to graphene. Commercial WS_2 bulk can be mechanically exfoliated (ME) in few-layer or monolayer structures. This technique involves the peeling of layers from the bulk crystal using an adhesive and then the transfer onto a substrate (e.g., SiO_2 on Si wafer [16]). Alternatively a liquid exfoliation (LE) approach is also possible, employing solvents to attenuate the inter-layer interactions [17]. Despite the limited

number of defects (e.g, S vacancies) and a more uniform spatial homogeneity and stoichiometry, exfoliation techniques are not effective for large scale production, due to issues associated for instance to the transfer and the solvent removal [18]. Moreover, the flake shape is very irregular, as shown in Figure 1.4a.

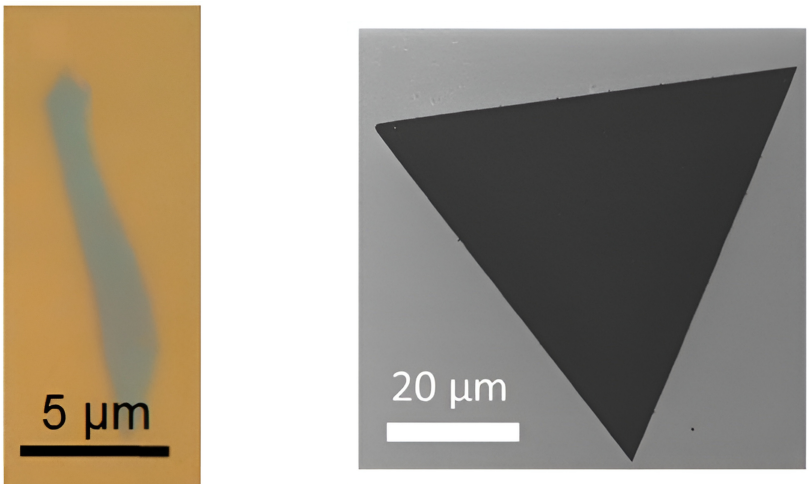

(a) ME sample [16]. (b) CVD sample [13].

Figure 1.4: Appearance of WS_2 monolayers realized with different approaches.

In view of the discussed issues of the exfoliation processes, Chemical Vapour Deposition (CVD) has become the most popular approach for WS_2 monolayer synthesis. Different recipes have been optimized to obtain regular and quite large flakes, as shown in Figure 1.4b. Commonly WO_3 powder is used as precursor for the transition metal, while gaseous HS_2 [15] or S powder [13] is the chalcogen source. Usually sapphire [14], graphene over SiC [15] or SiO_2 over Si [9] are employed as substrates for the growth. Depending on the growth conditions, triangular flakes can be obtained, as shown in Figure 1.4b. Hexagonal shapes are also reported [19]. In both cases, the lateral edges can be easily larger than tens of μm. The possibility of synthesis of large flakes is also proved by a recent result: the growth of a 2-inch wafer of continuous monolayer film with grain size up to millimeter scale has been reported [20]. The scalability of the CVD approach, together with the large and regular flakes obtained, makes this synthesis approach the most appealing for applications. Moreover, this technique is the most suitable for incorporation of dopant atoms in the flakes. The main drawback of CVD samples is a higher unintentional defect density that can significantly modify the monolayer properties [21]. For that reason, recently other synthesis approaches have been proposed: for example, monolayers have been successfully synthesised by evaporation of WS_2 powder [22] or through magnetron sputtering [23].

1.2.2 Unintentional defects in WS_2 monolayers

The presence of defects can alter the electrical and optical properties of any material. However, defects are particularly relevant in 2D materials. Due to the strong electronic quantum confinement and the reduced electrostatic screening, the properties of 2D materials are generally more susceptible to structural defects than their bulk counterparts [24]. For example, defects in 2D materials usually generate electronic states that are deeper in the bandgap and more tightly confined [25].
In this framework, defect engineering becomes an effective approach to tune WS_2 monolayer properties. Different foreign atoms, such as V, Nb, Re, Mn and Fe have been intentionally introduced as dopants in WS_2 flakes [14], [25]. They are W substituent atoms and can enhance the electron or hole concentration or introduce in-gap defect states able to mediate specific optical transitions. Substitution or addition of carbon-based functional groups at the S sites have been also proposed as doping strategies [4], [13].
These doping approaches deal with the creation of intentional defects, nevertheless unintentional defects are also relevant. Indeed, due to the enhanced influence of defects in 2D materials, unintentional defects, even at low concentration, can modify the material properties or alter the behaviour of the intentional doping. This problem is significant in CVD samples, as discussed in paragraph 1.2.1, due to the higher number of created defects with respect to exfoliated monolayers. For that reason, different works classify the unintentional defects introduced during the CVD synthesis [15],[19],[26]. Commonly, sulphur vacancies (V_S) are identified as the most abundant defect type. Oxygen as substituent of sulphur (O_S) is also common and it passivates chalcogen vacancies, whereas chromium impurities (Cr_W) are the most probable tungsten substituents. These defects (V_S, O_S and Cr_W) are the most important unintentional defects in CVD monolayers and they will be more extensively discussed in the following paragraphs. Occasionally, other types of defects in as-grown samples are identified: Fe [26], Mo [15] replacing W, W vacancies [19] and carbon group in the chalcogen site [27]. Nevertheless, they are by far less common, so they are not treated in this thesis work.

1.2.2.1 Sulphur vacancy and Oxygen substituent

Defects at the chalcogen sites are the most reported defects in TMDs [2]. These defects are commonly identified as sulphur vacancies in WS_2. However, only recently much more effort has been spent to investigate the possibility that foreign atoms occupy the vacancy due to its high reactivity [28]. Necessity of distinction between V_S and S substituent atoms arises from the contrasting properties that are commonly attributed to vacancies. Indeed, according to some authors [19], [24] V_S can enhance the optical emission intensity. Whereas other works [21], [29] consider vacancies detrimental. The ambiguity about the role of the vacancies is strictly associated to issues in the identification of V_S and S substituent atoms at the experimental level. For ex-

ample, Transmission Electron Microscopy (TEM) can be employed to identify defect sites, but light substituent atoms, such as oxygen, produce very weak TEM contrast and could be mistaken for vacancies [28]. Moreover, the electron beam can induce the formation of new S vacancies, hence the abundance of this type of defects in 'as-grown' samples, before characterization, becomes unclear [30]. At the same time, even if Atomic Force Microscopy (AFM) is sensitive to the outermost surface layer, oxygen substituent atoms are located slightly below the surface sulfur plane. Hence, it is easy to erroneously classify an oxygen substituent atom as a missing sulphur one [30].

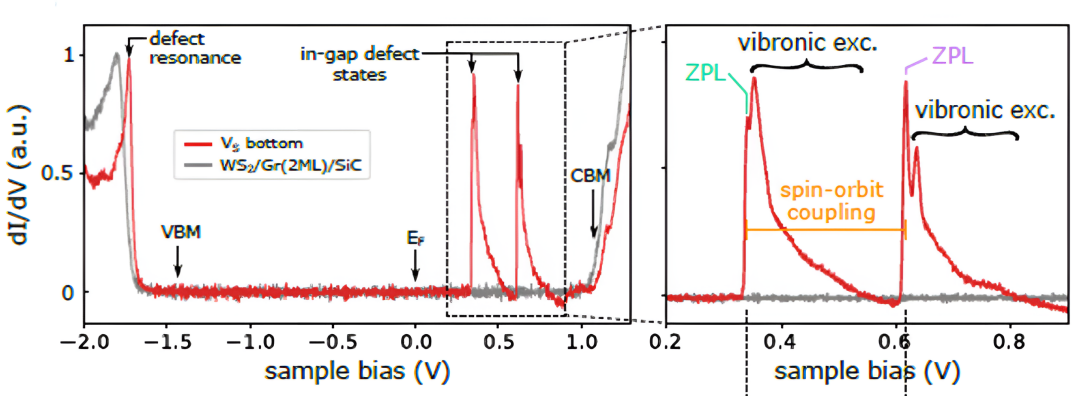

(a) Sulphur vacancy [30].

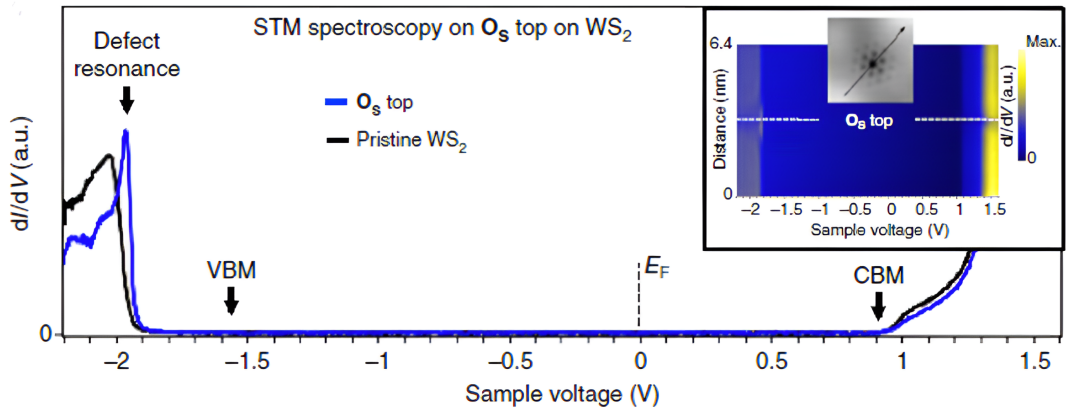

(b) Oxygen substituent [28].

Figure 1.5: STS spectra recorded on different point defects in WS_2 monolayers.

An effective way to distinguish V_S from O_S relies on the analysis of the electronic properties of the defects by Scanning Tunnelling Spectroscopy (STS). Indeed, the analysis of the Local Density of States (LDOS), evaluated by STS, allows to uniquely distinguish these types of defects. The experimental LDOS of the V_S, reported in Figure 1.5a, is characterized by two in-gap defect states below the conduction band. The broadening of the peaks is due to the inelastic scattering between electrons and phonons (vibronic excitations), while the large splitting of in-gap states (252 meV) is associated to Spin-Orbit-Coupling [30]. On the contrary, the STS spectrum in corre-

spondence of the O_S site, reported in Figure 1.5b, shows no in-gap states. A defect peak only appears in the correspondence of the valence band maximum when oxygen is incorporated. Hence the presence/absence of in-gap states can be employed to distinguish V_S and O_S.
This approach allows to get more information about the abundance of S vacancy in 'as-grown' samples. Even if S vacancies are considered very common, it has been proved that 'as-grown' monolayers have very low V_S concentration, while O_S defects are the most abundant [28]. Indeed, O atoms can easily occupy the S vacancies. O atoms can be incorporated during the monolayer synthesis (above all in CVD samples due to the O presence in WO_3 precursor) or in a subsequent step due to the flake oxidation under ambient conditions. S vacancies can be created after the synthesis by the action of electron microscopy beams or during high-temperature annealing (T $\approx$ 600 °C) [30]. Notice that the annealing steps are common during flake handling in order to remove contaminant from the surface between different steps. This justifies the presence of V_S even if they are absent immediately after the synthesis.

1.2.2.2 Chromium substituent

Chromium is a common substituent atom for tungsten. Even if Cr atoms can be intentionally introduced in WS_2 flakes [14], Cr impurities have been also reported in 'as-grown' samples [15],[26]. Cr can be unintentionally introduced during the CVD synthesis due to Cr impurities present in the W precursor (i.e., WO_3). Cr atoms usually appear as isolated defects, however configurations in which pairs of Cr impurities are sufficiently close to interact, have been also reported [15].

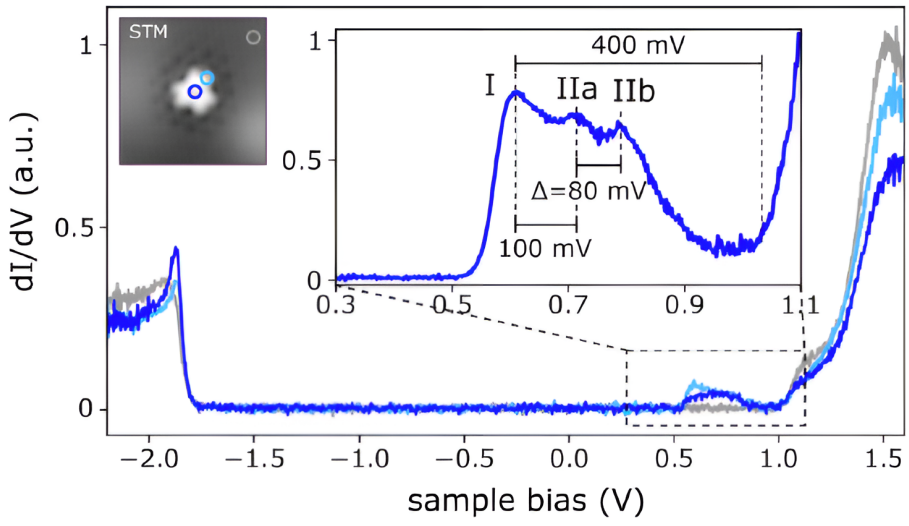

Figure 1.6: STS spectrum recorded on Cr substituting W in WS_2 monolayers [15].

The identification of Cr atoms substituting W is easier with respect to O_S. Indeed, the smaller Cr atomic radius with respect to W one results into an evident lattice

distortion and closer S atoms in correspondence of this defect. Moreover, the electronic signature of Cr_W is also peculiar: STS spectrum reported in Figure 1.6 shows that the LDOS in correspondence of Cr defect is characterized by three unoccupied in-gap states below the conduction band minimum (the lowest state is 400 meV below the conduction band minimum) [15]. Two defect states at higher energies (denoted IIa and IIb in Figure 1.6) appear very similar, suggesting that their degeneracy is removed by Spin-Orbit-Coupling. It is supposed that Cr in-gap defect states can act as effective radiative recombination centers and might host defect-bound excitons [15].

1.2.3 Photoluminescence spectrum of WS_2 monolayers

As discussed in paragraph 1.2, the direct band gap in the visible range of WS_2 monolayer is resposible for much of the appeal of this material. Several works experimentally analyse the optical emission spectrum of WS_2 by exciting the material with a laser source (Photoluminescence PL studies) [24],[31],[32]. The peculiarity of PL spectra of TMD monolayers is the presence of emission peaks associated to different exciton populations. The most relevant one, identified in all PL spectra, is associated to neutral excitons. An exciton is a bound state of an electron and a hole, reciprocally interacting due to the electrostatic Coulomb force. Since electrons in this state are interacting with holes, their ground state energy is slightly smaller than the 'quasi-free' electron energy in conduction band. This implies that the energy released by recombination when the electron and the hole are interacting in the exciton state is smaller than the energy released by the recombination of a electron in conduction band and a hole in valence band. The main consequence in the emission spectrum is the presence of a peak associated to the exciton recombination at energies slightly below the nominal electronic band gap. This energy is referred to as the 'optical gap' of the material. Excitons are only stable at cryogenic temperature in bulk materials, but they are commonly found at room temperature in case of low-dimensional systems. Specifically, Coulomb interaction in 2D materials is enhanced due to the spatial confinement and the reduced screening [31]. Hence, not only excitons, but also more complex systems of electrons and holes interacting due to the Coulomb force can be found in WS_2. Among different exciton populations, charged excitons (i.e., states composed by three interacting carriers), also called trions, can be identified. Due to the n-type nature of WS_2 monolayers, negative trions composed by two electrons and a hole are more probable [33]. Bound excitons (i.e., excitons localized close to a defect site) can be also identified in regions with higher defect densities, above all at low temperature [32]. Finally, biexcitons (i.e., systems composed by two interacting neutral excitons) are present in case of high carrier concentration (e.g., at high power laser irradiation) [34]. Recombination of carriers associated to different exciton populations is responsible for specific emission peaks visible in the PL spectra. An example of PL spectrum of WS_2 monolayer, collected at cryogenic temperatures, is reported in Figure 1.7. The

spectrum is deconvoluted in three peeks: the neutral exciton A^0 at about 2.02 eV, the negative trion A^- at about 1.92 eV and the defect-bound exciton D at 1.75 eV [33]. No biexciton peak is identified in this case.

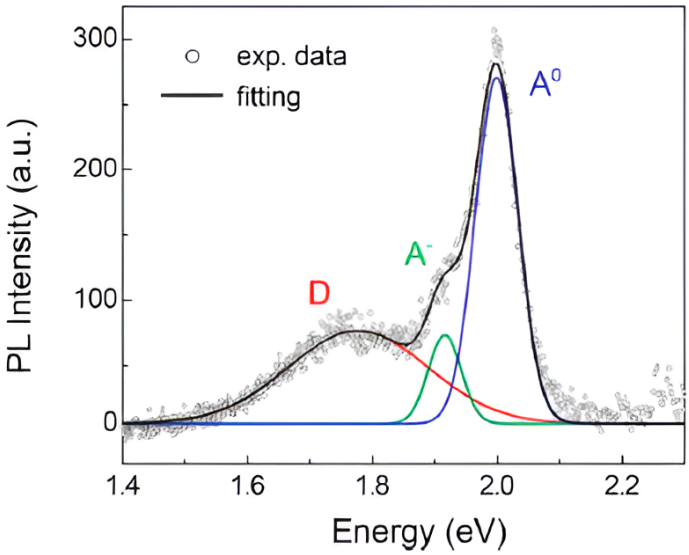

Figure 1.7: PL spectrum of the inner part of WS_2 monolayer at 77 K [33].

Nevertheless, the interpretation of the emission peaks is by far not trivial due to the several characterization conditions that can modify the intensity and the position of peaks. For example, temperature significantly influences the stability of the different exciton populations [34]. Moreover, the peak positions red-shift due to the electronic band gap decrease at increasing temperature and peaks become more broadened and overlapped at rising temperature, so their identification is more complex. In addition, non-uniform spatial distribution of defects and carrier concentration can cause a PL spectrum variation within the same flakes [22],[26],[33]. Finally, the relative intensity of peaks varies according to the excitation laser power and the laser exposure time, with an enhancement of biexciton contribution at high laser power [34].

1.2.4 Influence of molecule adsorption on PL spectrum

Among all the issues associated to PL spectrum variations, the optical property variability due to the surrounding environment conditions is the most problematic in view of applications. Several works experimentally notice that PL peaks are strongly influenced by the nature of the adsorbed molecules [16], [35]. The origin of the intensity variation and peak shift has not been completely identified, mainly because of the wide variability of the experimental evidences. Optical property variation is often attributed to the chemical doping action of adsorbed molecules [16], [35]. Molecules act as n- or p-doping for WS_2 monolayers. Effectiveness of the carrier concentration modulation due to molecule adsorption has been verified experimentally, analysing the electrical

properties [16]. For example, NO_2 is supposed to behave as an acceptor molecule [36]. Experimentally, flakes exposed to NO_2 are characterized by a blue-shift of the PL emission, as reported in Figure 1.8. The decrease of the electron population with respect to the hole one due to the p-doping action, can enhance the presence of neutral excitons with respect to negative trions. Hence, the blue-shift is attributed to the intensity increase of the neutral exciton peak, located at higher energies with respect to the trion one [35]. On the other hand, NH_3 is supposed to be a donor molecule for WS_2 [36], hence its adsorption is responsible for an electron concentration increase and an enhancement of negative trion role. The boost of the trion peak, at lower energies, could be the cause of the PL red-shift experimentally observed in case of NH_3 treated samples, as shown in Figure 1.8.

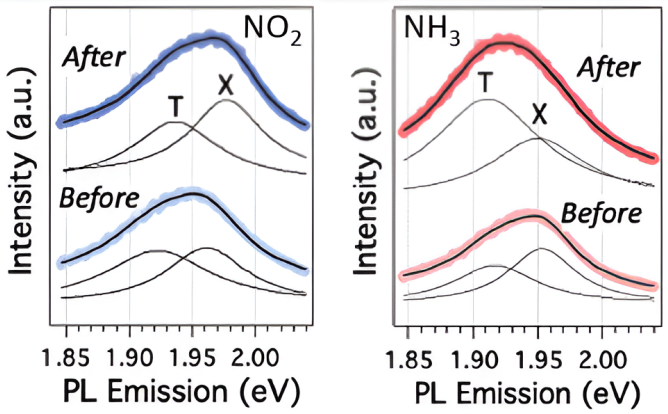

Figure 1.8: PL emission spectra collected before and after different gas exposure (NO_2 on the left, NH_3 on the right) [35].

However, the interpretation of the PL spectra due to molecule adsorption can be more complex. Indeed, the analysed samples can already host contaminant molecules (e.g., organic compounds, such as polyciclic aromatic hydrocarbons) before the gas exposure [37], [38]. These impurities can be removed during the PL measurement due to the energy provided by the excitation laser. Hence, new adsorption sites become available during the laser exposure and the controlled environment molecules can be easily adsorbed on them [39]. This implies that the evolution of PL spectra during laser exposure has to be interpreted considering the nature of preexisting adsorbed contaminants as well as the role of gas molecules present in the environment during the PL measurement [37]. For example, the enhancement of PL due to O_2 adsorption during laser irradiation could be explained as an oxygen passivisation mechanism of S vacancies previously occupied by organic contaminants [39]. In conclusion, the shift and enhancement of the different PL peaks requires additional studies in order to identify the role of a wider range of adsorbed molecules and decouple the effects of the different chemical species adsorbed at the same time.

1.2.5 Applications for WS_2 monolayers

The extraordinary properties of 2D materials can be effectively tuned in view of a wide range of applications. Specifically, the electrical and the optical properties make WS_2 an optimal material for electronic and optoelectronic applications. These applications will be more extensively discussed in the next paragraphs. Nevertheless, WS_2 monolayers are also effectively employed in other fields. For example, the large Spin-Orbit-Coupling of WS_2 monolayer is appealing for spintronic devices [40]. Moreover, the reactivity of flake edges or monolayers decorated with nanoparticles is interesting for catalysis [41],[42].

1.2.5.1 Field Effect Transistors and FET-based gas sensors

Despite the superior electrical properties of graphene, its semi-metallic nature is incompatible with the requirements of transistor devices. Indeed, a material with a gap (i.e., a semiconductor) is required in order to have an effective switch-on/switch-off of the device. For that reason, 2D semiconductors as WS_2 are appealing for the realization of Field Effect Transistors (FETs) at the nanoscale. A schematic layout of a WS_2-based FET is reported in Figure 1.9a, together to a false-colored SEM image representing a real implementation 1.9b. SiO_2 over heavily doped Si substrate is often used as gate-dielectric and back-gate contact respectively, as shown in Figure 1.9, but a gate-dielectric and a metal contact can be also deposited above the monolayer to realized a top-gate configuration [43].

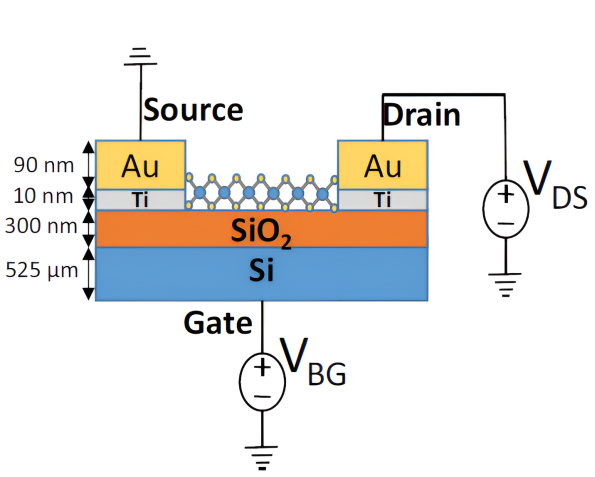

(a) Schematic layout [8].

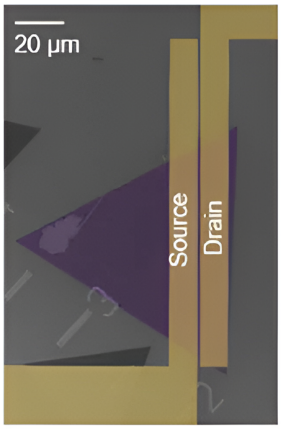

(b) False-colored SEM image [13].

Figure 1.9: WS_2 monolayer-based Field Effect Transistor.

The appeal of ML WS_2-based FET is associated to the possibility of an easy fabrication of a system stable at the nanoscale, avoiding the issues associated to the common top-down approaches employed in the realization of nanodevices. Hence, 2D semicon-

ductors can become the best platform for ultimate scaled-down FET [44]. Indeed, it is expected that monolayer-based FETs are less prone to Short Channel Effects [44]. Moreover, the leakage currents due to tunneling through the gate oxide are smaller than in the standard material devices. For that reason WS_2 FETs are appealing for low-power consumption nanodevices, above all for memory applications [44]. The atomic thickness of WS_2 monolayers is also appealing for flexible electronics. However, it has been observed that WS_2-based FETs have poorer performance when they are not in a controlled environment and they work in ambient atmosphere [8]. Hence, molecule adsorption on WS_2 not only alters the optical properties, as discussed in paragraph 1.2.4, but also has negative effects on the electronic performances.

Nevertheless, the influence of molecule adsorption on WS_2 FET electrical characteristic can be effectively employed for gas sensing. As discussed in paragraph 1.2.4, molecules adsorbed on the monolayer can act as chemical n- or p-dopants, altering the carrier concentration. As schematically represented in Figure 1.10, adsorbed molecules can act as a secondary virtual gate, decreasing or increasing the electron concentration in the FET channel, modifying the device conductivity. The use of a 2D material guarantees a large surface-to-volume ratio resulting in a high sensitivity, even at low target concentrations [45]. Specifically, WS_2 is more sensitive to gases with respect to other TMDs; for that reason WS_2-based sensors are effective for a large set of molecules such as O_2 [46], ethanol [46], NH_3 [46], H_2S [47], water [48], NO_2 [49].

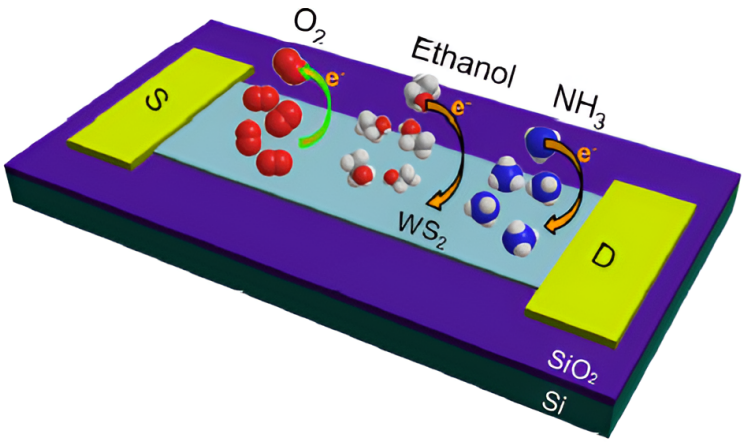

Figure 1.10: Representation of WS_2-based FET gas sensor [46].

1.2.5.2 Optoelectronic devices

The direct band gap nature makes WS_2 monolayer an effective absorbing material for photo-detectors, solar cells as well as an optically active material in LEDs, lasers and single photon emitters. WS_2 is commonly coupled to graphene in hetero-structures in order to realize a full optoelectronic system. WS_2 is employed in the optical part of the system, while contacts/connections are realized in graphene. For example, several

photo-detectors composed of WS_2/graphene hetero-structures have been proposed [50], [51]. The absorption coefficient of WS_2 ($> 10^5$ cm^{-1}) in the visible range is quite large and higher than common Si bulk, making WS_2 an optimal absorbing material [52]. At the same time, the high mobility of graphene employed in photo-detector connections allows for high working frequencies [51]. Moreover, WS_2 can be deposited also at low temperatures on polymeric substrates, so that flexible photo-detectors can be realized [53]. The same advantages of WS_2/graphene hetero-structures are also employed in solar cell applications. Due to the high absorption coefficient, together with the reduced volume of the absorbing material, WS_2 solar cells have an extraordinary power density for unit of volume, larger than other ultra-thin film solar cells [52].

Despite the remarkable absorption properties of WS_2 monolayers, this direct band gap material is by far more interesting for emitting sources. Different LED structures with WS_2 monolayers have been proposed, based both on homo-junctions [54] and hetero-junctions [55]. For example, a LED with a controllable circular polarization emission has been realized using a p-i-n hetero-junction composed by a heavily p-doped silicon - intrinsic WS_2 - n-doped indium tin oxide (ITO), as shown in Figure 1.11a [55]. This device is characterized by a strong red luminescence, even if the active material is only composed by a monolayer. Hence, this example shows the possibility of ultra-thin LED that can be employed in flexible displays and wearable electronics [55].

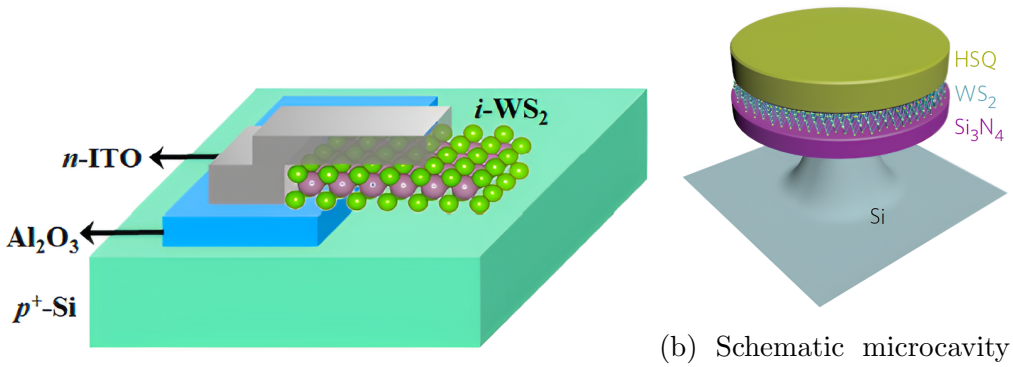

(a) Schematic LED structure [55].

(b) Schematic microcavity laser structure [56].

Figure 1.11: Examples of optically active devices based on WS_2 monolayer.

Stimulated emission can be also achieved in WS_2. Indeed, fabrications of lasers with WS_2 monolayers have been reported. For example, WS_2 can be used as the active material in a whispering gallery microcavity laser [56]. As shown in Figure 1.11b, WS_2 monolayer is sandwiched between two dielectric materials. These lateral layers not only constitute the resonant cavity, but also protect WS_2 from the air exposure and subsequent degradation of the optical properties. Advantages of this laser cavity are the high quality factor and optical confinement that allow for the lasing condition even

if the active material volume is very small. Specifically, WS_2 results the monolayer with the highest quantum yield among other TMDs [56]; for that reason WS_2 is the most suitable TMD for laser application. The described laser is characterized by a small footprint, a low power consumption and is effective for on-chip optoelectronics.

Despite the relevance of previous discussed devices, one of the most interesting optoelectronic application for WS_2 is as Single Photon Emitter (SPE). SPE is an optical source able to emit on-demand and separately a single photon. Each emitted photon is identical, in a single and well defined mode. The possibility of controlled photon emission in a well defined state is relevant in many applications, such as quantum computing and simulation [57], quantum information [58], sensing [59], Single Photon Emission Computed Tomography [60] and quantum communication [61]. A material for SPE should have discrete and well isolated states within the band gap in order to mediate optical transitions at a well defined photon energy. Hence, proper defects are introduced in the material in order to get isolated defects states. Single photon sources can be realized in 3D bulk materials, for example by creating nitrogen-vacancy color centers in diamond [62]. Nevertheless, achieving deep and isolated in-gap defect states is more complex in bulk materials; moreover issues associated to the spatial control of the color centre position and the dimension of the bulk system result in a more complex integration on a chip [63]. For that reason, 2D materials are appealing as single photon sources, due to their scalability and a superior control of defect position [64]. Moreover, the quantum confinement and the reduced electrostatic screening in two-dimensional systems are responsible for deeper and more tightly confined in-gap defect states, improving the spectral purity of the emission [25]. For example single photon emission has been achieved at V_S and Cr_W sites in WS_2 [64]. Single photon emission in WS_2 is possible not only in unintentional defects, but also in intentionally doped samples, for example with Nb atoms replacing W ones [65]. Notice that molecule adsorption on WS_2 monolayers in the discussed optoelectronic devices can be detrimental, since it causes a variability in the material properties, but it is particularly dramatic in SPE, since adsorption at a defect site can alter the in-gap defect states and deteriorate the emission purity. For that reason, capping layers composed by other 2D materials, such as hexagonal boron nitride, can be employed to protect WS_2 monolayers from molecule exposure [63].

In summary, sections 1.2.3 and 1.2.4 show the complexity of the interpretation of the WS_2 properties, above all when the samples are exposed intentionally or unintentionally to different gases. Section 1.2.5 highlights some implications associated to the flake - gas interaction at the application level. It is evident that WS_2-based devices are not competitive with the current technology yet. A cause of the poor performances is associated to the evident and apparently unpredictable variations in the material properties when flakes are exposed to ambient atmosphere. Hence, the decoupling of

the adsorption effects from the intrinsic properties is a fundamental step to improve the device layout and the fabrication steps. However, it is difficult to uniquely distinguish the role of the different molecules in the environment, at the experimental level. Moreover, it is not possible to prevent the simultaneous adsorption on areas of the samples without defects and in defective regions. Hence, the uniquely identification of the specific role of the defects in the adsorption is complex.
For that reason, this thesis employs *ab initio* simulations to separately characterize the adsorption of different molecules and study the interaction on specific sites (i.e., point defects). Specifically, considering the high density of defects in CVD samples, this work aims at the identification of the unintentional point defects that strongly enhance the gas-flake interaction with respect to the pristine material. Different molecules are analysed to identify which are characterized by a high affinity for the defect sites. The alterations of the material properties are investigated to understand which are reversible, since associated to physisorption processes, and which are permanent. Finally, the variations are also analysed to understand if molecule adsorption has some beneficial effects.

CHAPTER 2

Methods

The study of the electronic structure is a central issue in Physics since the basis for understanding materials and phenomena ultimately is correlated to the analysis of the electronic structure. In this framework, *ab initio* atomistic approaches have become a powerful tool to elucidate experimentally observable phenomena. Among the plethora of different methods to solve the Schrödinger equation in case of many-body systems (i.e., electrons and ions reciprocally interacting), Density Functional Theory (DFT) is one of the most commonly employed. For that reason, this thesis work is completely developed in the framework of this theory. This chapter resumes the basic principles of DFT, together with some technical elements of its implementation required to perform a DFT computation.

2.1 The many-body problem and the adiabatic approximation

Matter is characterized by the co-presence and reciprocal interaction among a large number of electrons and nuclei (or equivalently among outer shell electrons and ions composed by inner shell electrons and nuclei). In the quantum mechanics description, this system is described by the following Hamiltonian 2.1(in atomic units):

$$\begin{aligned}\mathcal{H} = &-\frac{1}{2}\sum_i {\nabla_i}^2 - \sum_I \frac{1}{2M_I}{\nabla_I}^2 + \frac{1}{2}\sum_{i\neq j}\frac{1}{|\mathbf{r}_i - \mathbf{r}_j|} \\ &- \sum_{i,I}\frac{Z_I}{|\mathbf{r}_i - \mathbf{R}_I|} + \frac{1}{2}\sum_{I\neq J}\frac{Z_I Z_J}{|\mathbf{R}_I - \mathbf{R}_J|},\end{aligned} \tag{2.1}$$

where:

- M_I is the mass of the I-th ion,

- Z_I is the atomic number of the I-th ion,
- $\mathbf{R}_I$ is the position of I-th ion,
- $\mathbf{r}_i$ is the position of the i-th electron.

The first term in 2.1 is the sum of the kinetic energy contributions of each electron, while the second one is the analogous counterpart of the ionic system. The third contribution describes the interaction between electron pairs, the fourth considers the attraction between electron and ion pairs, while the last is associated to repulsion of the ion couples. The complexity of equation 2.1 is its many-body character since the electron and ion systems are coupled together and the particle coordinates depend reciprocally on one another, continuously varying due to particle motion. Hence, neither analytical nor numerical approaches are able to effectively solve the problem described by the Hamiltonian in equation 2.1, especially in real systems where the electron and ion number is very large. A series of approximations is required to deal with this many-body problem. The main approximation is the adiabatic or Born-Oppenheimer approximation [66]. This assumption relies on the large difference between the velocity of the electronic system ($\sim 10^5 \div 10^6$ m/s) and the ion one ($< 10^3$ m/s). Hence, from the electron standpoint, ions are essentially stationary (i.e., electrons instantaneously respond to any ion motion). Whereas ions are not able to follow the instantaneous movements of electrons, but they only see a time average potential (V_i) associated to the electronic system. According to this assumption, Hamiltonian in 2.1 can be rewritten as:

$$\mathcal{H} = \mathcal{H}_{ions}(\{\mathbf{R}_I\}) + \mathcal{H}_e(\{\mathbf{r}_i\}, \{\mathbf{R}_{I0}\}) + \mathcal{H}_{e-ion}(\{\mathbf{r}_i\}, \{\delta\mathbf{R}_I\}). \tag{2.2}$$

The first term in 2.2 is the Hamiltonian associated only to the ionic system and it explicitly depends only on the ion coordinates:

$$\mathcal{H}_{ions}(\{\mathbf{R}_I\}) = -\sum_I \frac{1}{2M_I}{\nabla_I}^2 + V_i(\{\mathbf{R}_I\}). \tag{2.3}$$

The second term in 2.2 is the electronic Hamiltonian:

$$\mathcal{H}_e(\{\mathbf{r}_i\}, \{\mathbf{R}_{I0}\}) = -\frac{1}{2}\sum_i {\nabla_i}^2 + \frac{1}{2}\sum_{i\neq j}\frac{1}{|\mathbf{r}_j - \mathbf{r}_i|} - \sum_{i,I}\frac{Z_I}{|\mathbf{r}_i - \mathbf{R}_{I0}|}. \tag{2.4}$$

Notice that the electron-ion interaction in 2.4 considers only the condition in which ions are at their equilibrium position $\mathbf{R}_{I0}$, hence the ion coordinates become a parameter in the electronic Hamiltonian. The variations of the ion positions $\delta\mathbf{R}_I$ and the associated variations in the electron-ion interaction are encoded in the third term in 2.2, which is commonly described as interaction between electrons and phonons.

The main advantage of the adiabatic approximation is the partition of the original problem in sub-parts that can be studied separately and through different approaches

("classically", "quantum mechanically", "perturbation methods" etc...). In view of the electronic structure study, the electronic Hamiltonian 2.4 becomes the central point of the following discussion. Despite of the huge problem simplification due to the adiabatic approximation, the eigenproblem associated to 2.4 is still a many-body problem in which the electron number is very high. Different approaches have been proposed to solve it, the DFT solution is described in the next section.

2.2 Density functional theory

Density Functional Theory (DFT) is a method developed to describe correlated many-body systems. The original formulation is associated to the works of Hohenberg and Kohn in 1964 [67] and Kohn and Sham in 1965 [68]. From these milestones, lots of theoretical works have been published in order to improve the completeness and accuracy of this method. The peculiarity of the DFT approach is the central role of the electron density. Indeed, if other methods identify the electronic wavefunction as the basic unknown, in which the physical information is encoded, DFT replaces it with the electron density. In other words, all system properties are formulated as functionals of the ground state density. So, instead of considering a wavefunction $\psi(\mathbf{r}_1...\mathbf{r}_N)$ that is function of the coordinate position $\mathbf{r}_i$ for each electron, for a total number of $3N$ variables (neglecting spin contribution), the DFT description is associated to the electron density $n(\mathbf{r})$ that is a scalar function of 3 spatial coordinates $\mathbf{r}$. Origin of this alternative approach can be already identified in the Thomas-Fermi theory (1927) [69],[70], following improved by Dirac [71]. However, Hohenberg-Kohn theorems (2.2.1) and Kohn-Sham *ansatz* (2.2.2) are the core of the modern DFT approach.

2.2.1 Hohenberg-Kohn theorems

The Hohenberg-Kohn (H-K) theorems hold for a generic system of N interacting electrons in presence of a time-independent local external potential $V_{ext}(\mathbf{r})$. According to the first H-K theorem, for **any** system of interacting particles in an external potential, $V_{ext}(\mathbf{r})$ is determined uniquely, except for a constant, by the ground state particle density $n_0(\mathbf{r})$. This theorem has relevant consequences; indeed, once the ground state electron density $n_0(\mathbf{r})$ is known, a unique $V_{ext}(\mathbf{r})$ is determined up to an additive constant. Hence, the system Hamiltonian is uniquely assembled given $n_0(\mathbf{r})$ and if associated eigenproblem is solved, all wavefunctions and energy eigenvalues (both ground and excited states) can be evaluated. Therefore, all system properties are completely determined given only the ground state density. As shown in Figure 2.1, this approach is different from the standard solution of the Schrödinger equation, where, given $V_{ext}(\mathbf{r})$, through the Hamiltonian eigenproblem all wavefunctions Ψ_i are determined and, from the specific ground eigenstate Ψ_0, the associated electron density n_0 is evaluated.
According to the H-K scheme, the ground state expectation value of any observable is

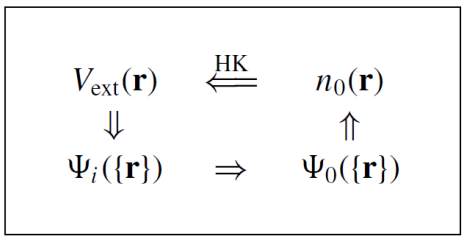

Figure 2.1: Schematic representation of Hohenberg–Kohn theorem. Smaller arrows denote the usual solution of the Schrödinger eq., while long arrow labeled "HK" denotes the Hohenberg–Kohn approach [72].

.

a unique functional of n_0. For example, the total energy $E[n]$ is expressed as:

$$E[n] = \int n\,(\mathbf{r})\, V_{ext}\,(\mathbf{r})\;\; d\mathbf{r} + F_{HK}[n]. \tag{2.5}$$

F_{HK} is defined as universal since it is independent from the specific $V_{ext}(\mathbf{r})$, because F_{HK} includes only energy terms (electron kinetic energy and electron repulsion energy) that strictly depend on the electronic system alone.

The second H-K theorem states that the minimization of the total energy functional $E[n]$ with respect to n allows for the identification of the ground state. The ground state energy E_0 is the minimum of $E[n]$ and the ground state density n_0 is the density associated to the minimum of $E[n]$. In other words, given a generic electron density $\tilde{n}$, relation 2.6 is always valid:

$$E_0 = E[n_0] \leq E[\tilde{n}]. \tag{2.6}$$

The minimization of the total energy in 2.5 with respect to $n(\mathbf{r})$, imposing the constraint of the constant number N of electrons (i.e., $\int n\,(\mathbf{r})\, d\mathbf{r} = N$), can be performed through the Lagrange multiplier approach as:

$$\delta \left\{ E[n] - \mu \left[\int n\,(\mathbf{r})\, d\mathbf{r} - N \right] \right\} = 0, \tag{2.7}$$

leading to the Euler equation:

$$\mu = \frac{\delta E[n]}{\delta n} = V_{ext}\,(\mathbf{r}) + \frac{\delta F_{HK}[n]}{\delta n}, \tag{2.8}$$

where the Lagrange multiplier μ is the chemical potential.

Notice the second H-K theorem shows a way to determine the exact ground state energy and density through the minimization of functional $E[n]$. However, even if n_0 encodes also information about excited states, in general this theorem does not provide any indication about excited state evaluation.

2.2.2 The Kohn-Sham *ansatz*

The H-K theorems 2.2.1 can be considered as an effective reformulation of the original many-body problem through functionals of the electron density. However, they do not solve the complexity of the many-body system since they do no specify any way to identify the functional required in equation 2.5. For that reason, the effectiveness of the H-K approach is associated to the Kohn-Sham (K-S) *ansatz* [68]. The basic idea of the K-S scheme is the association between the original and complex many-body system and a non-interacting system. The Hamiltonian of this auxiliary problem must be formulated so that the exact ground state density can be represented by the ground state density of the associated system of non-interacting particles. Notice this correlation is valid only for ground state properties and in general excited states cannot be directly shifted from a system to the other. Once the association between the original and the auxiliary problem is established, the application of the H-K approach is by far more convenient in the non-interacting electron system. In view of this task, it is convenient to introduce a new functional $G[n(\mathbf{r})]$, by subtracting the term of the electron density-density repulsion from the previously defined $F[n(\mathbf{r})]$, as:

$$G[n(\mathbf{r})] = F[n(\mathbf{r})] - \frac{1}{2}\int d\mathbf{r}\int d\mathbf{r}'\frac{n(\mathbf{r})\,n(\mathbf{r}')}{|\mathbf{r}-\mathbf{r}'|}. \tag{2.9}$$

Moreover, it is possible to emphasize the role of the kinetic energy functional T_s of the non-interacting system in 2.9, separating it from other terms grouped in $E_{xc}[n]$ (exchange-correlation contribution) as:

$$G[n(\mathbf{r})] = T_s[n(\mathbf{r})] + E_{xc}[n(\mathbf{r})]. \tag{2.10}$$

At this point the total energy functional $E[n(\mathbf{r})]$ in 2.5 can be rewritten as:

$$E[n(\mathbf{r})] = \int n(\mathbf{r})\,V_{ext}(\mathbf{r})\,d\mathbf{r} + T_s[n(\mathbf{r})] + \frac{1}{2}\int d\mathbf{r}\int d\mathbf{r}'\frac{n(\mathbf{r})\,n(\mathbf{r}')}{|\mathbf{r}-\mathbf{r}'|} + E_{xc}[n(\mathbf{r})]. \tag{2.11}$$

Similarly to 2.7 and 2.8, the minimization of $E[n(\mathbf{r})]$ with respect to $n(\mathbf{r})$. at constant electron number. results into a new Euler equation:

$$\mu = V_{KS}(\mathbf{r}') + \frac{\delta T_s[n]}{\delta n}, \tag{2.12}$$

where the Kohn-Sham potential $V_{KS}(\mathbf{r}')$ is defined in 2.13 and includes the Coulomb potential (Hartree term), the external potential and the exchange-correlation potential:

$$V_{KS}(\mathbf{r}') = \int d\mathbf{r}'\frac{n(\mathbf{r}')}{|\mathbf{r}-\mathbf{r}'|} + V_{ext}(\mathbf{r}') + \frac{\delta E_{xc}[n]}{\delta n} = V_{Hartree}(\mathbf{r}') + V_{ext}(\mathbf{r}') + V_{xc}(\mathbf{r}'). \tag{2.13}$$

.

If the total energy functional minimization process is not performed with respect to $n(\mathbf{r})$, but considering the electron wavefunctions ψ_i, with the constraint on the ψ_i orthonormality, one obtains the Kohn-Sham Schrödinger-like equations:

$$h_{KS}\psi_i = \left[-\frac{1}{2}\nabla^2 + V_{KS}\left(\mathbf{r}\right)\right]\psi_i = \epsilon_i\psi_i. \tag{2.14}$$

Once the wavefunctions ψ_i are evaluated by 2.14, the electron density is finally computed as:

$$n(\mathbf{r}) = \sum_i^N |\psi_i(\mathbf{r})|^2. \tag{2.15}$$

Notice that equation 2.14 appears as the eigenvalue equation of a non-interacting electron system. This means that interacting electrons can be described as independent electrons in presence of an effective potential V_{KS}. This is the key point of K-S approach.
Equation 2.14 is a non trivial eigenvalue problem since V_{KS} actually depends on $n(\mathbf{r})$(2.13), but $n(\mathbf{r})$ is evaluated only when all ψ_i are known (2.15). So, equations 2.14 and 2.15 are solved together and in an iterative way until convergence is achieved. This is numerically feasible since the Hamiltonian is associated to an independent particle problem.

Formally, once 2.14 is solved, the problem of the interacting electrons is sorted out, since the ground state density of the auxiliary system can be directly associated to the original one and then all other observables can be derived from $n_0(\mathbf{r})$. Practically, the many-body complexity is simply hidden inside an effective expression of V_{KS} and more specifically of $E_{xc}[n]$. Indeed, the exact correspondence between the original and auxiliary problem holds only if the correct expression for the exchange-correlation term is employed. Unfortunately, excluding the simple case of the uniform electron gas, exact forms for $E_{xc}[n]$ are unknown. So, even if DFT is an exact theory, the result accuracy strongly depends on the employed exchange-correlation functional. For that reason, a complex hierarchy of functionals has been developed in the last decades, starting from the simplest one (Local Density Approximation LDA) to a wide variety of Generalized Gradient Approximations (GGAs), orbital dependent functionals, hybrid functionals etc. In general, higher level functionals result into better results but at a higher computational cost, so a trade-off between accuracy and simulation time is always considered in DFT simulations.

2.2.3 LDA and GGA functionals

As discussed in section 2.2.2, the association between the many-body system and the auxiliary independent-particle one is guaranteed only if the exact form of the exchange-correlation functional is known. Since H-K and K-S equations do not provide any expression for $E_{xc}[n]$, only approximated functionals can be employed. The most simple

functional form is provided by the Local Density Approximation (LDA) or its generalization in case of unpolarized spin systems (Local Spin Density Approximation or LSDA) [73],[74]. It was originally developed for a homogeneous electron gas where $n(\mathbf{r})$ is constant everywhere and the exchange-correlation energy per particle $\epsilon_{xc}(n)$ is simply a function (not a functional) of the density. The total exchange-correlation functional results in the sum of contributions of N equivalent electrons:

$$E_{xc}^{hom}[n] = N\epsilon_{xc}(n). \tag{2.16}$$

This idea can be extended to a non-homogeneous electron gas system, in which the density is not constant, but depends on position. So, the exchange-correlation energy per particle $\epsilon_{xc}(n)$ expression, previously used for the homogeneous case, now depends on the local density. E_{xc} becomes a spatial average of $\epsilon_{xc}^{hom}(n(\mathbf{r}))$ weighted by the local density:

$$E_{xc}^{LDA} = \int n(\mathbf{r})\epsilon_{xc}^{hom}\left(n(\mathbf{r})\right) d\mathbf{r}. \tag{2.17}$$

The basic idea justifying the LDA approach is the quite short range of the effects of exchange and correlation. Actually, this statement is not completely true since the Hatree term in 2.13 contains a spurious self-interaction component (i.e., the interaction of the electron with itself) that is not local. The exchange term should compensate this nonphysical effect, but if E_{xc}^{LDA} is local by construction, this cancellation is incomplete. Hence the accuracy of LDA depends on the characteristics of the analysed system: LDA is effective in systems resembling homogeneous electron gases (e.g, nearly-free electron metals), but it works poorly in case of inhomogeneous electron distribution. For that reason, the LDA idea is generalized in more complex expressions for E_{xc} as in the Generalized Gradient Approximation (GGA) [75]. The non-locality is introduced in 2.17 considering that ϵ_{xc} depends not only on the local value of $n(\mathbf{r})$, but also on its gradient:

$$E_{xc}^{GGA} = \int n(\mathbf{r})\epsilon_{xc}\left(n(\mathbf{r}), \nabla n(\mathbf{r})\right) d\mathbf{r}. \tag{2.18}$$

Different strategies have been proposed to formulate $\epsilon_{xc}\left(n(\mathbf{r}), \nabla n(\mathbf{r})\right)$, often modifying the original expression ϵ_{xc}^{hom} of the homogeneous electron gas. The simplest and most used expression for E_{xc}^{GGA} is the PBE (Pendew, Burke and Ernzerhof) form [76]. Notice, even if GGA-PBE functionals can generally work better than LDA, they are not a complete expression for the true E_{xc}, hence more complex approximations are possible, but at a higher computational cost. The main limits of LDA/GGA are associated to a general imperfect description of the electronic properties, while the system total energy and the structural properties are adequately predicted. The most evident failure of LDA/GGA is associated to a band gap underestimation, mainly due to the not-justified association between the K-S eigenvalues of the independent electron system and the excited states of the original many-body system (the association is formally valid only for the ground states as discussed in 2.2.2).

2.3 Spin Density Functional Theory and Spin-Orbit Coupling

The previous sections describe the principles of DFT considering that the ground state density $n_0(\mathbf{r})$ only depends on the spatial coordinate $\mathbf{r}$. However, this formulation can be generalized introducing the role of the electron spin (Spin Density Functional Theory). In this framework, functionals are formulated considering that densities now depend on both space coordinate $\mathbf{r}$ and spin σ. Spin can be treated in different ways, but the simplest one is the collinear approach. In this case, the axis of quantization of the spin is assumed to be the same in all points. Hence, electrons can be simply described considering a spin-up and a spin-down population density. However, this approach can be generalized to the non-collinear case, where it is assumed that the spin axis orientation can vary point by point in the system. Hence, in each position, spin can be aligned to a generic direction, assuming a spin-up or spin-down configuration with respect to this direction.

The introduction of the non-collinear spin description is required in order to consider conditions in which the spin orientation can influence the electron energy, removing the energy degeneracy of electrons with opposite spin. Among the different effects in which spin is relevant, the Spin-Orbit Coupling (SOC) phenomenon can significantly alter the energy levels or the band diagram. This effect can be qualitatively justified considering that the electric field generated by the nucleus is actually felt as a magnetic field by the electron in a reference system at rest with respect to the electron. The magnetic field interacts with the magnetic moment associated to the electron spin, resulting into an additional energy contribution. Nevertheless, spin and SOC effect can be rigorously described only in the framework of the relativistic quantum mechanics. In this context, the resulting Hamiltonian $\mathcal{H}_{\mathcal{SOC}}$ associated to SOC is [77]:

$$\mathcal{H}_{\mathcal{SOC}} = \frac{1}{2m^2c^2}\frac{1}{r}\frac{\partial V}{\partial r}\hat{\mathbf{L}}\cdot\hat{\mathbf{S}}, \tag{2.19}$$

where

- V is the potential of the system;
- $\hat{\mathbf{L}}$ is the angular momentum operator;
- $\hat{\mathbf{S}}$ is the spin operator;
- c is the speed of light in vacuum.

In the simplest case in which V is the electrostatic potential of a Hydrogen-like system, equation 2.19 assumes the form:

$$\mathcal{H}_{\mathcal{SOC}} = \frac{1}{2m^2c^2}\frac{1}{4\pi\epsilon_0}\frac{Ze^2}{r^3}\hat{\mathbf{L}}\cdot\hat{\mathbf{S}}. \tag{2.20}$$

The peculiarity of this Hamiltonian term is the scalar product between the angular momentum and spin operators. The $\hat{\mathbf{L}} \cdot \hat{\mathbf{S}}$ operator presence requires the identification of a new set of operators that reciprocally commute with the Hamiltonian. In this framework the operator $\hat{\mathbf{J}} = \hat{\mathbf{L}} + \hat{\mathbf{S}}$ assumes a relevant role. Hence, states are now characterized by the quantum numbers j, m_j, l and s associated to $\hat{\mathbf{J}}^2$, $\hat{\mathbf{J}}_z$, $\hat{\mathbf{L}}^2$ and $\hat{\mathbf{S}}^2$ respectively. Electrons sharing the same quantum number l can have a different j, hence they are no more degenerate in energy. So, state splitting in energy is associated to the SOC intensity. Analysing equation 2.20, the dependence of the atomic number Z on SOC intensity is relevant and it is also encoded in r. Heavier nuclei are responsible for higher electron velocities, above all in the inner shells. The velocity increase turns into larger relativistic electron masses. Direct consequence of heavier electrons is a shrink of s and p orbitals. On the other hand, d and f orbitals tend to expand due to a better screening of the nuclear charge by the s and p electrons [78]. Hence, SOC energy contribution becomes proportionally more relevant for electrons of d and f orbitals in heavy atoms due to a more effective nucleus charge screening.

SOC effect influences both inner core and valence electrons. As more extensively discussed in paragraph 2.5.2, the role of the inner electrons can be lumped together to the nucleus charge in the pseudopotential approach. Hence, non-collinear spin description and relativistic effects must be considered in the generation of the pseudopotentials. For that reason, DFT calculations including the SOC contribution require specific pseudopotentials identified as fully-relativistic.

2.4 The Hellmann-Feynman theorem

The Hellmann-Feynman or force theorem identifies an effective way to evaluate the force acting on nuclei in a system composed by interacting nuclei and electrons. In analogy to classical mechanics, the force acting on a nucleus n can be associated to the gradient of the total energy with respect to the nucleus coordinates $\mathbf{R}_n$ as:

$$\mathbf{F}_n = -\nabla_{\mathbf{R}_n} E. \tag{2.21}$$

The total energy can be calculated through the evaluation of the expectation value of the system Hamiltonian $\mathcal{H}$ (2.22):

$$E = \frac{\langle \psi(\mathbf{R}) | \mathcal{H}(\mathbf{R}) | \psi(\mathbf{R}) \rangle}{\langle \psi(\mathbf{R}) | \psi(\mathbf{R}) \rangle}. \tag{2.22}$$

Combining equations 2.21 and 2.22, it is possible to evaluate the force acting on nucleus n. Nevertheless, the calculation of the gradient of the expectation value is not trivial since both the Hamiltonian $\mathcal{H}(\mathbf{R})$ and the system wavefunction $\psi(\mathbf{R})$ depend on the nucleus coordinates. The Hellmann-Feynman theorem [79],[80] states that the gradient of the energy expectation value is equivalent to the gradient acting only on

the Hamiltonian, if $\psi(\mathbf{R})$ is an eigenstate of $\mathcal{H}$. Hence the force acting on nucleus n is simply:

$$\mathbf{F}_n = -\frac{\langle\psi|\nabla_{\mathbf{R}_n}\mathcal{H}(\mathbf{R})|\psi\rangle}{\langle\psi|\psi\rangle}. \tag{2.23}$$

In other words, forces can be evaluated by knowing only the explicit dependence of each Hamiltonian term with respect to the nucleus coordinates.

This theorem is extensively employed in the next chapters 3, 4 and 5, when the geometrical minimum energy configuration of a system is unknown. In this case forces acting on different atoms are evaluated through Hellmann-Feynman theorem and atom positions are progressively updated to minimize the forces.

2.5 Practical aspects of DFT implementation

In this section some numerical details about DFT implementations are discussed. Even if this thesis work exploits an externally developed software (i.e., *Quantum Espresso* [81]) and not an in-house code, technical details are essential because they determine the accuracy of a simulation and will be extensively referred to in chapter 3.

2.5.1 Basis set

Common approach in quantum mechanics is the formulation of unknown wavefunctions as a linear combination of elements of a basis set. Common rationale is a mathematical complexity reduction due to specific properties of the selected basis set. According to this basis expansion approach, the wavefunction can be expressed as:

$$\psi_i(\mathbf{r}) = \sum_{j=1}^{\infty} c_j \phi_j(\mathbf{r}), \tag{2.24}$$

where $\phi_j(\mathbf{r})$ is an element of the basis set and c_j is the associated unknown coefficient. Notice equation 2.24 is strictly valid only if $\phi(\mathbf{r})$ is a complete set. Unfortunately, basis sets are usually composed by an infinite number of elements, hence 2.24 expansion is composed by an infinite number of terms. This summation must be truncated in numerical implementations, thus introducing an error in the wavefunction representation. For that reason, even if any complete basis set can be used in 2.24, commonly the selected family of functions should have a similar limiting behaviour with respect to the real wavefunction. This choice can guarantee an accurate approximation of the wavefunction through a limited number of basis elements.

2.5.1.1 Plane-wave basis set

A perfect crystalline structure is composed by a regular and periodic arrangement of ions. Hence, the electron system interacts with a periodic potential associated to the

lattice periodicity. In view of this periodic characteristic, the system wavefunction can be expressed as Bloch states as:

$$\psi_{i,\mathbf{k}}(\mathbf{r}) = u_{i,\mathbf{k}}(\mathbf{r})e^{i\mathbf{k}\cdot\mathbf{r}}, \tag{2.25}$$

where $u_{i,\mathbf{k}}$ is a function with lattice periodicity, i is the index associated to the band and the wave vector $\mathbf{k}$ is the crystal momentum vector of the considered state. For that reason, $u_{i,\mathbf{k}}$ can be expressed as a Fourier series with the reciprocal lattice vectors as wave-vectors $\mathbf{G}$:

$$u_{i,\mathbf{k}}(\mathbf{r}) = \sum_{\mathbf{G}} c_{i,\mathbf{G}} e^{i\mathbf{G}\cdot\mathbf{r}}. \tag{2.26}$$

Combining equations 2.25 and 2.26, the electron wavefunction is expressed as:

$$\psi_{i,\mathbf{k}} = \sum_{\mathbf{G}} c_{i,\mathbf{k}+\mathbf{G}} e^{i(\mathbf{k}+\mathbf{G})\cdot\mathbf{r}}. \tag{2.27}$$

Hence, the wavefunction $\psi_{i,\mathbf{k}}$ can be easily written as a linear combination of plane-waves; for that reason plane-waves are commonly used as basis set in equation 2.24. Unfortunately, the plane-wave basis set has an infinite dimension, hence, practically, only a limited number of plane-waves can be employed. Each plane-wave is identified by a specific $\mathbf{G}$ vector, however they are commonly regrouped according to their kinetic energy $E_k = \frac{1}{2}(\mathbf{k}+\mathbf{G})^2$ (in atomic units). It is reasonable that waves with lower energies are more physically important in the expansion than waves with very high energies. For that reason, only plane-waves with kinetic energy smaller than a threshold value (i.e., energy cutoff) are considered in 2.27. The identification of a suitable plane-wave energy cutoff is a critical step to achieve accurate results at a reasonable computational cost. For that reason, tests on the energy cutoff are extensively discussed in 3.1.1 and 3.2.1.

2.5.2 Pseudopotential theory

The previous paragraph 2.5.1 discusses the importance of accuracy in the basis expansion truncation and issues associated to finding a suitable energy cutoff. Specifically, core electrons are characterized by oscillating wavefunctions close to the nucleus position. Oscillations at short scale in real space are associated to high wave-numbers, therefore the description of core electron states generally requires high energy cutoff, and so high computational cost. However, core electrons are not especially important in defining the chemical bonding and other physical characteristics of the materials; indeed these properties are dominated by the less tightly bound valence electrons. For that reason, the pseudopotential theory is introduced to effectively consider core electrons, but at a reasonable computational cost. Conceptually, a pseudopotential replaces the electron density of a set of core electrons with a smoother density chosen to match various important physical and mathematical properties of the true ion

core. In other words, electrons of an atom are divided in two sets: the outer-shell electrons are explicitly treated and represented by wavefunctions in Hamiltonian equation, while the core states are not directly considered in the computation. Their role is embedded in an effective potential, responsible for representing both core states and the nucleus. The construction of pseudopotentials is a critical step because the effective potential in the pseudopotential (PP) approach should be able to exactly reproduce the atomic orbitals of the all-electron (AE) Hamiltonian. In practice, this condition is difficult to achieve, so commonly valence orbitals are only correctly represented. Different approaches for the pseudopotential construction have been proposed, resulting into different categories ('Norm-Conserving, 'Ultra-Soft', 'Projector Augmented-Wave' etc). Commonly accepted pseudopotentials for a wide range of atomic species and computational methods are Norm-Conserving [82],[83]. In this framework, pseudopotentials are developed so that the radial component of the atomic wavefunction $\phi_l^{PP}(r)$ predicted by the pseudopotential has some specific characteristics with respect to the analogous wavefunction $\phi_l^{AE}(r)$ associated to the all-electron Hamiltonian:

- $\phi_l^{PP}(r)$ must have no nodes, even if $\phi_l^{AE}(r)$ is characterized by nodes due to the oscillating behaviour close to the nucleus,
- $\phi_l^{PP}(r) = \phi_l^{AE}(r)$ at $r > r_c$ being r_c a selected cutoff radius,
- the eigenvalues of $\phi_l^{PP}(r)$ must coincide with the eigenvalues of $\phi_l^{AE}(r)$,
- $\int_0^{r_c} |\phi_l^{PP}(r)|^2 r^2 \, dr = \int_0^{r_c} |\phi_l^{AE}(r)|^2 r^2 \, dr$ i.e., pseudo-charge and true charge contained in the region $r < r_c$ must be the same.

In other words, PP behaviour must correctly represent the AE one at radial distances larger than a cutoff radius r_c, while $\phi_l^{PP}(r)$ can be smoother than $\phi_l^{AE}(r)$ at $r < r_c$, even if wavefunction norm must be preserved (i.e., norm-conserving).

Generally Norm-Conserving pseudopotentials are easily transferable (i.e., pseudopotential optimized for an isolated atom can be also effectively used when the atom is in any chemical environment without further adjustment). A drawback of Norm-Conserving pseudopotentials is a relatively higher energy cutoff with respect to other types as Ultra-Soft one. The latter, even if less computationally demanding, usually require a higher number of empirical parameters to be specified, hence their optimization is more complex.

2.5.3 Reciprocal-space integration and k-point sampling

According to Bloch theorem, periodic systems can be effectively studied limiting the analysis to the first Brillouin Zone (BZ) of the reciprocal k-space. Lots of physical quantities are evaluated integrating the contributions over the BZ. In any numerical

implementation, integrals are actually rewritten as summations. Hence common operations in a DFT computation are summations over the different k-points in the BZ. For example the electron density and the total energy are evaluated as:

$$n(\mathbf{r}) = \sum_{i}^{N_v} \sum_{\mathbf{k} \in BZ} |\psi_{i,\mathbf{k}}(\mathbf{r})|^2, \tag{2.28}$$

$$E_{tot} = \sum_{i}^{N_v} \sum_{\mathbf{k} \in BZ} \epsilon_{i,\mathbf{k}}, \tag{2.29}$$

where the index i runs on the number of the occupied bands in the valence band, for a total number of N_v bands.
The numerical evaluation of these summations can be computationally demanding due to the large number of k-points in the BZ. For this reason, different strategies are employed to speed up computation. In all cases, summations over the BZ must be truncated and only a limited set of k-points can be considered. Lots of states in the BZ are equivalent due to geometrical symmetry, hence the sampling of the BZ can be limited to an irreducible volume. An efficient sampling scheme is then applied to this irreducible wedge. The most adopted sampling scheme was developed by Monkhorst and Pack (MP) [84]. An MP grid is characterized by a mesh of equally spaced points along the directions identified by the three reciprocal lattice vectors. The grid is identified by three integers ($n_x \times n_y \times n_z$), each one specifies the number of sampled points in a direction. According to the system dimensionality, the mesh size in different directions can be the same or different. In all cases, a compromise between accuracy of the results and number of points in the summations is required to limit the computational cost. For that reason, paragraphs 3.1.2 and 3.2.1 are devoted to accuracy tests on the k-point sampling. In general, insulating or semiconductor materials allow for a coarser mesh, while metal systems are characterized by a denser k-grid to properly map the Fermi surface.

2.6 Activated processes and Nudged Elastic Band method

A common problem in chemistry and in solid state physics is the evaluation of the transition rate of a process. Indeed, even if a reaction from the initial to the final state is energetically favorable, it may not be spontaneous. In other words, the process must be activated in order to occur. The initial state must acquire sufficient energy in order to reach an intermediate activated state, after which the reaction becomes spontaneous and the external energy contribution is no more required. The energy increase with respect to the initial state, required to reach the activated states, is the activation energy of the process. Hence, the activation energy E_{act} is a key element in

the description of the velocity of a reaction. According to the Arrhenhius equation, the rate constant k of a reaction is:

$$k = Ae^{-\frac{E_{act}}{k_b T}}, \tag{2.30}$$

where A is the pre-exponential frequency factor, k_b is the Boltzmann constant and T is the temperature in Kelvin. In other words, the reaction occurs if the temperature of the system is sufficiently high so that, according to the statistical energy distribution, there is an appreciable number of reactant particles at energies larger than the activation energy.
In this framework, the evaluation of the activation energy is a central element in the description of a chemical reaction or the transition from physisorption to chemisorption state. The potential barrier associated to the activation energy can be evaluated analysing the 'Minimum Energy Path' (MEP) connecting the initial and the final configuration. Among the possible methods developed for the identification of the MEP, the Nudged Elastic Band (NEB) approach [85], [86] is commonly employed to map the energy profile of a system during a transformation. The given initial and the final configurations (initial and final images) are interpolated to generate a series of intermediate images representing an initial approximation of the path. Notice that intermediate images are not stable configurations, hence the minimization of all forces in these configurations would cause to slide away along the path from the high energy regions towards the minima. In order to effectively describe the intermediate configurations, a spring-like interaction between adjacent images is added. The true forces acting on the system and the fictitious spring forces are decomposed in components parallel and perpendicular to the tangent of the path for each image. The true forces perpendicular to the local tangent and the spring forces parallel to the path are the unique ones considered in the energy minimization process. According to this force minimization scheme, the intermediate image geometries are optimized, such that the estimated path converges to the true MEP. Indeed, the minimization of the true forces perpendicular to the path alone does not influence the distribution of the images along the path. On the other hand, the minimization of the spring forces parallel to the path does not interfere with the convergence of the path to the MEP since this type of forces only controls the spacing of the images along the path. Notice that the different images are not independent due to the reciprocal spring interactions, hence the force minimization in each image is performed considering the configurations of the adjacent images. All image geometries are continuously updated until forces are minimized in all configurations. The optimized intermediate images are then interpolated in order to reconstruct the full minimum energy path. In that way, it is possible to reproduce the energy variation profile during a transformation and estimate the energy barriers along the path.

CHAPTER 3

Computational approach and accuracy tests

This thesis work has been developed in the framework of Density Functional Theory (DFT), whose basic concepts are summarized in chapter 2. Simulations are performed with *Quantum Espresso* [81],[87],[88], an integrated suite of Open-Source computer codes for electronic structure calculations and material modeling at the nanoscale. Among all the exchange and correlation functional types developed in DFT frame, this thesis work employs the Pendew, Burke and Ernzerhof (PBE) [76] one since it is a well established GGA functional that is commonly exploited to reproduce structural and electronic properties for a wide range of materials. When molecule adsorption on defects is studied, semi-empirical corrections are included in order to consider dispersion interactions. Grimme's DFT-D3 [89] type of Van der Waals corrections is considered in this work. Norm-Conserving fully relativistic pseudopotentials are used in all simulations. They are generated by the code ONCVPSP (Optimized Norm-Conserving Vanderbilt Pseudopotential) fully-relativistic version 3.3.0 by D. R. Hamann [90]. An initial analysis is performed without including Spin-Orbit Coupling (SOC) effects (Section 3.1) and then it is compared to results with SOC (Section 3.2) in order to better identify the relevance of this relativistic effect on the structural and electronic properties. Analysis is restricted to the single cell and periodic boundary conditions are imposed to reproduce the full monolayer. The hexagonal cell of WS_2 is considered in this chapter: the lattice constant a, shown in Figure 3.1a, is initially set to its experimental value (a_{exp} = 3.153 Å [91],[92]). The height c of the cell in 3.1a represents the spacing between different layers in the bulk phase, so it should diverge in case of a monolayer structure. However, c value is set to 15 Å since this spacing is already sufficient to have negligible interaction between atomic layers in the framework of a DFT computation. Hence, each monolayer results completely isolated from its periodic replicas generated by imposing periodic conditions in the perpendicular direction.

Specifically, the cell of hexagonal 1H-WS_2 (the most stable phase and the most interesting one in optoelectronic applications), identified in bold in Figure 3.1a, is considered to fully exploit the system symmetries. The primitive cell is composed of

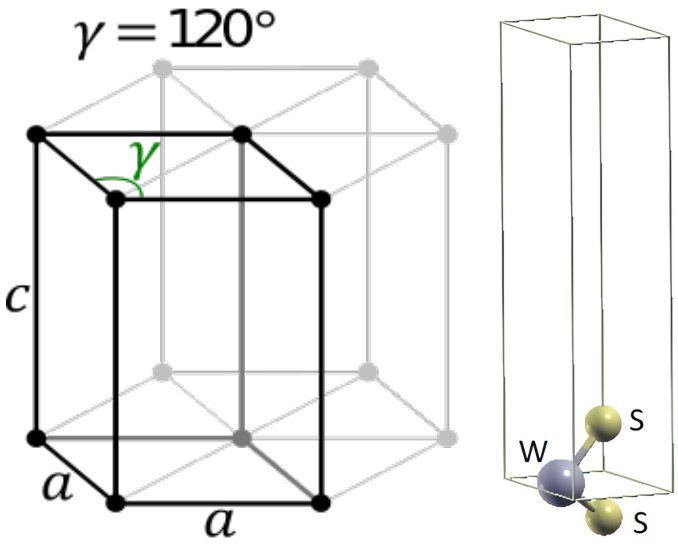

(a) Conventional hexagonal cell. (b) Primitive cell.

Figure 3.1: 1H-WS_2 crystal cell.

one W atom and two S atoms, as shown in 3.1b. Tests on plane-wave cutoff energy (Section 3.1.1) and reciprocal space sampling (Section 3.1.2) are considered in order to reach a compromise between accuracy and reasonable computation cost. Moreover, the atom positions are also optimized to identify the minimum energy configuration (Section 3.1.3). The system geometry is relaxed until all components of all forces are smaller than 10^{-4} Ry/Bohr and total energy between two consecutive steps changes less than 10^{-5} Ry. This set of tests aims at the identification of the simulation parameters effectively reproducing the WS_2 primitive cell, that can be exploited in the analysis of larger systems, where a higher computational cost limits the simulation test number.

3.1 Analysis without Spin-Orbit Coupling effect

The primitive cell of WS_2 in the 1H phase cell is analysed using a Norm-Conserving fully relativistic pseudopotential for both W and S. However, initially relativistic effects as Spin-Orbit Coupling (SOC) are not included. This preliminary analysis is carried out to better clarify the impact of these effects on geometry and band structure.

3.1.1 Plane-wave cutoff energy convergence

The identification of a proper cutoff energy value for the selected pseudopotentials is a preliminary step to guarantee a compromise between accuracy and reasonable computational time, as discussed in paragraph 2.5.1.1. A series of simulations with a wave-function cutoff variable between 10 Ry and 90 Ry with a interval step equal to 5 Ry is performed. For each simulation the total energy per primitive cell is evaluated.

Total energies per atom evaluated at different cutoff energies are reported in Figure 3.2.

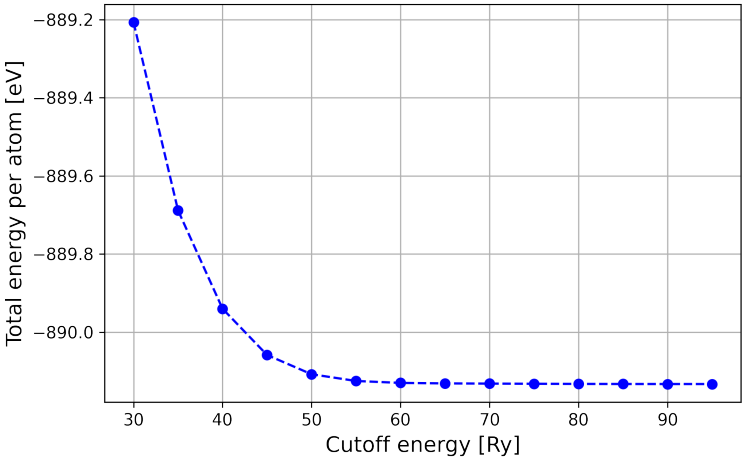

Figure 3.2: WS_2 primitive cell energies per atom at different cutoff energies.

We can immediately notice a decreasing trend in total energy for increasing cutoff values, in agreement with the variational theorem. However, it is also evident that large cutoff values result in negligible total energy variations. For this reason, the difference in energy between consecutive cutoff values is considered in order to have a more quantitative criterion for convergence identification. Absolute values of energy difference per atom at different cutoff values are reported in Figure 3.3.

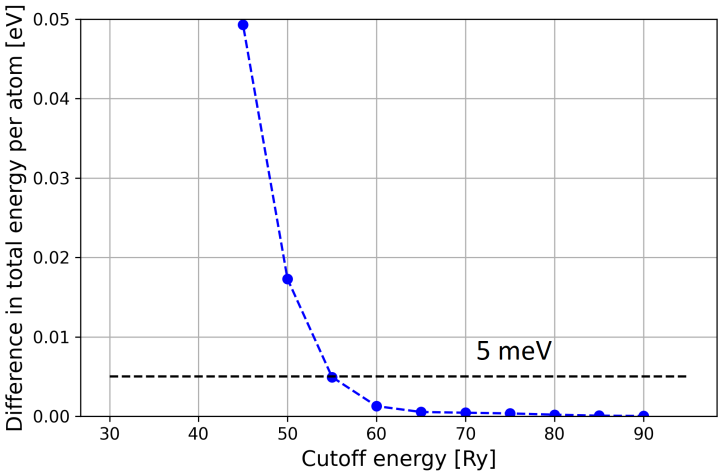

Figure 3.3: Energy difference in absolute value per atom in WS_2 at different cutoff energies.

Here 5 meV per atom is considered as a reasonable threshold below which energy

variations at higher cutoffs are assumed negligible. This condition is satisfied at a cutoff around 55 Ry and this value is used in the following tests on the WS_2 primitive cell.

3.1.2 K-points sampling convergence

A second important test deals with the accuracy of the k-point sampling of the first Brillouin Zone (BZ). Indeed, as discussed in paragraph 2.5.3, several quantities can be evaluated through summations over the BZ. Hence, a minimum set of k-points in the summation must be identified in order to get sufficiently accurate results at a reasonable computation time. The standard Monkhorst-Pack approach [84] is used in this thesis. A mesh of equally spaced points along the three reciprocal space primitive vectors is considered and it is identified by three integer numbers $n_x \times n_y \times n_z$. Considering that the simulated structure is a 2D material and the resulting BZ is bi-dimensional, there is no need of sampling along the third direction, i.e., $n_z = 1$. A series of simulations at increasing number of sampled k-points is performed considering grids from $3 \times 3 \times 1$ up to $8 \times 8 \times 1$. The cutoff energy is set to 55 Ry, as identified in paragraph 3.1.1. Convergence is obtained when the energy difference between consecutive MP grid cases is below 5 meV, as reported in Figure 3.4

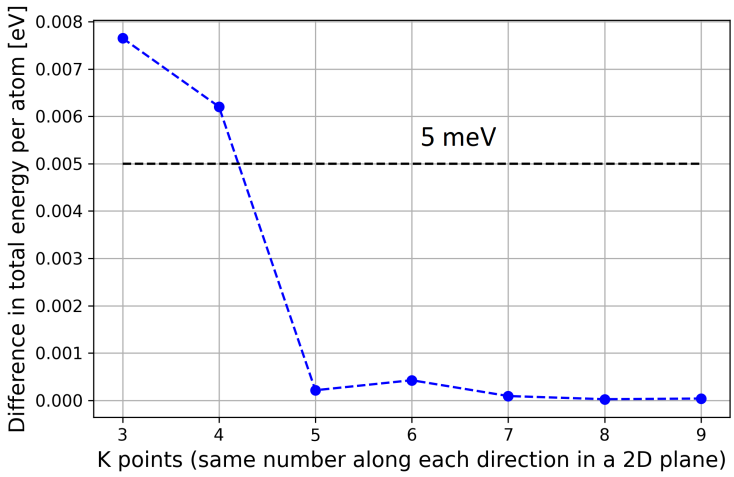

Figure 3.4: Energy difference in absolute value per atom in WS_2 at different MP grid sizes.

Notice that small grids already result in a small energy variation, however a relevant improvement is associated to the $5 \times 5 \times 1$. At higher grid dimensions the variation becomes very small and well below the assumed threshold. Next tests on the primitive cell are performed considering a $5 \times 5 \times 1$ grid, corresponding to 22 points in the irreducible BZ, due to system symmetries.

3.1.3 Equilibrium structure

Once the suitable cutoff energy for the chosen pseudopotentials (i.e. 55 Ry) and a proper k point grid (i.e., $5 \times 5 \times 1$) are identified, the cell geometry must be optimized in order to identify the equilibrium configuration. Relative atom positions are identified by three parameters as shown in Figure 3.5:

- lattice constant a of the hexagonal cell (i.e., the distance between two consecutive W atoms),
- distance d between top and bottom S planes within the same primitive cell,
- the bond length between W and S atoms.

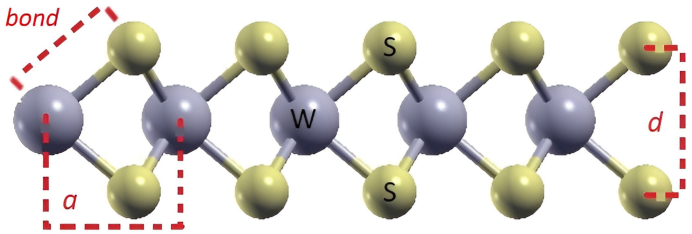

Figure 3.5: Main geometrical parameters of 1H-WS_2 monolayer.

The previous tests were performed considering the experimental values of geometrical parameters (i.e., $a_{exp} = 3.153$ Å, $d_{exp} = 3.142$ Å and W-S bond = 2.405 Å [91]), however these may not correspond to the predicted equilibrium geometry at DFT level. Notice that typically different functionals predict different minimum energy configurations. Band diagram and above all direct and indirect gaps are strongly influenced by small geometry variations [15]. For example, if the lattice constant is not properly identified, it is possible that the monolayer results in an indirect gap semiconductor. In view of the previous considerations, it is important to carefully identify the minimum energy geometrical parameters at DFT level. This task is performed simulating the primitive cell at variable a. Firstly an interval of 10 points from -10 % to +10 % around a_{exp} is considered and the total energy is evaluated at these lattice constants. Then a second smaller interval of 10 points from -5 % to +5 % around a_{exp} is analysed in order to have a finer interpolation mesh. Total energies per atom at different lattice constants are reported in Figure 3.6. An evident trend with a minimum energy point is appreciable and the experimental lattice constant (identified by the vertical orange line) is qualitatively close to the stationary point of the curve, proving the effectiveness of the selected pseudopotentials and functional. However, in order to have a more quantitative evaluation of the minimum energy lattice constant, total energies simulated at different a are fitted adopting a polynomial function. Fit results are shown in Figure 3.6 where the minimum energy a, according to the interpolation, is identified

by a green vertical line. Fitted minimum energy a is 3.177 Å, quite close to the experimental one (i.e., 3.153 Å). In the relaxed geometry associated to the identified lattice constant, the distance d between top and bottom S planes in the monolayer is 3.150 Å and the W-S bond length is 2.418 Å. Notice that these values are quite similar to the experimental ones (i.e., d_{exp} = 3.142 Å and 2.405 Å [91]) proving the simulation effectiveness.

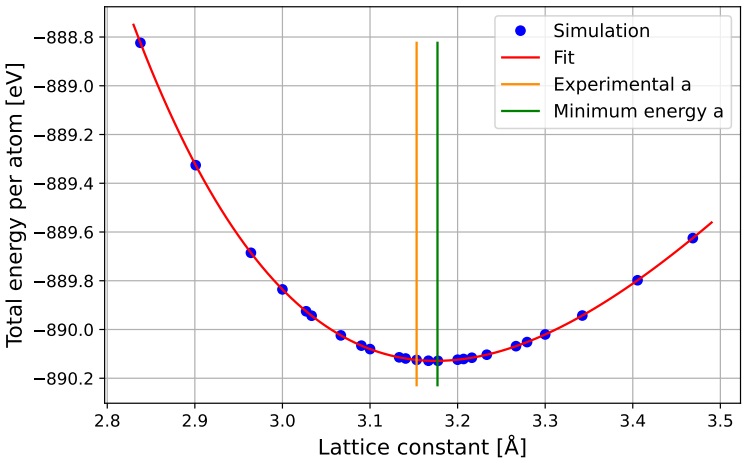

Figure 3.6: Fit of total energy at different a for WS_2, neglecting SOC.

3.1.4 Band diagram neglecting SOC

Considering the suitable cutoff energy (i.e., 55 Ry), k-space grid (i.e., $5 \times 5 \times 1$) and the optimized geometry (i.e., a = 3.177 Å, d = 3.150 Å and W-S bond = 2.418 Å), the band diagram is finally evaluated neglecting the SOC effect. This step is crucial in order to verify the predictive capability of the *ab initio* simulation and understand if selected parameters and functional are able to reproduce the main electronic signature of WS_2 monolayer.

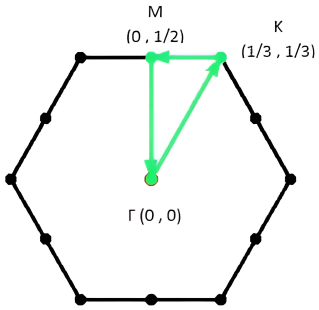

Figure 3.7: Analysed k path with high symmetry points reported in crystal coordinates.

The selected k path in the reciprocal space is reported in Figure 3.7 where the coordinates of high symmetry points are reported in crystal coordinates.
The band diagram evaluated along this path neglecting SOC is reported in Figure 3.8. The maximum of the valence band E_{VBM} is set to zero as energy reference.

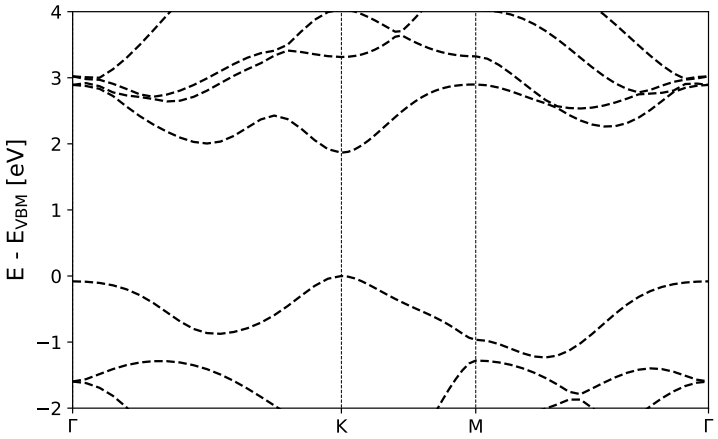

Figure 3.8: 1H - WS_2 monolayer band diagram neglecting SOC.

Simulated band diagram shows that WS_2, as monolayer, behaves as a direct gap semiconductor in the K point, in agreement with other DFT works [93], but also with experimental measurements [94]. However another relative minimum in the conduction band is present between Γ and K. Separation between two minima in conduction band is only 140 meV in this simulation, but this value can significantly vary according to the lattice constant. The direct band gap here evaluated neglecting SOC is 1.87 eV, in agreement with other DFT analyses in similar conditions (e.g., 1.95 eV in [93].) There is a significant mismatch (about 10 %) with the experimental evidence that shows a gap of about 2.05 eV [9]. However, underestimation of the electronic band gap is a well-known feature of functionals as PBE and more complete functionals have been developed [95]. Other relevant limit of simulated band diagram in Figure 3.8 is the exclusion of fully relativistic effects as SOC, that can significantly modify band structure. For that reason next section 3.2 is devoted to the analysis of WS_2 considering SOC effect.

3.2 Analysis with Spin-Orbit Coupling effect

As discussed in paragraph 2.3, Spin-Orbit Coupling (SOC) is a relativistic effect that can remove the energy degeneracy of electrons with opposite spin. This effect can be significant in Transition Metal Dichalcogenides (TMDs) as MoS_2 and WS_2, both in the bulk and monolayer phase [96]. Specifically SOC is enhanced in heavy metals as W and

Mo and their d orbitals are the main source of the Spin-Orbit interaction, as discussed in paragraph 2.3. For that reason, the introduction of this relativistic effect in the analysis of the primitive cell is required to verify the role of SOC in the gap value and in the band splitting. Adopted pseudopotentials are the same of previous section 3.1 (i.e., Norm-Conserving fully relativistic), but in this case a non-collinear computation is performed and SOC is considered. Accuracy tests and geometry optimization are performed also in this case to identify the new minimum energy configuration before band evaluation.

3.2.1 Plane-wave cutoff energy convergence and k-point sampling tests

Accuracy tests on the plane-wave cutoff energy and reciprocal space grid dimension are performed considering now SOC, but following the same approach of sections 3.1.1 and 3.1.2. Variations of the total energy per atom between consecutive cutoff values and different k grid dimensions are reported in Figure 3.9a and 3.9b respectively.

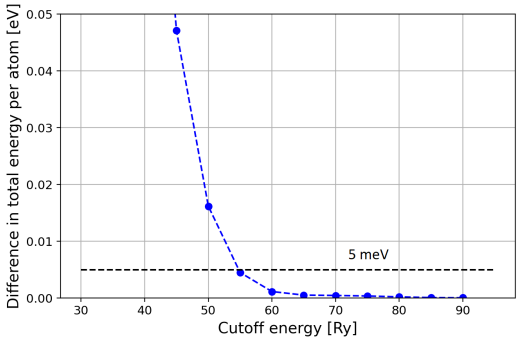

(a) Cutoff energy test.

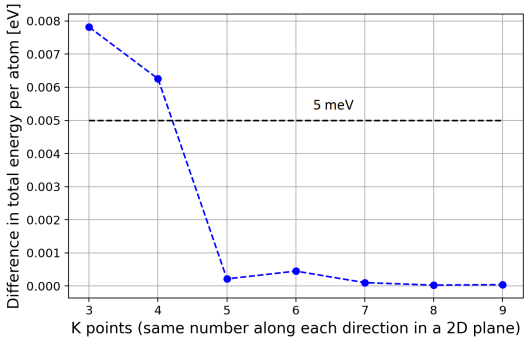

(b) K grid dimension test.

Figure 3.9: Convergence tests for WS_2 primitive cell including SOC.

Considering the use of the same pseudopotentials and the same approach, qualitatively the trend of Figures 3.9a and 3.9b is very similar to the curve profile of Figures 3.3 and

3.4 evaluated without SOC. Assuming the same convergence threshold of 5 meV per atom, the most suitable cutoff energy and MP grid dimension are 55 Ry and $5 \times 5 \times 1$ respectively, in agreement with the results of sections 3.1.1 and 3.1.2. Hence all next simulations on the primitive cell employ these parameters.

3.2.2 Equilibrium structure

Similarly to section 3.1.3, the minimum energy configuration of the primitive cell must be identified. In view of the previous discussed criticality of band variations in case of residual strain in the cell, it is important to consider also the small potential geometry modifications introduced by SOC with respect to the structure identified in paragraph 3.1.3. The optimization of the lattice parameter a is performed employing the same approach previously discussed. The result of the fit of total energy at different a is reported in Figure 3.10.

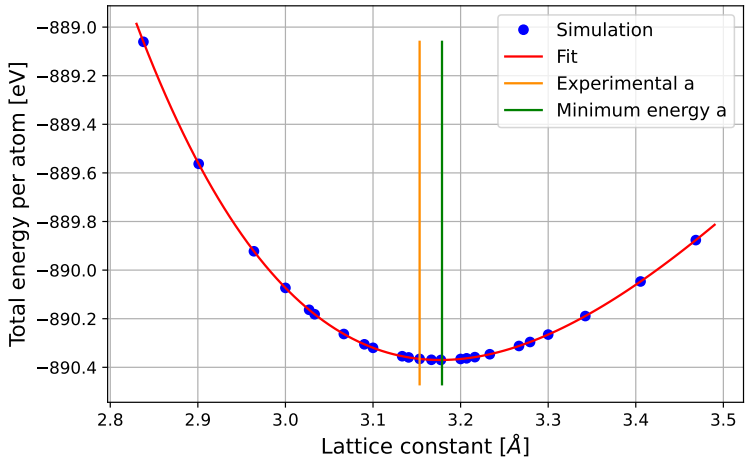

Figure 3.10: Fit of total energy at different a in WS_2 monolayer, including SOC.

The identified minimum energy lattice constant a is 3.179 Å, compatible with the experimental value (i.e., 3.153 Å).The most stable S plane separation d is 3.151 Å and the associated W-S distance is 2.419 Å.

The optimized geometry considering SOC is compared to the structure evaluated neglecting SOC as well as both experimental and other theoretical evaluations. Geometrical parameters are reported in Table 3.1 and ordered at increasing a.
Looking at Table 3.1, it is evident that geometrical parameters depend on the choice of the functional and more in general on selected pseudopotentials, cutoff energies etc... Hence a direct comparison among theoretical works is not immediate, however it is possible to identify some trends. For example LDA functionals tend to underestimate a, while GGA ones overestimate it [15]. This thesis work results are in agreement with this trend considering that estimated a are between the experimental and other PBE

Work	Approach	a [Å]	d [Å]
Ref. [15]	LDA + SOC	3.123	3.118
Ref. [91]	Exp.	3.153	3.142
This work	PBE	3.177	3.150
This work	PBE + SOC	3.179	3.151
Ref. [15]	PBE + SOC	3.192	3.140

Table 3.1: Comparison of geometrical parameters of 1H-WS_2 primitive cell.

work values. Comparing the evaluated parameters within this work, the introduction of SOC is responsible for only a very small variation in the geometry. Even if the structural parameters are almost the same considering or neglecting SOC, the relativistic effects strongly modify the band diagram, as discussed in the following paragraph 3.2.3.

3.2.3 Band diagram considering SOC

Considering the suitable cutoff energy (i.e., 55 Ry), k-space grid (i.e., $5\times5\times1$) and optimized geometry (i.e., $a = 3.179$ Å, $d = 3.151$ Å and W-S bond = 2.419 Å), the band diagram is finally evaluated considering the SOC effect. The path in the reciprocal space is the same as in Figure 3.8. The evaluated band diagram is reported in Figure 3.11 and compared to another theoretical band evaluation at similar conditions (PBE + SOC, Norm-Conserving pseudopotentials [15]). Despite the different geometrical

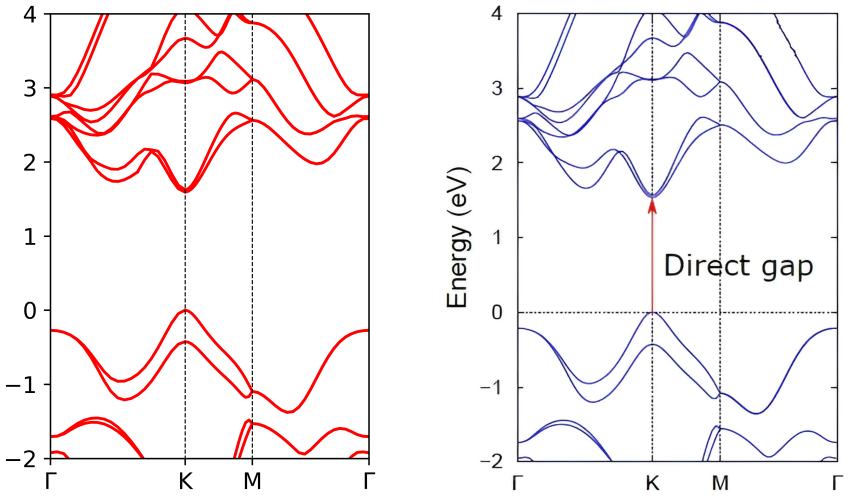

Figure 3.11: Comparison of the WS_2 band diagram obtained in this work (on the left) and the results reported in Reference [15] (on the right), considering SOC.

parameters adopted in [15], there is a good agreement in band profiles, confirming the effectiveness of previous paragraph accuracy tests and geometry optimization. Evaluated direct band gap equal to 1.61 eV is also comparable to the value estimated in [15] (1.55 eV).
Once the validity of band diagram with SOC is confirmed, a detailed comparison with the previous evaluated diagram without SOC (3.8) is reported in Figure 3.12.

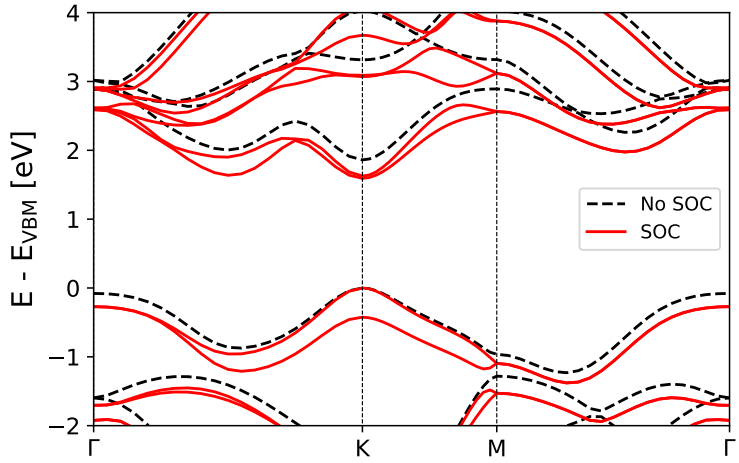

Figure 3.12: Comparison of 1H - WS_2 monolayer band diagrams neglecting (dash black line) and considering SOC (solid red line).

The main effect of SOC is the removal of spin degeneracy, resulting in a splitting of bands along the Γ-K and K-M directions. For example, considering the K point, the lowest conduction band is split in two branches separated by about 32 meV. The splitting is more evident in the highest valence band since it is about 425 meV. These values are compatible with other theoretical simulations (29 meV and 431 meV for the lowest conduction band and the highest valence band respectively [97]). Another significant modification introduced by SOC is a reduction of the direct band gap as visible in Figure 3.12 and confirmed by other theoretical works [93]. The gap without SOC (1.87 eV) drops down to 1.61 eV, resulting into a large underestimation of the experimental value (2.05 eV [9]). As already discussed, this is a well known limit of the DFT-PBE approach and reported in several theoretical works [96],[15],[97]. More precise evaluations of the gap are possible using hybrid functionals (e.g, HSE) or adopting more complex approaches (e.g., GW), but requiring high computational costs [95]. Nevertheless, this thesis work adopts a DFT-PBE approach, since it is already able to predict some key features of the band diagram although with these limitations. SOC is also always considered in next simulations since the splitting due to SOC is essential in the description of in-gap states in defective monolayers [15], as discussed in next chapter 4.

CHAPTER 4

WS_2 point defect analysis

Defects have a stronger impact on the properties of 2D materials than on those of their bulk counterparts, as discussed in paragraph 1.2.2. For that reason a detailed analysis of defects in WS_2 monolayers is required to understand how the electronic properties of the pristine monolayer are changed. This chapter only focuses on unintentional point defects. Indeed, this thesis work aims at the analysis of molecule adsorption on defect sites, independently of the specific intentional doping used to tailor the material properties. Here, we select only three types of unintentional point defects (i.e., sulphur vacancy V_S, oxygen as sulphur substituent O_S and chromium as tungsten substituent Cr_W) since they are the most common according to experimental evidences, as discussed in paragraph 1.2.2. Initially the problem of the simulation domain size is discussed in section 4.1 in order to properly describe isolated defects. These considerations are then applied to specific defect cases. The formation energies of the defects are studied in paragraph 4.2 in order to identify how easily these defects are unintentionally introduced. Then, the defect electronic signature is fully analysed for each case, describing not only the band diagram, but also the Projected Density of States (PDOS) and the electron density isosurfaces associated to the defect states.

4.1 Supercell approach

Defects are periodicity perturbations in a perfect crystalline structure. As discussed in section 2.5.1.1 and applied in chapter 3, an efficient way to describe periodic systems relies on the analysis of a single cell with periodic boundary conditions. Even if the analysed defects are 0D, they cannot be studied considering only the repetition unit shown in Figure 3.1b, since defects are local, isolated in a real system and not spread in each primitive cell. For that reason, in the framework of plane-wave DFT, the supercell approach must be employed to describe defects, while retaining the periodicity at the same time. This method identifies a larger minimal repetition unit; instead of a single primitive cell composed by three atoms, a piece of monolayer composed by more

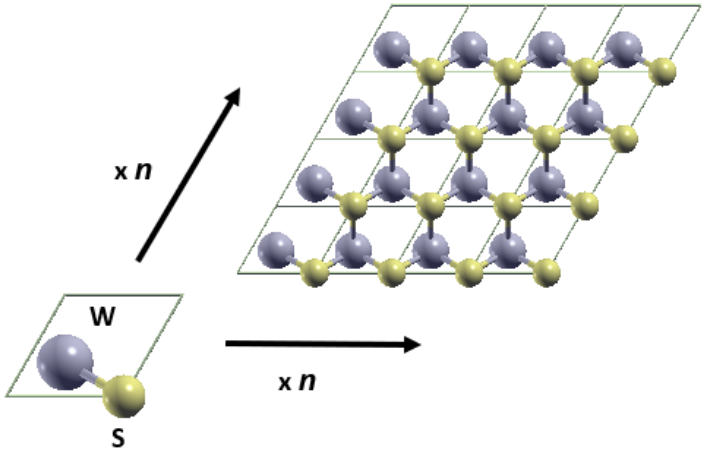

Figure 4.1: Construction of a $n \times n$ supercell.

hexagonal cells (i.e., a supercell) is studied, as shown in Figure 4.1. Periodic conditions on this larger repetition unit result in a monolayer with point defects periodically arranged. Despite this apparently nonphysical description due to the randomness of the defect positions in the real samples, this approach is effective if each defect is sufficiently spaced from its periodic replicas in order to behave as isolated. This requirement implies that supercell size must be sufficiently large (i.e., composed by a sufficiently large number of primitive cells of pristine WS_2) to mimic single "diluted" defects. Nevertheless, a larger supercell results in a larger number of simulated atoms. For that reason, the optimal supercell size is a compromise between sufficiently isolated defects and a reasonable computational cost. Several features can be analysed to understand if the supercell dimension is suitable. Isolated point defects are usually characterized by dispersionless states. Hence, by progressively increasing the supercell dimension, defect states progressively become "flatter" since they are more and more isolated. Secondly, if defects are isolated, they often introduce only specific states. Most of the band diagram strictly associated to pristine atoms is usually unchanged. This implies that, at increasing supercell dimension, the main features of the band diagram (e.g., the gap) should converge to the pristine WS_2 case. Finally, if defects are completely isolated, their formation energy should become independent from the supercell size.

Practically, the supercell is assembled considering the cell reproduced in Figure 3.1b and replicating it n times in both directions of the plane, as shown in Figure 4.1. The parameters of the single WS_2 primitive cell are those identified in paragraph 3.2.2 (i.e., $a = 3.179$ Å and $d = 3.151$ Å), considering SOC. The cutoff energy is equal to 55 Ry, if not specified otherwise. The k-point grid is reduced with respect to the previously identified one (i.e., $5 \times 5 \times 1$) since the increase of the superlattice constant (na instead of a) is responsible for a inversely proportional reduction of the BZ dimension. Hence, the k-space grid is reduced to $2 \times 2 \times 1$ in 3×3 and 4×4 supercells, to $1 \times 1 \times 1$ in

5×5 and 6×6 supercells.

4.2 Formation energy for defects

Firstly, the formation energies E_{FORM} of all unintentional defects are evaluated to understand how easily they can occur. E_{FORM} is evaluated as:

$$E_{\mathrm{FORM}}[\mathrm{X}] = E_{\mathrm{TOT}}[\mathrm{X}] - E_0 + n_{\mathrm{W}}\mu_{\mathrm{W}} + n_{\mathrm{S}}\mu_{\mathrm{S}} - \sum_{\mathrm{X}} n_{\mathrm{X}}\mu_{\mathrm{X}}, \tag{4.1}$$

where:

- $E_{\mathrm{TOT}}[\mathrm{X}]$ is the energy of the supercell with the defect,
- E_0 is the total energy of the pristine supercell (i.e. without any defect),
- n_{W} and n_{S} are the numbers of W and S atoms removed from the layer,
- μ_{W} and μ_{S} are the chemical potentials of tungsten and sulphur, respectively, in their stable bulk phases,
- n_{X} is the number of substituent X atoms added to the system,
- μ_{X} is the chemical potential of species X in its stable bulk phase.

Table 4.1 resumes the analysis on the bulk stable phases employed to evaluate the chemical potentials of the different atomic species, specifying the type of phase and the suitable cutoff energy.

Atomic species	Reference phase	Cutoff energy [Ry]
W	crystal tungsten, FCC	55
S	α-Octasulfur, orthorhombic	40
Cr	crystal chromium, FCC	80
O	O_2 molecule	75

Table 4.1: Recap of the analysis of stable bulk phases for the different atomic species.

The formation energies for the different defects are evaluated through equation 4.1 at increasing supercell size, but the results in Table 4.2 refer to the optimal size of the supercells. The suitable energy cutoff values are also reported.

Sulphur vacancies are characterized by the highest formation energy and it is unlikely that this defect occurs spontaneously. This result is in agreement with the experimental evidences discussed in section 1.2.2.1: CVD 'as-grown' samples do not show V_{S}, but chalcogen vacancies are created in subsequent high temperature annealings.

Defect	V_S	O_S	Cr_W
Supercell size	5×5	5×5	6×6
Cutoff energy [Ry]	55	75	80
E_{FORM} [eV]	2.83	-1.35	0.35

Table 4.2: Formation energies of unintentional defects.

On the other hand, the negative formation energy of O_S proves that spontaneously O atoms are incorporated in WS_2 monolayers. This result is again confirmed by the experimental evidences discussed in section 1.2.2.1: O atoms spontaneously passivate S vacancies during the synthesis or simply due to air oxidation. Whereas the substitution of W with Cr requires an external energy contribution, as shown by its positive formation energy. It is sufficiently large to avoid the Cr incorporation at room temperature, nevertheless, Cr impurities are present in the W precursor, hence the formation energy is sufficiently small to allow Cr_W creation due to the temperatures achieved during the synthesis. This confirms the possibility of Cr presence in the monolayer after the synthesis.

The discussed approach for the formation energy evaluation assumes that the energies of atoms added/removed are referred to the chemical potential of the corresponding atoms in their stable bulk phase. Nevertheless, in practical situations, atoms are not directly obtained from their bulk reference phase, but they initially belong to their precursor species. For that reason, the formation energies should be expressed considering the chemical potentials of atoms in the precursors as energy references. Hence, the chemical potential for W(S) $\mu_{\mathrm{W(S)}}$ is expressed as $\mu_{\mathrm{W(S)}} = \mu^0_{\mathrm{W(S)}} + \Delta\mu_{\mathrm{W(S)}}$, where $\mu^0_{\mathrm{W(S)}}$ is the potential of the reference bulk phase for W(S) reported in Table 4.1 and $\Delta\mu_{\mathrm{W(S)}}$ is the term accounting for the possible variations of the chemical potential with respect to the reference bulk phase [98], [99]. In order to guarantee the correct stoichiometric ratio between W and S, the thermodynamical equilibrium requires μ_{WS_2} $= \mu_W + 2\mu_S$. Defining $\Delta\mu = \Delta\mu_S$ - $\Delta\mu_W$, equation 4.1 can be effectively rewritten as:

$$E_{\mathrm{FORM}}[\mathrm{X}] = E'_{\mathrm{TOT}}[\mathrm{X}] - \left(\frac{2}{3}n_{\mathrm{W}} - \frac{1}{3}n_{\mathrm{S}}\right)\Delta\mu - \sum_{\mathrm{X}} n_{\mathrm{X}}\mu_{\mathrm{X}}, \tag{4.2}$$

where $E'_{\mathrm{TOT}}[\mathrm{X}]$ is defined as:

$$E'_{\mathrm{TOT}}[\mathrm{X}] = E_{\mathrm{TOT}}[\mathrm{X}] - E_0 + \left(\frac{2}{3}n_{\mathrm{W}} - \frac{1}{3}n_{\mathrm{S}}\right)(\mu^0_{\mathrm{W}} - \mu^0_{\mathrm{S}}) + \left(\frac{1}{3}n_{\mathrm{W}} + \frac{1}{3}n_{\mathrm{S}}\right)\mu_{WS_2}. \tag{4.3}$$

By introducing the enthalpy of formation of the WS_2 monolayer $\Delta H_{WS_2} = \mu_{WS_2}$ - μ^0_{W} $-2\mu^0_{\mathrm{S}}$, it is possible to define a meaningful range for the chemical potential variation:

$$\Delta H_{WS_2} < \Delta\mu < -\Delta H_{WS_2}. \tag{4.4}$$

The formation energy in equation 4.2 can be plotted as a function of the chemical potential variation $\Delta\mu$ within the limits of equation 4.4. Results are reported in Figure 4.2. Supercell sizes and cutoff energies for the different defect types are reported in Table 4.2.

V_S formation energy is always high both in the W-rich (left side of Figure 4.2) and S-rich (right side of Figure 4.2) limit, preventing the spontaneous formation of this type of defect. At the same time, O_S is always spontaneous, even if the formation energy increases when there is abundance of S atoms as competitor. Finally, Cr_W formation requires an external energy contribution in case of the W-rich limit, but its formation becomes spontaneous in case of W deficiency.

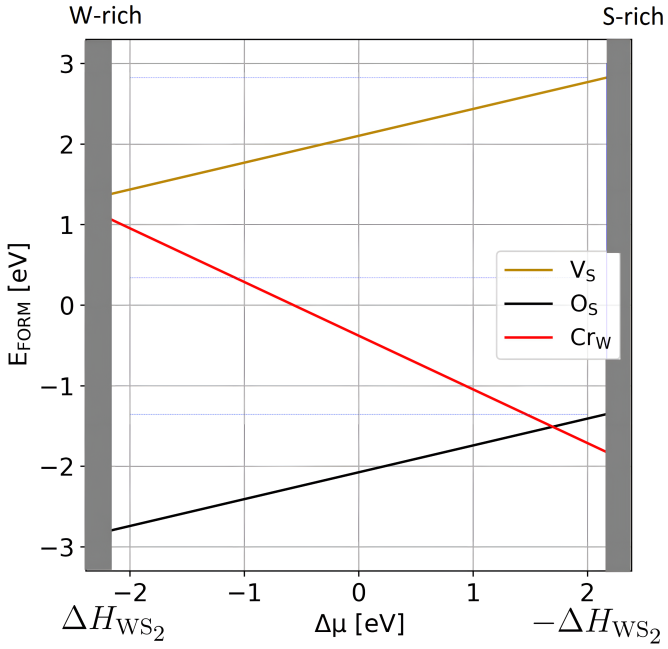

Figure 4.2: Formation energies of unintentional defects in WS_2 monolayer as a function of $\Delta\mu$.

4.3 Sulphur vacancy

Sulphur vacancies V_S is the most widely discussed type of unintentional defect in WS_2 monolayers. Supercells with V_S at progressively increasing dimension from 3×3 up to 5×5 are analysed. For each case, the initial geometry is equivalent to the structure of a pristine supercell of the same dimension, except for the removal of an S atom. Then, a relaxation process is performed on the initial geometry in order to identify the most stable configuration when an S atom is missing. An example of the relaxed structure in the 3×3 supercell is shown in Figure 4.3.

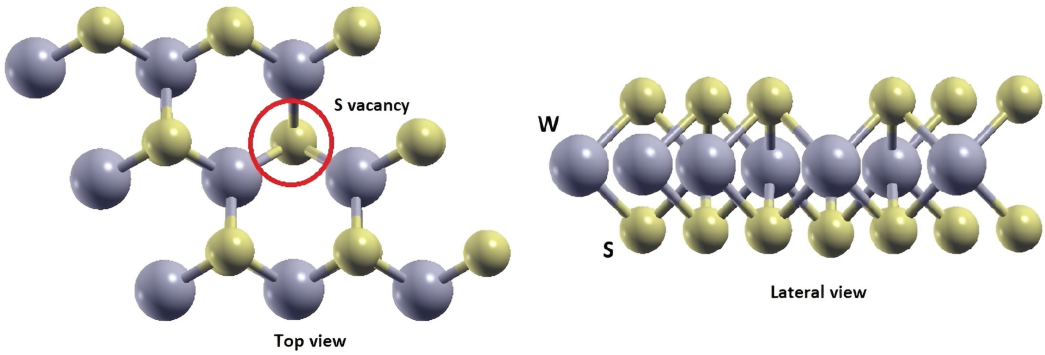

Figure 4.3: Relaxed 3×3 supercell with V_S.

The effects of the structure relaxation in absence of an S atom can be quantified by analysing the distance between two W atoms in proximity of the vacancy. The W-W distances for different supercell sizes are reported in Table 4.3. The missing S atom allows W atoms to expand towards the vacancy site, reducing the W-W distance with respect to the pristine condition. This effect is more evident in larger supercells since the stress induced by deformation can be redistributed on a larger number of atoms.

V_S supercell	3×3	4×4	5×5	Pristine
W-W distance [Å]	3.056	3.042	3.036	3.179

Table 4.3: Comparison of the W-W distance in proximity of V_S at different supercell size.

Once the structural variations due to V_S have been analyzed, the effects on the electronic properties are discussed by evaluating the band diagram at different supercell dimensions. Figure 4.4 shows the band diagrams of the 3×3, 4×4 and 5×5 supercells with a single V_S. The maximum of the valence band E_{VBM} is set to zero as energy reference, while the Fermi level is plotted with a dashed red line.

The apparently larger number of visible bands in Figure 4.4 with respect to the diagram in Figure 3.11 is associated to the decrease of the BZ dimension, when the repetition unit is enlarged to a supercell. Hence, bands that are inside the unit cell BZ (UCBZ), are folded into the smaller supercell BZ (SCBZ), resulting into a larger number of visible bands. This happens because points in the UCBZ, that are outside the SCBZ, are mapped to equivalent points inside the SCBZ. For example, the K point (1/3, 1/3, 0) in the UCBZ is folded on the Γ point (0, 0, 0) of the 3×3 supercell BZ. Despite the band complexity increase due to the supercell approach, the main electronic features of the system can be easily identified. For example, the vacancy does not alter the direct band gap nature in K of the WS_2 monolayer. Nevertheless, the gap value depends on the supercell dimension, as shown in Table 4.4. The gap

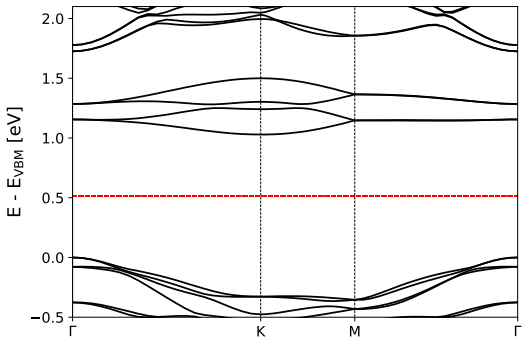

(a) 3×3 supercell.

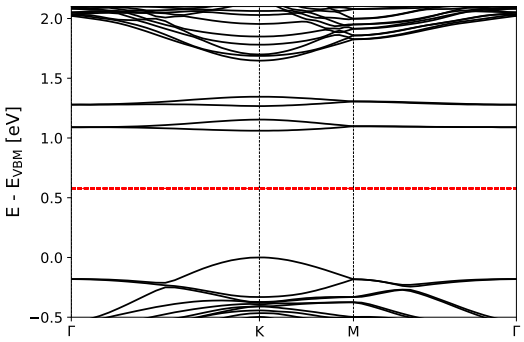

(b) 4×4 supercell.

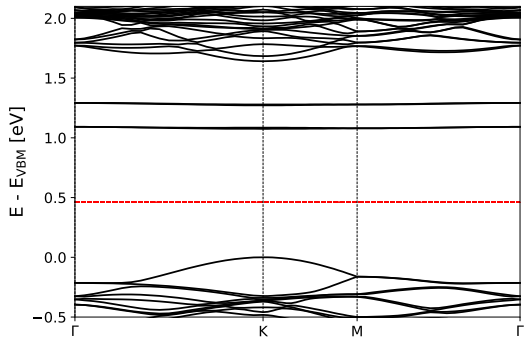

(c) 5×5 supercell.

Figure 4.4: Band diagrams at different WS_2 supercell dimension with V_S (the Fermi level is depicted with a red dashed line).

value drops with supercell increase and is almost converged to the pristine value in the 5×5 structure, proving that the defect is appreciably isolated, as discussed in section 4.1.

V_S supercell	3×3	4×4	5×5	Pristine
E_g [eV]	1.72	1.65	1.64	1.61

Table 4.4: Comparison of the direct band gap value in different WS_2 supercells with a single S vacancy.

The main feature associated to V_S is the formation of defect states well within the gap. They are clearly two couples of bands, composed by two states each, as shown in Figure 4.4a. However, their dispersion is significantly reduced when defects are more isolated from their periodic replicas in larger supercells, as discussed in section 4.1. The defect states degenerate in two completely 'flat' levels in the 5×5 supercell. The

convergence of the gap value and the dispersionless defect states in the 5×5 supercell prove that this supercell dimension is suitable to describe isolated defects. For that reason, the analysis of the electronic properties associated to V_S is performed in the 5×5 supercell.

In order to better characterize the S vacancy, the band diagram together with the Density of States decomposed in the different atomic species contributions (i.e., the Projected Density of States or PDOS) are plotted in Figure 4.5a. For comparison, a 5×5 supercell without defects is also reported in Figure 4.5b in order to better point out the vacancy contributions.

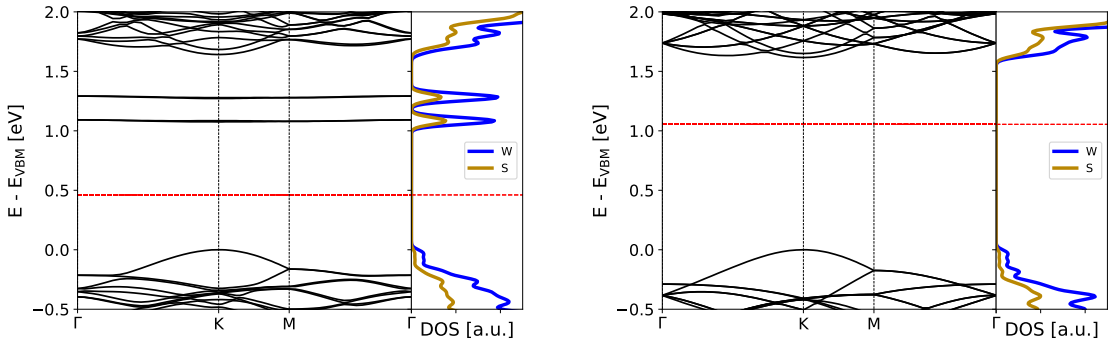

(a) S vacancy.

(b) Pristine.

Figure 4.5: Band diagram and PDOS of the 5×5 WS_2 supercell (the Fermi level is depicted with a red dashed line).

The presence of two in-gap defect states below the conduction band due to the S vacancy is further confirmed; however now we can notice that S, but above all W atoms are responsible for the defect states, as shown in the PDOS panel in Figure 4.5a. In addition we can observe that these states are unoccupied and an analysis neglecting SOC reveals that the splitting of these states is associated to this relativistic effect. Their energy separation is about 0.2 eV. These simulation results are perfectly in agreement with the experimental LDOS reported in Figure 1.5a: two unoccupied defect states split by 252 meV due to SOC are the main electronic signature of V_S from the experimental standpoint, as discussed in 1.2.2.1. Despite many works claim that V_S might be responsible for the unintentional n-doping in WS_2 monolayers [100], the identified defect states cannot act as donor levels since they are unoccupied when the monolayer is analysed as isolated. Hence, the origin of the n-doping in WS_2 is more probably associated to impurities trapped between the flakes and the substrate [101] or carrier transfer mechanisms from the substrate [102].

The contribution of S and W atoms in the band diagram is further investigated analysing the k-resolved PDOS. The PDOS in Figure 4.5 is evaluated summing together the contributions of all states at the same energy, while the k-resolved PDOS,

represented in Figure 4.6, considers the PDOS for each state resolving in energy as well as in k vector. For each state the relative contribution of the atomic species is associated to the color shades: cyan is associated to W while yellow is associated to S.

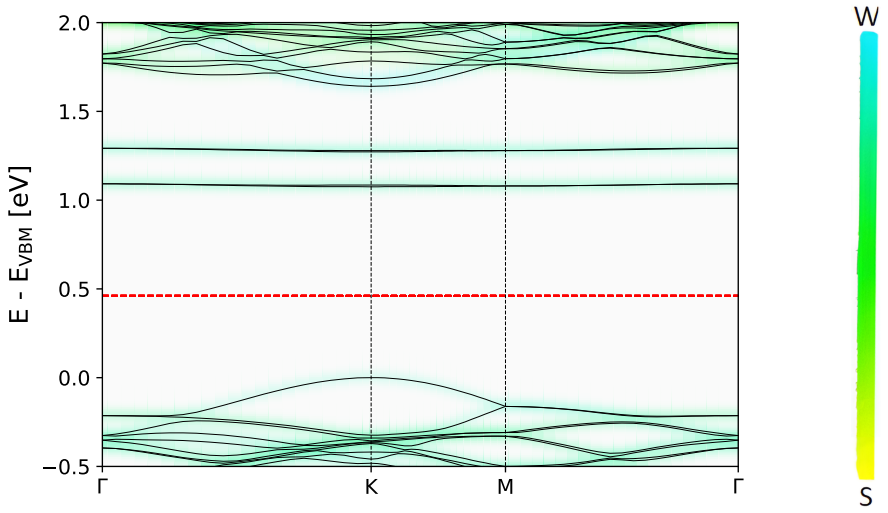

Figure 4.6: K-resolved PDOS of the 5×5 WS_2 supercell with a single S vacancy (the Fermi level is depicted with a red dashed line).

The uniform color along the in-gap defect states further proves that they are k independent (i,e., dispersionless). Moreover the green towards cyan color of the defect states confirms the predominance of W over S contribution. At the same time, the bottom of the conduction band and the top of the valence band in K are characterized by the predominance of W contribution, as occurs in the pristine case, further proving that V_S does not strongly alter other states in the band diagram.

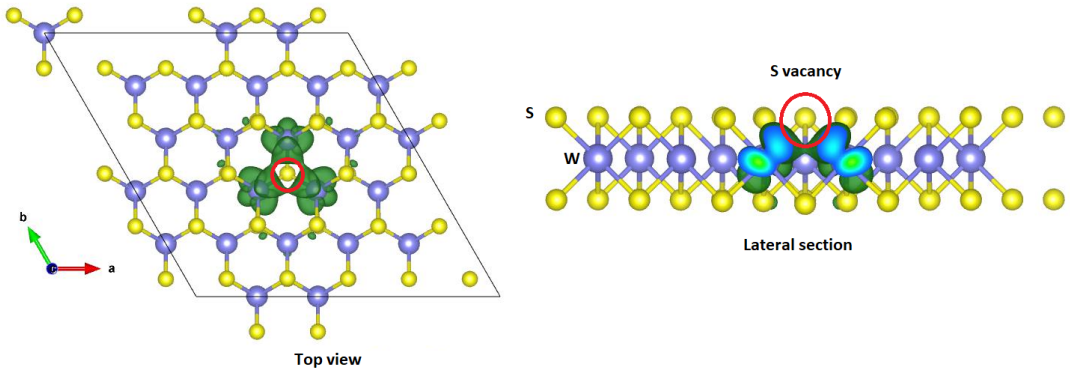

Figure 4.7: Charge density isosurface associated to the 1st defect state due to V_S in WS_2 monolayer (isosurface value = 0.0014 a.u.).

Finally, the localized nature of the defect states is further evaluated by plotting the isosurface of the charge density associated to these states. Figure 4.7 shows the charge density associated to the lowest defect state; the plot of the highest defect state is not reported due to its similar features. The density is clearly localized close to the vacancy site, above all in the S plane with the missing atom, as shown by the lateral section, proving that the 5×5 supercell is sufficiently large to have isolated and localized defects.

4.4 Oxygen as substituent of sulphur

Oxygen is the most common substituent atom of sulphur and it can passivate V_S. Similarly to the approach of section 4.3, different supercells at progressively increasing size are simulated. Considering that the O atom has a smaller atomic radius than the S one, the atom position in the supercells are properly relaxed in order to minimize the force induced by the presence of a smaller atom. An example of relaxed structure in the 3×3 supercell is shown in Figure 4.8. The O atom is exactly aligned over the S atom of the bottom plane, however it is located well below the surface of the top sulphur plane. This evidence is also confirmed experimentally, as discussed in section 1.2.2.1. The distance decrease of O atom with respect to the W plane is reported in Table 4.5 for the different supercells and is compared to the S atom distance from the W plane in the pristine cell. The O atom height decreases of about one third of the original position and this effect is slightly more evident in large supercells.

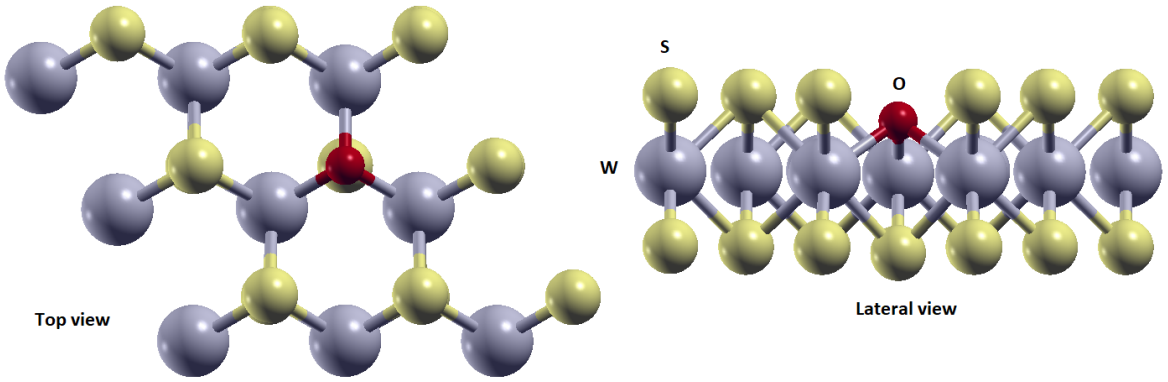

Figure 4.8: Relaxed 3×3 supercell with a single O_S.

Supercell	3×3	4×4	5×5	Pristine
O - W plane distance [Å]	1.08	1.05	1.03	1.58

Table 4.5: Comparison of O_S - W plane distance at different WS_2 supercell size.

Once the structural properties have been discussed, the band diagram of supercells with an oxygen substituent at different size are evaluated. For the sake of simplicity, only the band diagram of the 5×5 supercell is reported in Figure 4.9a. The main peculiarity of the band diagram associated to O_S is the complete absence of in-gap defect states. This result is completely in agreement with experimental evidence, as discussed in section 1.2.2.1 and shown in Figure 1.5b. The unique variation in the band diagram among the different supercells is associated to the direct band gap value, as reported in Table 4.6. The direct gap in the 3×3 supercell is already close to the pristine case; nevertheless, the best match is in the 5×5 one. For this reason, whole analysis of O_S is performed in the 5×5 supercell. Until now all simulations have been performed at the cutoff energy equal to 55 Ry since it is the optimal value for the W e S pseudopotentials, as identified in paragraph 3.2.1. However, the oxygen pseudopotential is also employed in the O_S analysis. The study of the O_2 molecule shows that 75 Ry is the optimal energy cutoff for the O pseudopotential. For that reason, the 5×5 supercell is also simulated at 75 Ry, but the resulting band diagram and above all the direct gap do not change significantly, as shown in Table 4.6.

Supercell	3×3	4×4	5×5	5×5	Pristine
Cutoff energy [Ry]	55	55	55	**75**	55
E_g [eV]	1.57	1.59	1.60	1.60	1.61

Table 4.6: Comparison of the direct band gap value at different WS_2 supercell size with O_S and at different cutoff energies.

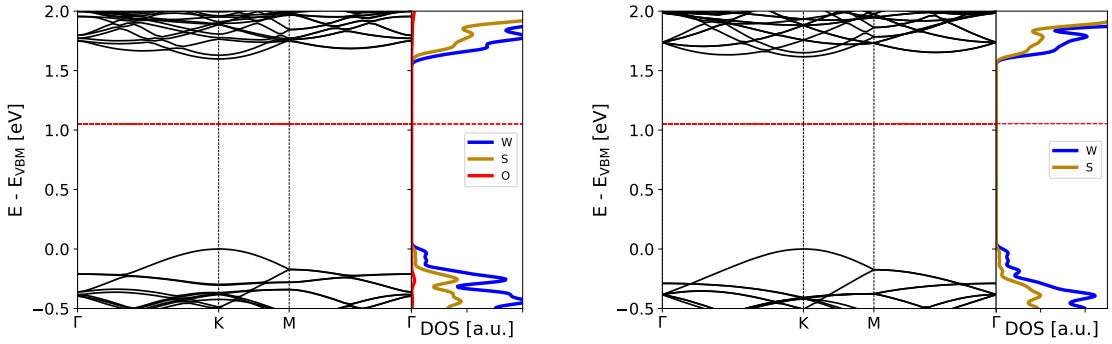

(a) O substituent.

(b) Pristine.

Figure 4.9: Band diagrams and PDOS of the 5×5 WS_2 supercell (the Fermi level is depicted with a red dashed line).

Figure 4.9 compares the band diagram in the case of O_S and the correspondent 5×5 pristine supercell. Aside some minor modifications in the valence band, the two

band diagrams are quite similar. Indeed, looking at the PDOS in Figure 4.9a, the contribution associated to the O species is spread both in valence and conduction band and does not have a major role at any energy. The similarity of O_S and the pristine band diagram is associated to the isovalence nature of O and S species. No dangling bonds or a different number of electrons are introduced when S is replaced by O. A more careful analysis of Figure 4.9 shows the presence of a band characterized by a reduced dispersion, just below the valence band top in case of O_S. A small bump in the PDOS associated to O species is also present in the same energy range. In order to better clarify the nature of this band, the k-resolved PDOS in the 5×5 supercell is reported in Figure 4.10. The relative contribution of the different atomic species is codified in the color shades: predominance of W, S and O contribution is associated to cyan, yellow and magenta respectively, as shown in the color triangle in Figure 4.10.

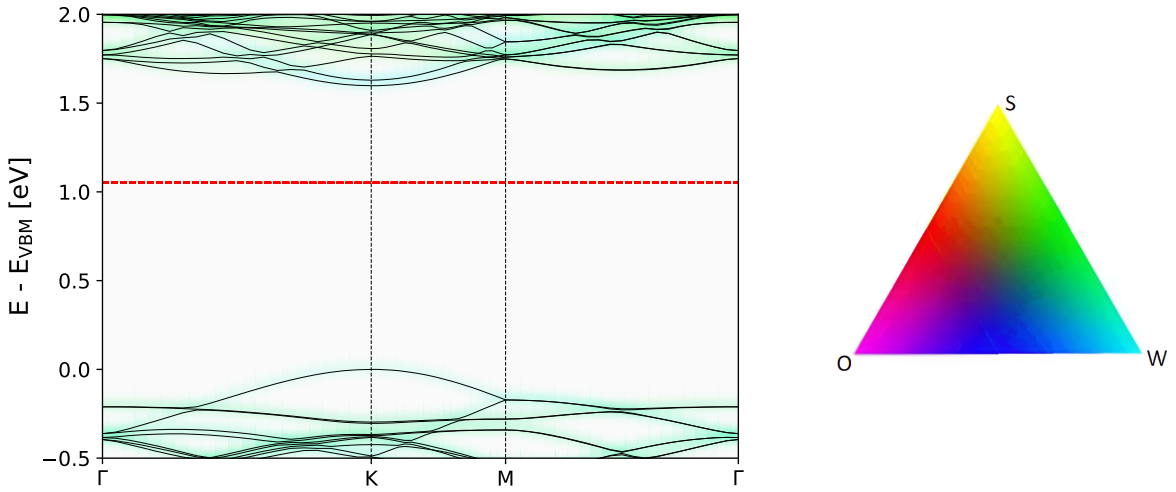

Figure 4.10: K-resolved PDOS of the 5×5 WS_2 supercell with O_S (the Fermi level is depicted with a red dashed line).

Comparing the k-PDOS of O_S in Figure 4.10 and the k-PDOS of V_S in Figure 4.6, there are no modifications outside the gap region. For example, the predominance of W contribution in the top of the valence band and in the bottom of the conduction band in K is preserved also in presence of O_S. No states are characterized by a reddish shade associated to O contribution. The previously identified band below the valence band maximum does not show any relevant O contribution. Hence, it is possible to conclude that this band is not a defect state due to O within the valence band, but it is probably a band that it is already present in the pristine case and the broken symmetry between top and bottom S planes, due to O presence, removes the energy degeneracy that previously characterizes these states.

4.5 Chromium as substituent of tungsten

Chromium substituent is considered the most common unintentional defect in the W site in WS_2 monolayers. Similarly to the chalcogen defect analysis, the structural properties of supercells with Cr_W are analysed. Figure 4.11 shows the relaxed structure of the 3×3 supercell with Cr_W. Cr atom is completely aligned to other W atoms. The main modification is associated to the distance of S atoms in the same plane, in proximity of Cr site. Indeed, as shown in Table 4.7, the S - S in-plane distance decreases of about 4 % due to the smaller atomic radius of Cr with respect to W. These results are in agreement with experimental evidences, as discussed in section 1.2.2.2.

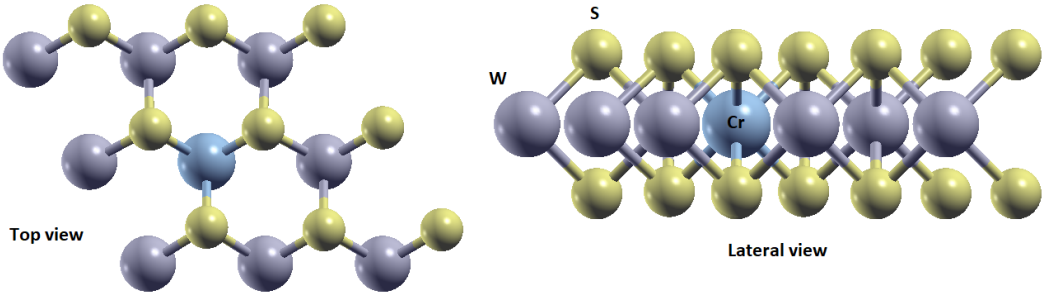

Figure 4.11: Relaxed 3×3 supercell with Cr_W.

Supercell	3×3	4×4	5×5	6×6	Pristine
S - S distance [Å]	3.049	3.045	3.043	3.041	3.179

Table 4.7: Comparison of S - S in-plane distance in proximity of Cr_W in different WS_2 supercells.

The electronic properties associated to Cr_W defect are then evaluated by analysing the band diagram of supercells at progressively increasing dimension. Figure 4.12 shows the results of supercells from 3×3 up to 6×6. Notice that the K point in the UCBZ is folded on the Γ point in the BZ of the 3×3 and 6×6 supercell, as discussed in section 4.3.

The main electronic feature of Cr_W is the presence of in-gap states, just below the conduction band minimum. In total there are 6 defect bands, as visible in Figure 4.12a. However, their energy separation progressively decreases in larger supercells and there are only 3 non degenerate states in the 6×6 supercell. Notice that the dispersion of these states is already reduced in the 5×5 supercell, but the band gap estimation is not accurate. Indeed, as shown in Table 4.8, the gap in the 5×5 supercell is larger than the nominal one and, above all, system has an indirect gap. Indeed, the bottom of the conduction band is associated to a point in the path between Γ and K. For that reason,

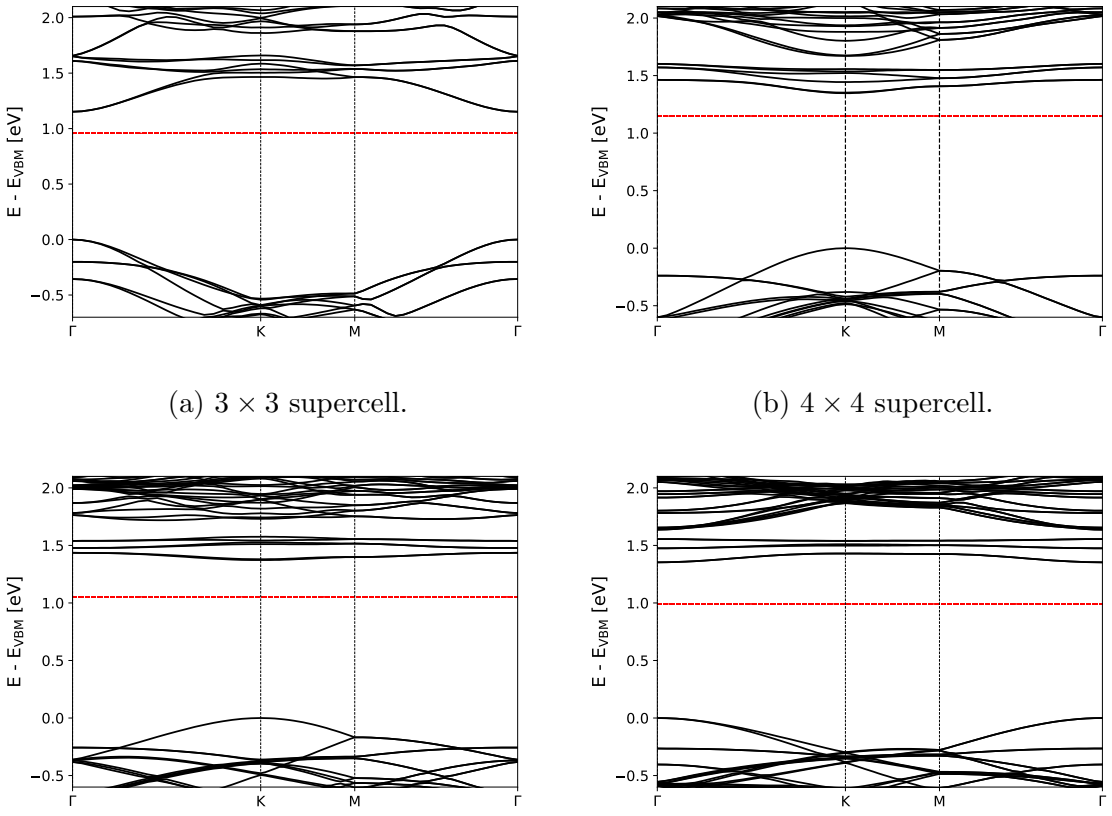

(a) 3×3 supercell.

(b) 4×4 supercell.

(c) 5×5 supercell.

(d) 6×6 supercell.

Figure 4.12: Band diagrams of different WS_2 supercells with Cr_W (the Fermi level is depicted with a red dashed line).

the 6×6 supercell is considered and the direct gap value is more correctly estimated in this supercell, as shown in Table 4.8. Hence, the next analysis of Cr_W is performed in the 6×6 supercell. The same band evaluation is also performed employing a cutoff energy higher than 55 Ry. Indeed, the analysis of the Cr bulk system reveals that Cr pseudopotential requires a cutoff energy equal to 80 Ry. Nevertheless, the band diagram at 80 Ry is almost unchanged with respect to the 55 Ry analysis, as shown in Table 4.8.

Figure 4.13a shows the band diagram and the PDOS of the 6×6 supercell with the Cr_W defect. For comparison, the analysis of the pristine supercell with the same size is also reported in 4.13b.

The comparison in Figure 4.13 allows for a better identification of three defect states. They are unoccupied and very close to the bottom of the conduction band. Indeed, the separation between the highest defect state and the minimum of the conduction band is only about 80 meV. The presence of these defect states is also confirmed experimentally, as discussed in section 1.2.2.2 and shown in Figure 1.6. However,

Supercell	3×3	4×4	5×5	5×5	6×6	Pristine
Cutoff energy [Ry]	55	55	55	**80**	55	55
E_g [eV]	1.66	1.67	1.72	1.72	1.63	1.61
Gap type	direct	direct	indirect	indirect	direct	direct

Table 4.8: Comparison of the band gap value in different WS_2 supercells with Cr_W and at different cutoff energies.

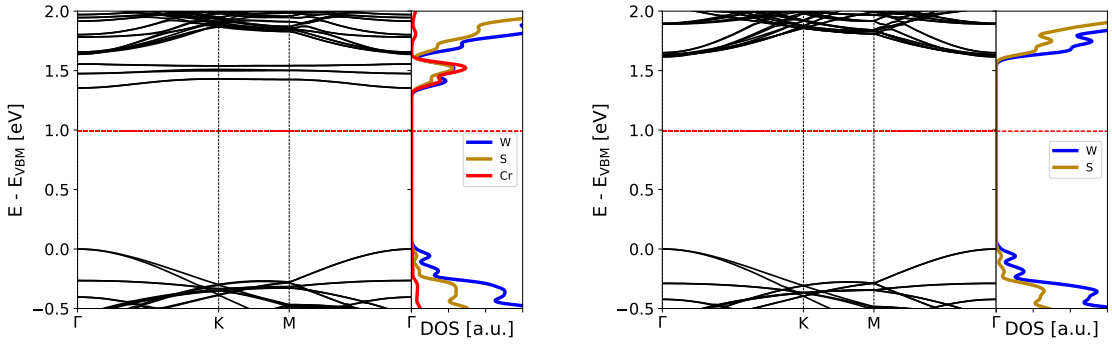

(a) Cr substituent.

(b) Pristine.

Figure 4.13: Band diagrams and PDOS of the 6×6 WS_2 supercell (the Fermi level is depicted with a red dashed line).

the experimental estimation of the separation between defect states and the minimum of the conduction band is larger (220 meV [15] vs 80 meV). This mismatch can be associated to the limit of the PBE functional in the gap estimation. Nevertheless, the internal separation between defect states is effectively estimated: the separation between the first and the second state and the separation between the second and the third are about 95 meV and 70 meV respectively in the simulated band diagram. As shown in Figure 1.6, the same separations are 100 meV and 80 meV according to STS measurements. Considering that Cr_W defect states are close to the conduction band, but are unoccupied, they are not donor levels. Indeed, Cr_W is an isoelectronic substitution and does not provide any additional electrons/holes.

Beside the in-gap defect states, Cr_W does not strongly alter the band diagram of the pristine material. Indeed, the PDOS contribution of Cr species in Figure 4.13a is almost negligible in the conduction and the valence band. Cr has the major role in the defect states, however W and S contributions are also present in the in-gap states. This proves that a hybridization between Cr and W/S orbitals occurs in this type of defect.

The contribution of the different chemical species is further investigated by analysing the k-resolved PDOS reported in Figure 4.14. The relative contribution of the different

atomic species is codified in the color shades: predominance of W, S and Cr contribution is associated to cyan, yellow and magenta respectively, as shown in the color triangle in Figure 4.14.

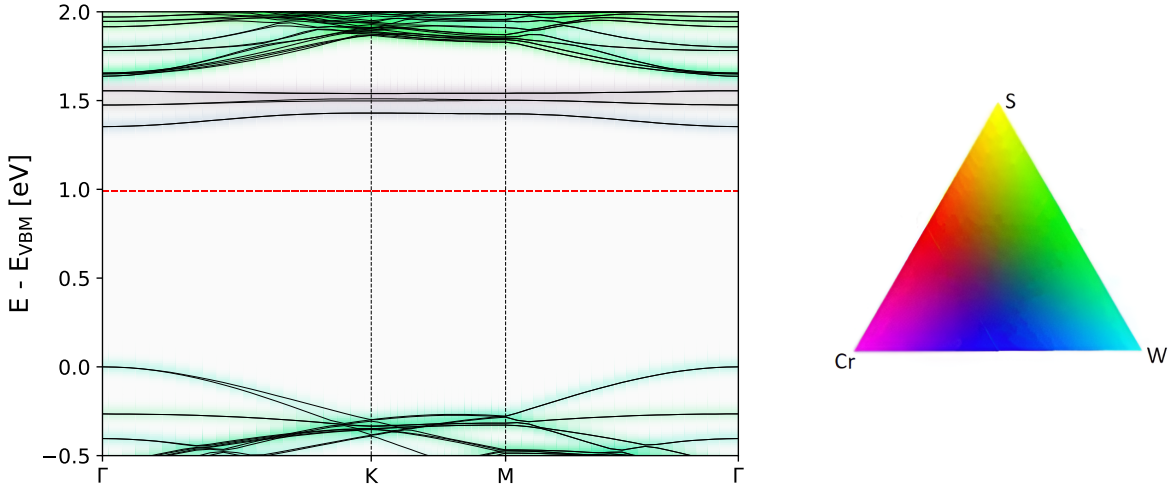

Figure 4.14: K-resolved PDOS of the 6×6 WS_2 supercell with Cr_W (the Fermi level is depicted with a red dashed line).

The predominance of cyan or green in the valence and conduction band shows W and S, but no Cr contribution. On the other hand, the predominance of the reddish color in the defect states, above all in the second and in the third, further confirms the predominant contribution of Cr in the in-gap states.

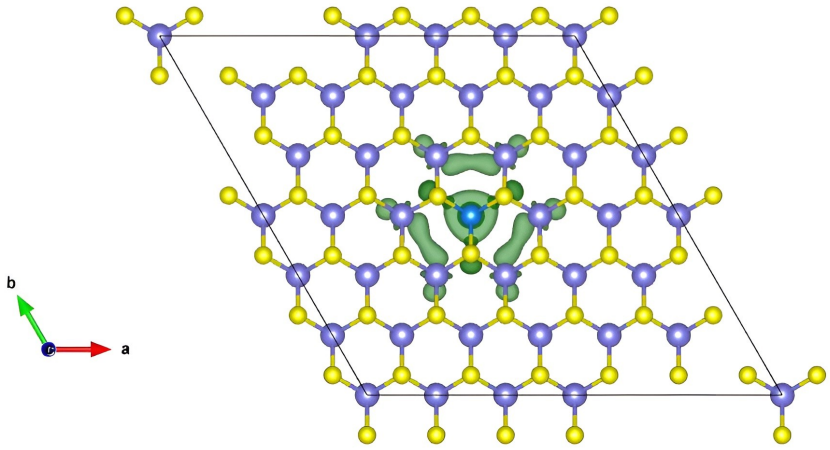

Figure 4.15: Charge density isosurface associated to the 1st defect state due to Cr_W in WS_2 monolayer (isosurface value = 0.001 a.u.). Purple, yellow and light blue balls are respectively W, S and Cr atoms.

Finally, the spatial localization of defect states is studied. Figure 4.15 shows the charge density isosurface associated to the first in-gap states. Other in-gap state isosurfaces are not reported since they show similar features. The three-fold pattern centered around the Cr atom clearly shows the spatial localization of the defect state around the substituent atom.

In summary, the structural and electronic properties of the most common unintentional point defects (i.e., V_S, O_S and Cr_W) in WS_2 monolayers are investigated in this chapter. The analysis of the formation energies in section 4.2 confirms the experimental evidences that the analysed defects can be unintentionally introduced during the synthesis: O_S and Cr_W are generated during the CVD growth, while unpassivated S vacancies are more commonly created in post-growth treatments due to the higher formation energy. The in-gap defect states associated to V_S are not responsible for the unintentional n-doping of WS_2 monolayers, but they might mediate non-radiative recombination processes. The presence of O atoms instead of S does not alter the pristine band diagram and O incorporation can be adopted as strategy to passivate S vacancies. Finally, the Cr_W defect is responsible for three in-gap states in proximity of the conduction band minimum, but differently from other transition metal substituents, Cr is not an effective dopant atom for WS_2.

CHAPTER 5

Molecule adsorption on selected WS_2 point defects

This chapter aims at the analysis of gas molecule adsorption on WS_2 monolayers. Adsorption can occur both on the edges [103] and on the basal plane [36] of the flakes. Specifically, this work considers the adsorption on point defects in the basal plane. Indeed, defects might behave as highly reactive sites, above all in CVD samples where they are more abundant. Only common unintentional defects discussed in chapter 4 (i.e., V_S, O_S and Cr_W) are included in this analysis. Common gas molecules, such as O_2, H_2O and NH_3, are considered in view of the spontaneous exposure of the flakes to these chemical species during sample synthesis, handling, storage and characterization. Both physisorption and chemisorption processes are investigated. The first is characterized by the absence of new chemical bonds between the molecule and the surface atoms. Hence, the weak electrostatic interactions result in quite small adsorption energies (usually tens or few hundreds of meV) and the molecule geometry is minimally destabilized due to the large separation between the molecule and the surface. Whereas, the chemisorption process is characterized by the formation of chemical bonds between the molecule and the flake, resulting in adsorption energies of few eV. The new bonds perturb the molecule stability, distorting its original geometry.
For each type of defect, different molecule configurations are considered to identify the minimum energy adsorption geometry. Indeed, a gas can interact with the flakes in a geometry in which the molecule is vertical, horizontal, tilted etc with respect to the monolayer. Moreover, molecules can be adsorbed exactly on top of the missing / substituent atom or on other sites surrounding the defect. To consider this variability, molecules are initially located at different distances and orientations with respect to the monolayer and a relaxation process is performed to identify the stable configuration geometries. This initial set of tests on a wide range of cases is performed in the 3×3 supercell. Even if this supercell is not suitable for the correct analysis of the defects, as discussed in chapter 4, analysed molecules are quite small and the interaction

among the periodic replicas is small for a preliminary analysis. This choice allows for a computational time reduction and a wider range of configurations can be initially considered. For each optimised adsorption geometry, the adsorption energy E_{ads} is evaluated through equation 5.1:

$$E_{\text{ads}} = E_{\text{WS}_2\,+\,\text{mol}} - E_{\text{WS}_2} - E_{\text{mol}}, \tag{5.1}$$

where:

- $E_{\text{WS}_2\,+\,\text{mol}}$ is the total energy of the supercell with the adsorbed molecule,
- E_{WS_2} is the total energy of the supercell without the adsorbed molecule,
- E_{mol} is the total energy of the isolated molecule.

According to the definition in equation 5.1, negative adsorption energies are associated to energetically favorable adsorption configurations. Once the most stable configurations are identified, they are extensively studied to clear out the variations in the band diagram once the molecule is adsorbed. This detailed analysis is performed in a larger supercell to properly describe isolated defects, as discussed in chapter 4.

5.1 Water and ammonia molecule adsorption

The influence of water vapour on WS_2 monolayers is analysed by simulating the adsorption of H_2O on the discussed defects. Despite the presence of dangling bonds in the V_S case, the H_2O molecule does not chemisorb on the vacancy, but is only physisorbed. Physisorption is also possible on the O_S and Cr_W site. Despite the stability of these configurations, as confirmed by adsorption energies in the range -150 meV ÷ -300 meV, the adsorption of these molecules does not significantly alter the band diagram. Similar condition occurs for NH_3: physisorption prevails with adsorption energies in the range -150 meV ÷ -250 meV, according to the defect type. However, no in-gap states or variations of the band gap value occur when NH_3 is adsorbed.

For that reason, H_2O and NH_3 molecule adsorption on the defects of the basal plane has a minimal influence on the electronic properties of WS_2 and an extended analysis for these adsorption conditions is not reported. Nevertheless, these molecules can modify the material properties when they are adsorbed at the flake edges or grain boundaries [103].

5.2 Molecular oxygen adsorption

Molecular oxygen is one of the most probable gas species to which WS_2 flakes are exposed. Here, only isolated O_2 molecule adsorption is considered; nevertheless this

process can become the starting point of a full oxidation mechanism in which large areas of flakes are converted from WS_2 to WO_x and the peculiar material properties drastically change [104]. Even if O_2 adsorption is possible also in proximity of O_S (section 5.2.2) and Cr_W (section 5.2.3), the V_S case is more extensively studied due the co-presence of physisorption (section 5.2.1.1) and chemisorption (section 5.2.1.2) processes. The potential energy barrier between these two adsorption conditions is also simulated to evaluate the transition effectiveness (section 5.2.1.3).

5.2.1 O_2 adsorption on sulphur vacancy

5.2.1.1 O_2 physisorption on V_S

O_2 physisorption on V_S is obtained by initially locating the molecule at a distance larger than 4 Å from the W plane and allowing the molecule to relax into a minimum energy configuration. Two relevant adsorption conditions in proximity of the V_S site are identified. The geometry configurations are reported in Figure 5.1 and 5.2: for the sake of clarity, in order to better visualize the relative separation of the molecule and of the defect, the process is represented in a small supercell even if analysis is performed in the 5×5 supercell.

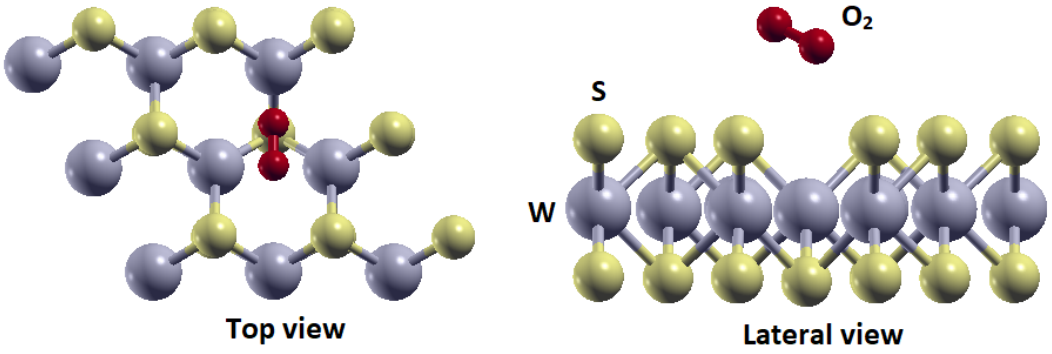

Figure 5.1: Horizontal O_2 physisorption on V_S.

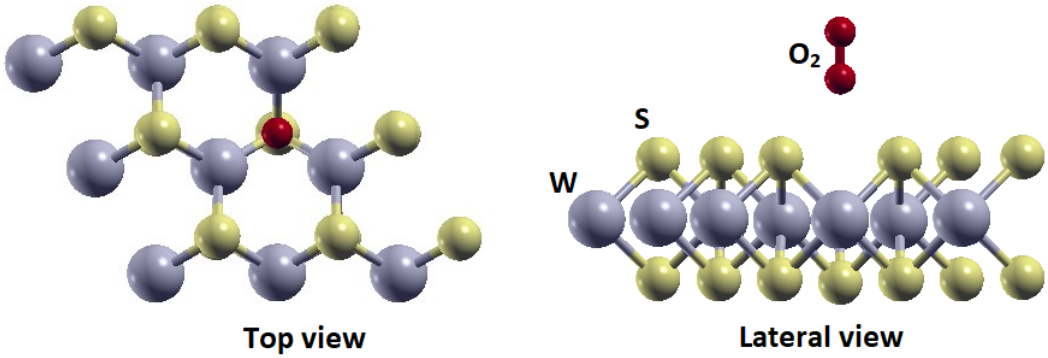

Figure 5.2: Vertical O_2 physisorption on V_S.

In the first case, reported in Figure 5.1 and labelled as 'horizontal configuration', the molecule is horizontal with respect to the monolayer, over the V_S site and aligned with a W-S bond. Notice that the molecule is not perfectly parallel to the monolayer, but is slightly tilted out of plane. In the second physisorption configuration, labelled as 'vertical' and shown in Figure 5.2, the molecule is perpendicular to the monolayer and centered over the empty S site. Despite the dangling bonds associated to the missing S atom, no new chemical bonds are created and the distance of the geometrical centre of the molecule with respect to the W plane is quite large (4.08 Å and 4.23 Å in the horizontal and in the vertical configuration respectively). Moreover, the O_2 bond length is unchanged with respect to the isolated molecule case (i.e., 1.212 Å), further confirming the weak interaction between the flake and O_2. This interaction strength is quantified by evaluating the adsorption energy at a cutoff energy equal to 75 Ry, as reported in Table 5.1. It is evident that the supercell size minimally alters the interaction evaluation (variations within 10 meV), confirming the effectiveness of the preliminary analysis in the 3×3 supercell for the identification of the most stable configuration among the considered ones. The small adsorption energies are compatible with a physisorption process. The horizontal configuration is more favorable due to the closeness of the O atoms to the flake surface, even if the difference between the two cases is small. Notice that the adsorption energy of O_2 on the surface without defects (E_{ads} = -110 meV [105]) is similar, hence V_S does not strongly enhance the O_2 interaction when only physisorption occurs.

Adsorption energy [meV]		
V_S supercell	3×3	5×5
Horizontal physisorption	-140	-130
Vertical physisorption	-120	-120

Table 5.1: Adsorption energy for O_2 physisorption on V_S in WS_2 monolayer.

The electronic properties of the physisorption configurations are evaluated by analysing the band diagram of the 5×5 supercell with the adsorbed molecule, as shown in Figure 5.3.

The conduction and the valence bands are unchanged after the O_2 adsorption and the gap value is also the same (i.e., 1.64 eV). The pairs of defect states (i.e., the electronic signature of V_S) are still present after the O_2 adsorption, proving that dangling bonds are not saturated. The sole effect of the physisorption is the introduction of a discrete level, associated to the O_2 molecular levels, just below the defect states. In both cases, the states introduced by O_2 are unoccupied and far away from the valence band maximum (about 0.94 eV and 0.91 eV in the horizontal and in the vertical configuration respectively). At the same time, the O_2 level is quite close to the lowest V_S defect state: the separation is about 160 meV and 190 meV in the horizontal and in the vertical

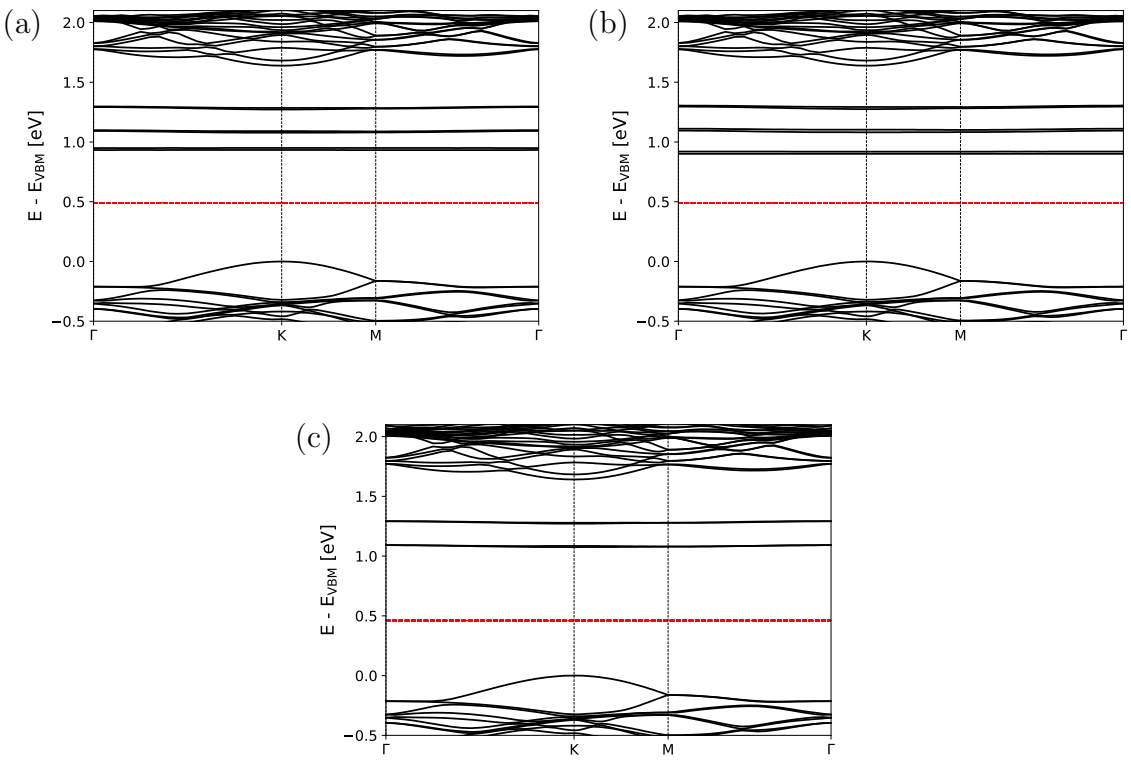

Figure 5.3: Band structure of O_2 physisorbed on a vacancy site in a horizontal (a) and vertical (b) configuration. The band structure of WS_2 ML with a vacancy is reported as reference (c). The Fermi level is depicted with a red dashed line.

configuration respectively. Notice that O_2 physisorption on the pristine material is responsible for the introduction of a similar unoccupied level in the middle of the gap [105]. Nevertheless, not only the O_2 level, but also the V_S defect states may be involved in the energy transitions between the valence and the conduction band, increasing the complexity of the process.

5.2.1.2 O_2 chemisorption on V_S

The presence of dangling bonds due to the missing S atom allows also for the chemisorption of O_2. Indeed, if the molecule is initially close to the monolayer surface (i.e. at a distance smaller than 3 Å from the W plane), it is attracted towards the V_S site and relaxes in a chemisorbed configuration. The analysis in the 5×5 supercell at a cutoff energy equal to 75 Ry allows for the identification of two different chemisorption cases. A configuration in which the molecule is horizontal with respect to the flake is detected, as shown in Figure 5.4. It is not perfectly parallel to the W plane, but an O atom is up-shifted due to the presence of a underlying W atom. The molecule is aligned with a W-S bond. A second chemisorption configuration is also identified,

as shown in Figure 5.5. In this case the molecule is vertical with respect to the flake and perfectly centered in the V_S site. The bottom O atom of the molecule establishes chemical bonds with W.

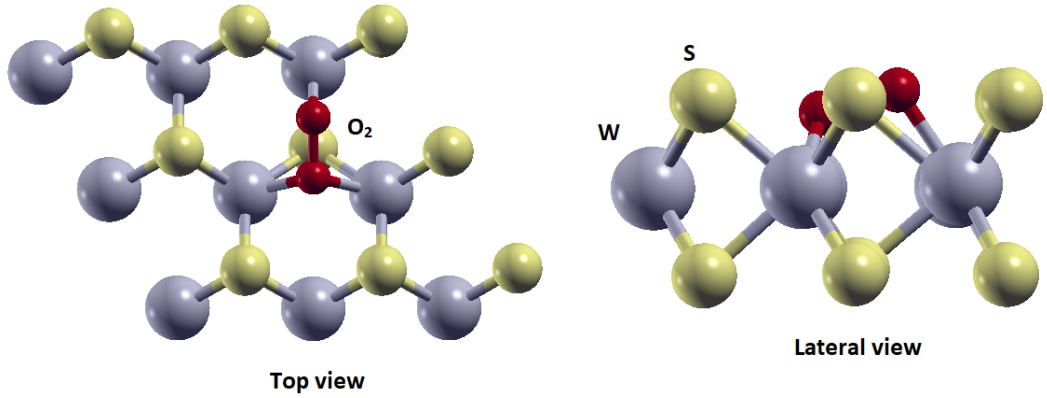

Figure 5.4: Horizontal O_2 chemisorption on V_S.

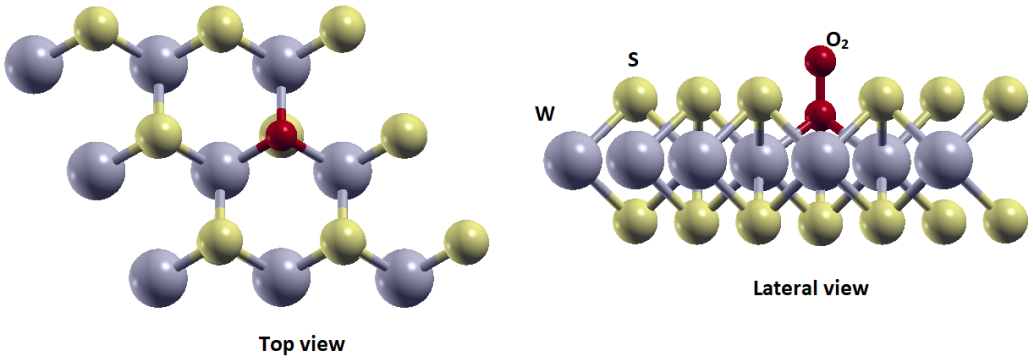

Figure 5.5: Vertical O_2 chemisorption on V_S.

The formation of chemical bonds between W and O atoms characterizes the analysed configurations. As reported in Table 5.2, in the horizontal case, the distance between the O atom and the nearest W atom is 2.103 Å and 2.043 Å for the down-shifted and the up-shifted O atom respectively. On the other hand, in the vertical configuration, the W-O distance is 2.168 Å. Notice that the W-O length in the analysed chemisorption configurations is slightly different from the bond length in case of O substituent (i.e., 2.076 Å), as analysed in paragraph 4.4. Nevertheless, the W-O distances are always compatible with the formation of chemical bonds. The interaction between the flake and O_2 perturbs the molecule geometry. Indeed, the original O-O distance in the isolated molecule, equal to 1.212 Å, largely increases when the molecule occupies the V_S site (increase of 20 % and 15 % in the horizontal and in the vertical configuration respectively).

The interaction strength of chemisorbed molecules is analysed in Table 5.3. The supercell size minimally changes the adsorption energy, as already observed for the

Configuration	Horizontal	Vertical
W-O distance [Å]	2.103 / 2.043	2.168
O-O distance [Å]	1.454	1.397

Table 5.2: Geometry of O_2 chemisorbed on V_S in WS_2 monolayer.

physisorption case. The large adsorption energies confirm the chemical nature of the interaction and its room temperature stability. Specifically, the horizontal configuration is more stable than the vertical one. The larger stability of the first configuration can be qualitatively justified by analysing the geometry: both O atoms are chemically interacting with W in the horizontal case, while a single O atom is involved in chemical W-O bonds in the vertical one. The different interaction strength is also confirmed by the variations of the O-O bond length reported in Table 5.2: the O_2 system is less interacting with the monolayer in the vertical configuration and, indeed, the O-O bond is less stretched and more similar to the isolated case with respect to the horizontal chemisorption. However, despite the different adsorption energies, both configurations are by far stable and can commonly occur.

Adsorption energy [eV]		
V_S supercell	3×3	5×5
Horizontal chemisorption	-1.98	-1.96
Vertical chemisorption	-1.66	-1.63

Table 5.3: Adsorption energy for O_2 chemisorption on V_S in WS_2 monolayer.

The electronic properties of the O_2 chemisorbed configurations are then analysed by evaluating the band diagram in the 5×5 supercell, as shown in Figure 5.6.
The common feature of the band diagrams when O_2 is chemisorbed is the passivation of the defect states that characterise the gap region in case of V_S. This effect is compatible with the passivation of the W dangling bonds previously discussed. Moreover, the same effect is also observed in case of O substituent, as discussed in section 4.4. Nevertheless, the co-presence of two O atoms reciprocally interacting has other impacts in the band diagram. The horizontal configuration is characterized by the absence of any in-gap states, but states with limited dispersion can be identified within the valence band. A more detailed description is possible by analysing the k-resolved PDOS, considering all the chemical species and O alone, as reported in Figure 5.7 and 5.8, respectively.
If all chemical species are considered in the plot of the k-PDOS, the O contribution cannot be distinguished. However, if the k-PDOS of O alone is analysed, a group of bands become evident below the maximum of the valence band. Comparing Figure 5.7 and 5.8 for the horizontal configuration, it is possible to deduce that both W and O

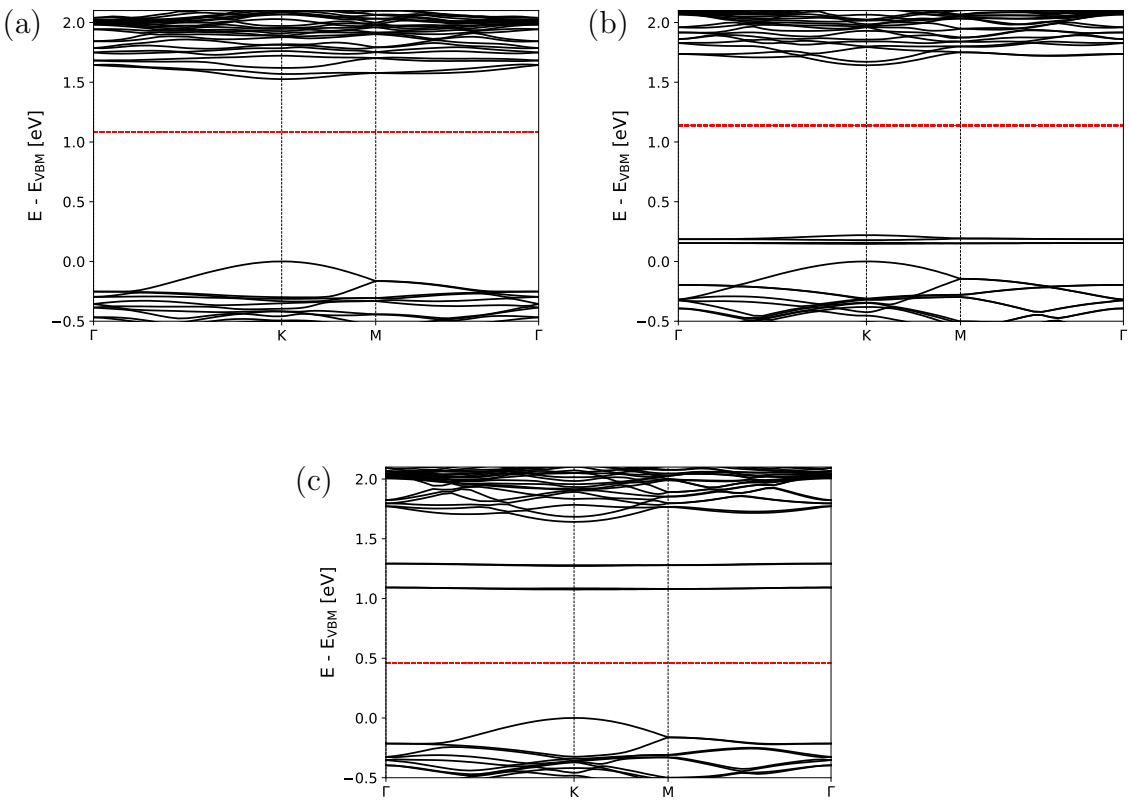

Figure 5.6: Band structure of O_2 chemisorbed on a vacancy site in a horizontal (a) and vertical (b) configuration. The band structure of WS_2 ML with a vacancy is reported as reference (c). The Fermi level is depicted with a red dashed line.

species have a contribution in the identified bands. O and W orbitals are hybridized in these states, confirming the strong interaction between the molecule and the flake. However, these states are well within the valence band, so they do not have an evident role in the modification of the electronic properties of the system.

The identification of the O_2 role is more intuitive in the vertical configuration. Indeed, as visible in Figure 5.6, isolated bands appear well within the band gap, at about $0.15 \div 0.19$ eV above the valence band maximum. As in the previous chemisorption case, these states are occupied. The higher energy of the bands associated to O atoms in the vertical configuration with respect to the horizontal one (where O contribution is within the valence band) is compatible with the smaller stability of the vertical case. The minor interaction strength between the molecule and the monolayer in the vertical configuration can be also deduced by analysing the total k-PDOS in Figure 5.7. In-gap states are mainly due to the O species, as proven by the predominance of the magenta shade. Hence, W and S contribution is minor, so the hybridization between the O and

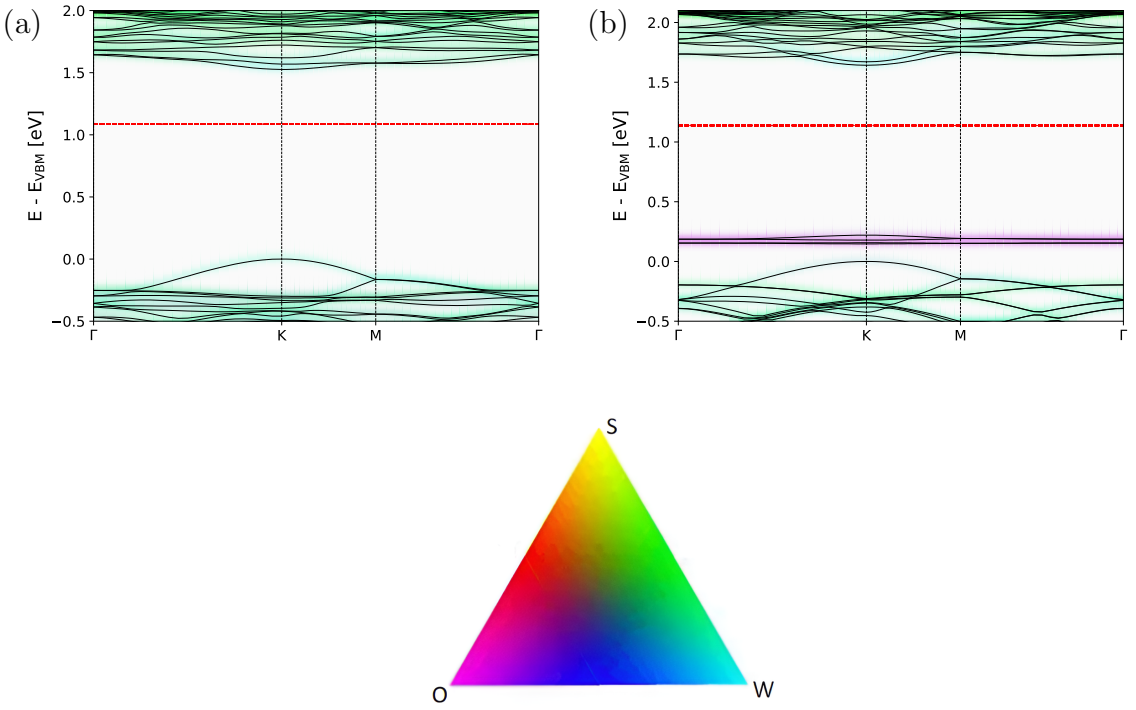

Figure 5.7: K-resolved PDOS of O_2 chemisorbed on a vacancy site in a horizontal (a) and vertical (b) configuration (the Fermi level is depicted with a red dashed line).

the other species orbitals is poorer and in-gap isolated states resemble the condition of physisorption in section 5.2.1.1.

Beside the discussed modifications, a more careful comparison in Figure 5.6 reveals that adsorption also modifies the conduction band. This change is further evident when the variations of the gap are evaluated, as reported in Table 5.4. The band gap decreases, above all in the horizontal configuration (decrease of about 0.11 eV) with respect to the condition without O_2.

Configuration	O_2 horizontal	O_2 vertical	No O_2
Band gap [eV]	1.53	1.64	1.64

Table 5.4: Band gap in case of O_2 chemisorption on V_S in WS_2 monolayer

The gap decrease in the horizontal configuration is associated to the presence of an additional band below the original minimum of the conduction band, as visible in Figure 5.6. The origin of this band is further investigated with the k-resolved PDOS. In Figure 5.8 for the horizontal configuration, it is easy to clearly distinguish the additional band below the conduction band minimum due to the reddish shade associated to the O species.

In the vertical configuration there are no states that alter the minimum of the conduction band. Indeed, the gap is unchanged with respect to the case without O_2, as shown in Table 5.4. The same result is confirmed in the analysis of the k-PDOS for the O species alone, reported in Figure 5.8. Beside the contribution to in-gap states, there are no states with evident O contribution in proximity of the minimum of the conduction band, proving that the vertical configuration minimally alters the picture of the bottom of the conduction band.

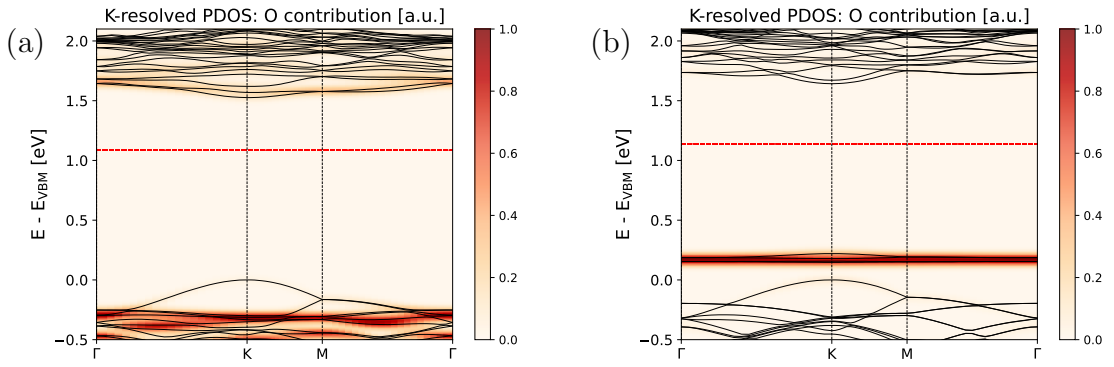

Figure 5.8: K-resolved PDOS of O species alone for O_2 chemisorbed on a vacancy site in a horizontal (a) and vertical (b) configuration (the Fermi level is depicted with a red dashed line).

5.2.1.3 O_2 adsorption energy barriers

Paragraphs 5.2.1.1 and 5.2.1.2 show that the O_2 molecule can be both physisorbed or chemisorbed on V_S. Both physisorption and chemisorption can occur in two configurations in which the molecule is horizontal or vertical with respect to the flake surface. Considering that system properties markedly change in physisorption and in chemisorption, it is important to evaluate the energy barriers between two configurations to identify at which conditions the transition is possible. The evolution of the O_2 position and the energy variations during the transition between the initial and the final state are evaluated through the Nudged Elastic Band (NEB) method, whose theory is briefly introduced in section 2.6. The NEB path is evaluated starting from the optimized initial (physisorption) and final (chemisorption) geometries and simulating 5 intermediate images. Once the position of the potential barrier peak is identified, further NEB intermediate images are evaluated in this region to get a more precise estimation of the barrier height.

Firstly, the transition between the horizontal physisorption and the horizontal chemisorption configuration is analysed. The evolution of the molecule position is reported in Figure 5.9. Along the NEB path, the molecule shifts down towards the W

plane from the initial distance of about 4 Å. Since the molecule is not perfectly parallel to the flake plane, the translation is coupled with a partial rotation of the molecule.

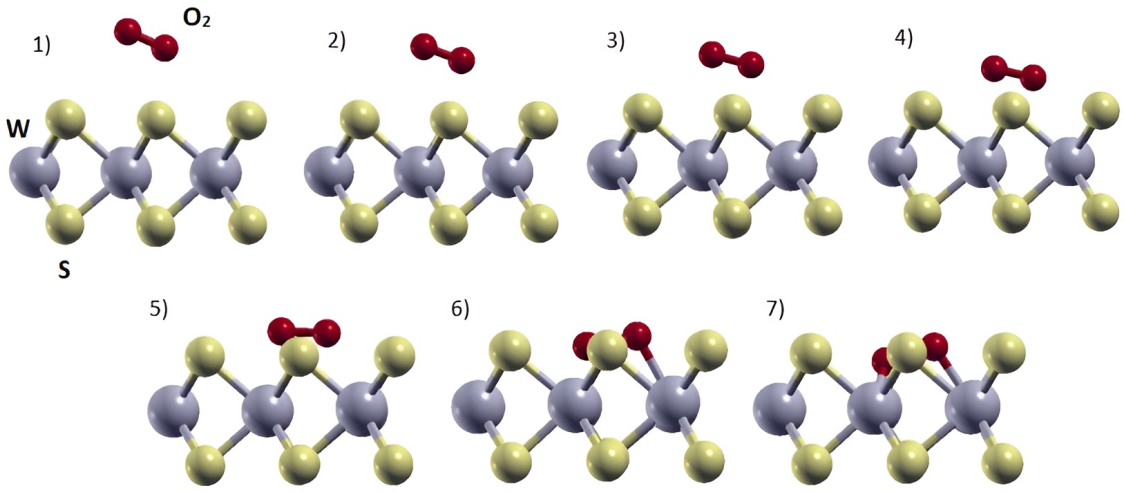

Figure 5.9: O_2 geometry evolution between horizontal physisorption (1) and horizontal chemisorption (7) state on the V_S site.

Figure 5.10 shows the variation of the energy during the described transition. The energy E_O of the isolated molecule is set to zero as energy reference. The large energy difference between the initial and the final states prevents desorption from the chemisorbed state. On the other hand, the energy barrier separating the physisorption from the chemisorption condition is about 0.93 eV, as shown in Figure 5.10. Hence, O_2 can reach the chemisorption state if the flake is sufficiently heated.

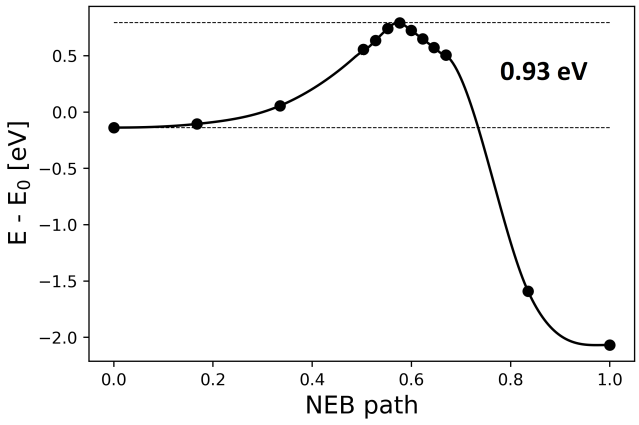

Figure 5.10: Energy profile during the transition from the horizontal physisorption to the horizontal chemisorption state on the V_S site.

The transition from the vertical physisorption to the vertical chemisorption configuration is then analysed. In this case, as reported in Figure 5.11a, the molecule simply translates towards the W plane and stretches during the NEB path without any rotation, since O_2 is always perfectly vertical and aligned with the V_S site. The energy profile reported in Figure 5.11b shows that the transition from physisorption to chemisorption is possible in case of heating, similarly to the previous discussed case. Indeed,, the potential barrier is 0.85 eV. Notice that the chemisorption state in the vertical case is less energetically favorable than the horizontal one, but the potential barrier for the vertical transition is slightly smaller. Hence, both horizontal and vertical chemisorptions can occur after an initial physisorbed step.

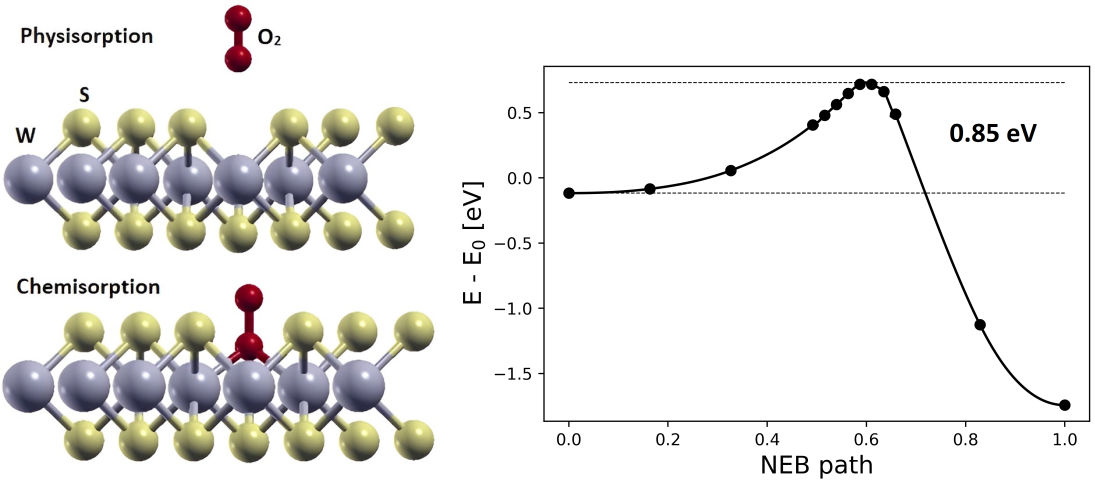

(a) O_2 geometry evolution.

(b) Energy profile.

Figure 5.11: Transition between vertical physisorption and vertical chemisorption state on the V_S site.

5.2.2 O_2 adsorption on oxygen substituent

Similarly to the adsorption on the V_S case, different orientations and adsorption sites in proximity of the O_S defect are considered in order to find the most stable configuration describing the O_2 - flake interaction. Independently of the initial distance of O_2 with respect to the flake surface, a chemisorption is never possible due to the absence of dangling bonds and the high stability of the TMD surface when completely passivated by O substituents. Different physisorption configurations sharing comparable stability and features are identified. However, only the most stable is carefully analysed as example for the other configurations. The O_2 molecule is parallel to the monolayer plane and is about 3.1 Å far from the substituent O atom. The large distance and the almost unchanged O-O bond length confirm the physisorption nature of the interaction. The weakness of the interaction is further established by evaluating the adsorption energy: it is about -130 meV in the 5×5 supercell and compatible with a physisorption

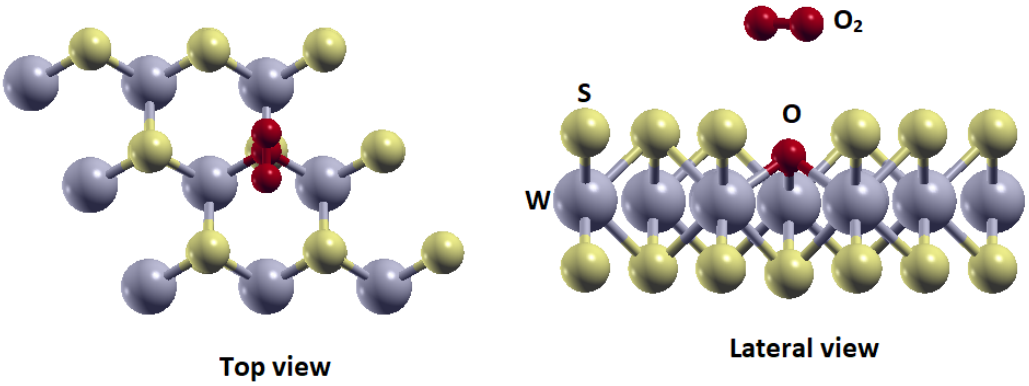

Figure 5.12: Most stable O_2 physisorption configuration on O_S.

process. Notice that this value is only slightly larger than the adsorption energies evaluated in the pristine flake (E_{ads} = -110 meV [105]). Moreover, the geometry and the interaction strength are also comparable to the horizontal physisorption on V_S. Hence, the O_S defect does not enhance the interaction with the O_2 molecule.

The electronic properties of O_2 adsorbed on O_S are then evaluated. The band diagram in case of adsorption, in the 5×5 supercell, is reported in Figure 5.13.

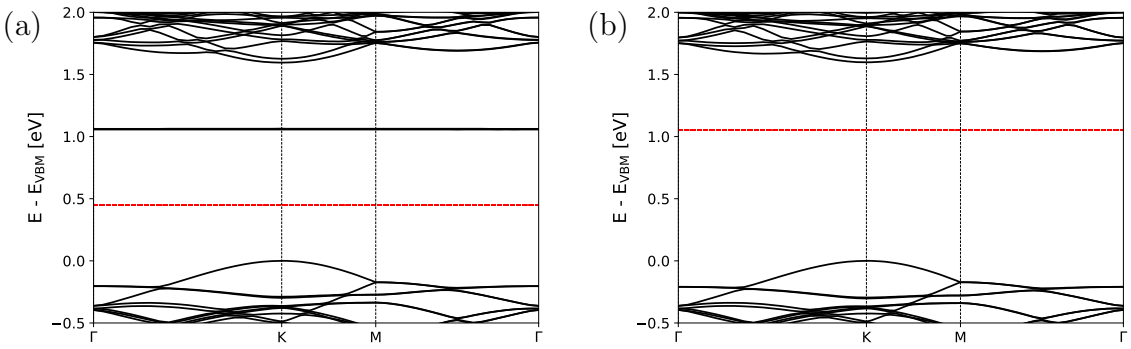

Figure 5.13: Band structure of O_2 adsorbed on an O_S site (a). The band structure of WS_2 ML with an O_S is reported as reference (b). The Fermi level is depicted with a red dashed line.

The main feature associated to the physisorption of O_2 on O_S is the introduction of a dispersionless state within the gap. All other relevant elements of the band diagram are completely unchanged with respect to the case without adsorbed molecule. The isolated state is unoccupied, but it is quite far from the maximum of the valence band (about 1.06 eV above it). Hence, this state results in a deep and ineffective acceptor level. However, it is an intermediate level that might mediate carrier transitions between conduction and valence band. Notice that the adsorption of O_2 molecule on the monolayer surface without defects is responsible for a similar modification of the

electronic properties [105]. Hence, also in this case the O_S defect minimally alters the behaviour of the material.

5.2.3 O_2 adsorption on chromium substituent

Finally, O_2 adsorption on chromium substituent is considered. Different adsorption configurations are also tested in this case. Physisorption is only possible and, in general, all considered adsorption geometries are characterized by similar interaction strengths. For that reason a unique configuration, the most stable, is analysed and is reported in Figure 5.14. The O_2 molecule is adsorbed over the Cr atom at about 4.8 Å from it. The molecule is aligned with the direction connecting two in-plane S atoms. Notice that the analysed adsorption geometry is very similar to the stable adsorption configuration of O_2 over a W atom in the pristine material [105]. Hence, from the adsorption standpoint, Cr and W atoms have a similar behaviour.

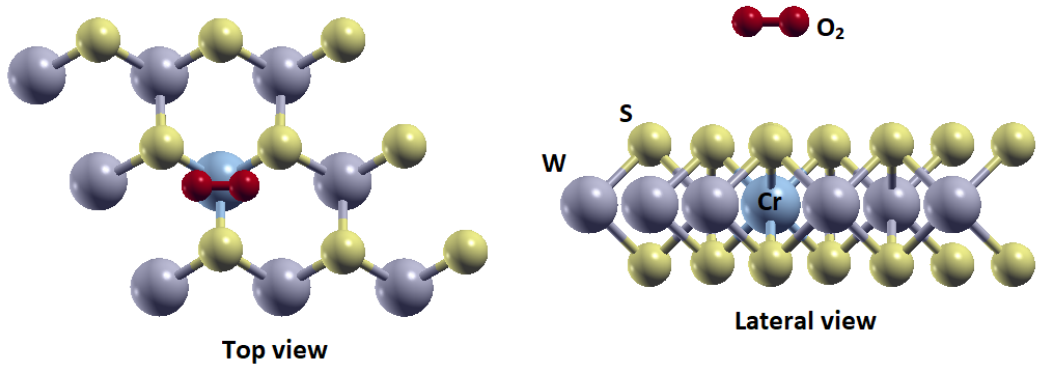

Figure 5.14: Most stable O_2 physisorption configuration on Cr_W.

The very large distance between O_2 and the flake surface is compatible with a weak interaction. Indeed, the adsorption energy evaluated in the 6×6 supercell is quite small (E_{ads} = -90 meV). Comparing the interaction strength for the analysed defects, it is evident that O_2 physisorption is more favoured on V_S (E_{ads} = -120 meV $\div$ -130 meV) and on O_S (E_{ads} = -130 meV) than on Cr_W.

Finally, the electronic properties of the system with the adsorbed O_2 molecule are analysed. The band diagram evaluated in the 6×6 supercell is reported in Figure 5.15, both with and without adsorbed O_2. Similarly to the case of O_2 on O_S, the adsorption does not alter the valence, the conduction band, the gap value and the position of the in-gap states associated to the defect. The only new feature associated to O_2 is the presence of a discrete level in the gap, close to the Cr defect states. The O_2 level is about 1.01 eV above the valence band maximum and about 0.34 eV below the lowest Cr defect states. The position of the O_2 level in the Cr_W supercell is very similar to the O_S case. In both situations, O_2 states are unoccupied and sufficiently far from the valence band maximum to behave as a deep ineffective acceptor level. However, in

the Cr_W case the energy transitions not only involve the O_2 level, but also the defect states. Notice, differently from the V_S case where defect states can be passivated by O_2, here the adsorption process does not alter the defect states.

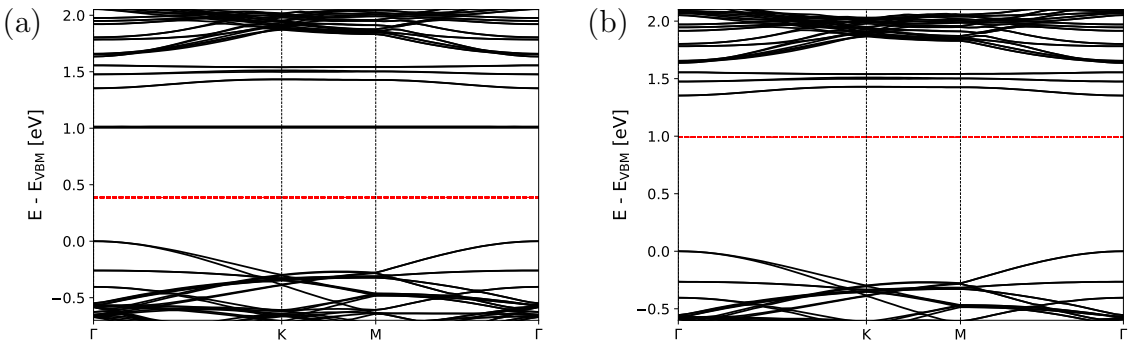

Figure 5.15: Band structure of O_2 adsorbed on a Cr_W site (a). The band structure of WS_2 ML with a Cr_W is reported as reference (b). The Fermi level is depicted with a red dashed line.

5.3 Summary of adsorption processes on defective monolayers

In conclusion, the adsorption of different gases (i.e., O_2, H_2O and NH_3) on common unintentional point defects (i.e., V_S, O_S and Cr_W) in WS_2 monolayers has been analysed in this chapter. The stability towards gas adsorption of the surface of perfect TMDs is a peculiarity of 2D materials and the absence of defects allows only for weak physisorption processes [36]. However, defects might modify the reactivity of the flake surface. In some cases the adsorption process is minimally altered with respect to the pristine monolayer despite the presence of defects such as O_S and Cr_W. On the other hand, for some defects, such as V_S, the interaction between the flake and the molecule is strong. However, the presence of dangling bonds in the V_S site does not directly imply that the molecule is chemisorbed. Indeed, H_2O and NH_3 can be only physisorbed over the V_S site.

Among the considered molecules, water and ammonia adsorption minimally alters the band diagram of the defective monolayer, so these conditions are not extensively studied, but the analysis focuses on the O_2 case. The O_2 molecule can be both physisorbed and chemisorbed on the V_S site. Different physisorption configurations are identified, but they show similar features: the adsorption does not passivate the defect states associated to the vacancy, but it only introduces a discrete unoccupied level in the middle of the gap, $0.91 \div 0.94$ eV above the valence band maximum, but $0.16 \div 0.19$ eV below the lowest defect state. In other words, the discrete O_2 level is simply superimposed to

the band diagram of the V_S cell. However, the chemisorption process of O_2 in the V_S site is also possible. Two stable chemisorption configurations are identified: the 'horizontal' and the 'vertical' adsorption condition. The latter is about 0.3 eV less stable and preserves some characteristics (minor O-O bond stretch, less evident hybridization between O and W, S orbitals) that resemble the physisorbed O_2 case. Nevertheless, both chemisorption configurations are stable and with large adsorption energies (-1.63 $\div$ -1.96 eV). The main effect of the O_2 chemisorption is the passivation of the V_S site. Hence, the O_2 chemisorption can have beneficial effects for the WS_2 properties: the suppression of the vacancy defect states removes possible non-radiative recombination channels, enhancing the photoluminescence of the material in a permanent way, due to the stability of the chemical bonds between O and W. However, this mechanism of passivation of sulphur vacancies requires the overcoming of a potential barrier between the physisorption and the chemisorption condition. The evaluated barriers are quite high, hence the passivation mechanism is not effective at room temperature. It requires an external heating treatment, for example an intentional thermal annealing or a local annealing due to the laser exposure during a PL analysis, above all if it is performed on a thermal insulating substrate as SiO_2. However, the chemisorption process has also some side effects on the band diagram. In the horizontal configuration, the band gap decreases of about 0.11 eV due to an additional band below the original conduction band minimum. In the vertical configuration, isolated and occupied states appear in the gap, 0.15 $\div$ 0.19 eV above the valence band maximum.

Finally, the adsorption of O_2 on the other defects analysed in this thesis work has minor modifications on the band diagram since only physisorption is possible. In case of O_S, the only effect is the introduction of an unoccupied level at 1.06 eV above the valence band maximum, similarly to the O_2 adsorption on the pristine surface without defects. Hence, the presence of O instead of S atom is not detrimental also from the standpoint of the adsorption process. The O_2 adsorption on the Cr_W site appears slightly less stable than the other defect cases, but it resembles the adsorption on the W atom in the pristine material. The unique effect of O_2 is the introduction of an unoccupied level 1.01 eV above the valence band maximum, but below the Cr_W defect states. Differently from the V_S case, these defect states are not passivated, hence the O_2 adsorption cannot be used to mitigate the impact of the Cr_W defect states.

Conclusions

In this thesis work the adsorption processes of common gas molecules on unintentional point defects in WS_2 monolayers are investigated. The analysis of the systems is performed by means of Density Functional Theory (DFT) simulations. Firstly, the pristine WS_2 monolayer is studied in a series of preliminary tests, aiming at determining the numerical accuracy of the simulation, but also the effects of explicitly considering the Spin-Orbit Coupling (SOC). This step was mandatory to validate the predictive capability of the simulation.
Then, the formation energies and the electronic properties of common point defects (V_S, O_S and Cr_W), unintentionally generated during the CVD synthesis or in the post-growth treatments, are analyzed. The S vacancy has the highest formation energy, while O_S is thermodynamically favorable. Hence, 'as-grown' samples are expected to present a low amount of V_S, being usually passivated by O atoms during the synthesis. The presence of residual vacancies has some negative consequences since they generate two couples of unoccupied in-gap defect states in the band diagram of WS_2. These can mediate non-radiative recombination mechanisms which may have detrimental effects when the material is used in optoelectronic devices. The passivation of V_S by the formation of O_S has beneficial consequences. Indeed, the analysis of the band diagram of the WS_2 monolayers containing O_S reveals that no in-gap states are present, restoring the original electronic picture of the pristine monolayer. Finally, the quite low formation energy of Cr_W is compatible with the temperatures of the synthesis process. The electronic signature of Cr_W is the presence of three pairs of unoccupied defect states close to the conduction band minimum.
The second part of this thesis focuses on the adsorption of selected gas molecules (O_2, H_2O, NH_3) on WS_2 monolayer with the point defects discussed above. Both in the case of the pristine surface and on the defected sites, physisorption is the most common process, even though for some defect cases (such as V_S) dangling bonds are present. Among the analyzed molecules, molecular oxygen has the major influence in the WS_2 band diagram. During physisorption, a pair of degenerate unoccupied levels appears in the middle of the gap. These states correspond to unperturbed O_2 molecular states which do not alter the electronic properties of WS_2. In all cases for which physisorption occurs, the pair of oxygen levels might mediate carrier transitions between bands, but these effects are reversible due to the weak molecule interaction and may

be eliminated via heating the sample. Among the adsorption processes studied in this thesis work, the only one in which O_2 interaction is markedly enhanced is associated to the chemisorption process on the V_S site. The main consequences of this interaction are the passivation of the V_S defect states and a local decrease of the band gap of the pristine WS_2. The first effect is beneficial since suppresses non-radiative channels, increasing photon emission probability. Notice that the passivation of the vacancy by O_2 chemisorption is not spontaneous, but it requires to overcome a potential barrier between physisorption and chemisorption condition.
In conclusion, this thesis proves that WS_2 monolayers, when are exposed to the environment, are mainly influenced by O_2. The V_S is the most reactive site, and when O_2 binds to a sulphur vacancy site, O incorporation has beneficial effects since it suppresses non radiative recombination processes. Further aspects, that need to be addressed in future investigations, are associated to the role of unintentional dopants in the WS_2 monolayer. This analysis must be performed by including in the simulation species like hydrogen impurities which are believed to originate n-type WS_2 monolayers. Moreover, the correlation between the electronic properties, here analyzed, and the optical properties could be further investigated, by employing post-DFT approaches, to correctly estimate the gap value and predict the optical absorption. This would allow interpreting and/or predicting the variations of WS_2 emission and photoluminescence spectra when exposed to different environments.

Bibliography

[1] K. S. Novoselov, A. K. Geim, S. V. Morozov, D. Jiang, Y. Zhang, S. V. Dubonos, I. V. Grigorieva, and A. A. Firsov. Electric field effect in atomically thin carbon films. *Science*, 306(5696):666–669, 2004. doi: 10.1126/science.1102896. URL https://www.science.org/doi/abs/10.1126/science.1102896.

[2] Zhong Lin, Bruno R Carvalho, Ethan Kahn, Ruitao Lv, Rahul Rao, Humberto Terrones, Marcos A Pimenta, and Mauricio Terrones. Defect engineering of two-dimensional transition metal dichalcogenides. *2D Materials*, 3(2):022002, apr 2016. doi: 10.1088/2053-1583/3/2/022002. URL https://doi.org/10.1088/2053-1583/3/2/022002.

[3] Agnieszka Kuc and Thomas Heine. On the stability and electronic structure of transition-metal dichalcogenide monolayer alloys mo1xxxs2ysey with x = w, nb. *Electronics*, 5:1, 12 2015. doi: 10.3390/electronics5010001. URL https://www.mdpi.com/2079-9292/5/1/1.

[4] M Palummo, A N D'Auria, J C Grossman, and G Cicero. Tailoring the optical properties of MoSsub2/sub and WSsub2/sub single layers via organic functionalization. *Journal of Physics: Condensed Matter*, 31(23):235701, mar 2019. doi: 10.1088/1361-648x/ab0c5e. URL https://doi.org/10.1088/1361-648x/ab0c5e.

[5] Y. Asadi and Z. Nourbakhsh. Structural, electronic, mechanical, thermodynamic, and linear and nonlinear optical properties of mos2, mose2, and their mos2xse2(1x) alloys: Ab initio calculations. *Journal of Electronic Materials*, 48 (12):7977–7990, Dec 2019. ISSN 1543-186X. doi: 10.1007/s11664-019-07611-x. URL https://doi.org/10.1007/s11664-019-07611-x.

[6] A.K.M. Newaz, D. Prasai, J.I. Ziegler, D. Caudel, S. Robinson, R.F. Haglund Jr., and K.I. Bolotin. Electrical control of optical properties of monolayer mos2. *Solid State Communications*, 155:49–52, 2013. ISSN 0038-1098. doi: https://doi.org/10.1016/j.ssc.2012.11.010. URL https://www.sciencedirect.com/science/article/pii/S0038109812006205.

[7] Wenxu Zhang, Zhishuo Huang, Wanli Zhang, and Yanrong Li. Two-dimensional semiconductors with possible high room temperature mobility. *Nano Research*,

7(12):1731–1737, Dec 2014. ISSN 1998-0000. doi: 10.1007/s12274-014-0532-x. URL https://doi.org/10.1007/s12274-014-0532-x.

[8] Hüseyin Şar, Ayberk Özden, Buşra Yorulmaz, Cem Sevik, Nihan Kosku Perkgoz, and Feridun Ay. A comparative device performance assesment of cvd grown mos2 and ws2 monolayers. *Journal of Materials Science: Materials in Electronics*, 29 (10):8785–8792, May 2018. ISSN 1573-482X. doi: 10.1007/s10854-018-8895-5. URL https://doi.org/10.1007/s10854-018-8895-5.

[9] Humberto R. Gutiérrez, Nestor Perea-López, Ana Laura Elías, Ayse Berkdemir, Bei Wang, Ruitao Lv, Florentino López-Urías, Vincent H. Crespi, Humberto Terrones, and Mauricio Terrones. Extraordinary room-temperature photoluminescence in triangular ws2 monolayers. *Nano Letters*, 13(8):3447–3454, 2013. doi: 10.1021/nl3026357. URL https://doi.org/10.1021/nl3026357.

[10] Katsuyoshi Kobayashi and Jun Yamauchi. Electronic structure and scanning-tunneling-microscopy image of molybdenum dichalcogenide surfaces. *Phys. Rev. B*, 51:17085–17095, Jun 1995. doi: 10.1103/PhysRevB.51.17085. URL https://link.aps.org/doi/10.1103/PhysRevB.51.17085.

[11] Won Seok Yun, S. W. Han, Soon Cheol Hong, In Gee Kim, and J. D. Lee. Thickness and strain effects on electronic structures of transition metal dichalcogenides: 2h-mX_2 semiconductors (m = mo, w; x = s, se, te). *Phys. Rev. B*, 85:033305, Jan 2012. doi: 10.1103/PhysRevB.85.033305. URL https://link.aps.org/doi/10.1103/PhysRevB.85.033305.

[12] Saptarshi Das, Abhijith Prakash, Ramon Salazar, and Joerg Appenzeller. Toward low-power electronics: Tunneling phenomena in transition metal dichalcogenides. *ACS Nano*, 8(2):1681–1689, 2014. doi: 10.1021/nn406603h. URL https://doi.org/10.1021/nn406603h.

[13] Fu Zhang, Yanfu Lu, Daniel S. Schulman, Tianyi Zhang, Kazunori Fujisawa, Zhong Lin, Yu Lei, Ana Laura Elias, Saptarshi Das, Susan B. Sinnott, and Mauricio Terrones. Carbon doping of ws¡sub¿2¡/sub¿ monolayers: Bandgap reduction and p-type doping transport. *Science Advances*, 5(5):eaav5003, 2019. doi: 10.1126/sciadv.aav5003. URL https://www.science.org/doi/abs/10.1126/sciadv.aav5003.

[14] Ming-Deng Siao, Yung-Chang Lin, Tao He, Meng-Yu Tsai, Kuei-Yi Lee, Shou-Yi Chang, Kuang-I Lin, Yen-Fu Lin, Mei-Yin Chou, Kazu Suenaga, and Po-Wen Chiu. Embedment of multiple transition metal impurities into ws2 monolayer for bandstructure modulation. *Small*, 17(17):2007171, 2021. doi: https://doi.org/10.1002/smll.202007171. URL https://onlinelibrary.wiley.com/doi/abs/10.1002/smll.202007171.

[15] Bruno Schuler, Jun-Ho Lee, Christoph Kastl, Katherine A. Cochrane, Christopher T. Chen, Sivan Refaely-Abramson, Shengjun Yuan, Edo van Veen, Rafael Roldán, Nicholas J. Borys, Roland J. Koch, Shaul Aloni, Adam M. Schwartzberg, D. Frank Ogletree, Jeffrey B. Neaton, and Alexander Weber-Bargioni. How substitutional point defects in two-dimensional ws2 induce charge localization, spin–orbit splitting, and strain. *ACS Nano*, 13(9):10520–10534, 2019. doi: 10.1021/acsnano.9b04611. URL `https://doi.org/10.1021/acsnano.9b04611`.

[16] Namphung Peimyoo, Weihuang Yang, Jingzhi Shang, Xiaonan Shen, Yanlong Wang, and Ting Yu. Chemically driven tunable light emission of charged and neutral excitons in monolayer ws2. *ACS Nano*, 8(11):11320–11329, 2014. doi: 10.1021/nn504196n. URL `https://doi.org/10.1021/nn504196n`.

[17] Kausik Manna, Huin-Ning Huang, Wei-Ting Li, Yao-Huang Ho, and Wei-Hung Chiang. Toward understanding the efficient exfoliation of layered materials by water-assisted cosolvent liquid-phase exfoliation. *Chemistry of Materials*, 28(21): 7586–7593, 2016. doi: 10.1021/acs.chemmater.6b01203. URL `https://doi.org/10.1021/acs.chemmater.6b01203`.

[18] Chinedu Obiakara, Chih-Kai Liao, and Mahmoud A. Mahmoud. Mechanical exfoliation assisted by molecular tweezers for production of sulfur-based semiconducting two-dimensional materials. *Industrial & Engineering Chemistry Research*, 58(31):14170–14179, 2019. doi: 10.1021/acs.iecr.9b03082. URL `https://doi.org/10.1021/acs.iecr.9b03082`.

[19] Hye Yun Jeong, Youngjo Jin, Seok Joon Yun, Jiong Zhao, Jaeyoon Baik, Dong Hoon Keum, Hyun Seok Lee, and Young Hee Lee. Heterogeneous defect domains in single-crystalline hexagonal ws2. *Advanced Materials*, 29(15): 1605043, 2017. doi: https://doi.org/10.1002/adma.201605043. URL `https://onlinelibrary.wiley.com/doi/abs/10.1002/adma.201605043`.

[20] Feifei Lan, Ruixia Yang, Kewei Sun, Zenghua Wang, Ying Zhang, Yingmin Wang, and Hongjuan Cheng. Growth of wafer scale continuous monolayer ws2 film with millimeter grain size. *Vacuum*, 201:111091, 2022. ISSN 0042-207X. doi: https://doi.org/10.1016/j.vacuum.2022.111091. URL `https://www.sciencedirect.com/science/article/pii/S0042207X22002214`.

[21] Matthew R Rosenberger, Hsun-Jen Chuang, Kathleen M McCreary, Connie H Li, and Berend T Jonker. Electrical characterization of discrete defects and impact of defect density on photoluminescence in monolayer ws2. *ACS nano*, 12(2): 1793–1800, 2018. doi: 10.1021/acsnano.7b08566. URL `https://doi.org/10.1021/acsnano.7b08566`.

[22] Ziyu Luo, Weihao Zheng, Nannan Luo, Bo Liu, Biyuan Zheng, Xing Yang, Delang Liang, Junyu Qu, Huawei Liu, Ying Chen, et al. Photoluminescence lightening: Extraordinary oxygen modulated dynamics in ws2 monolayers. *Nano Letters*, 22(5):2112–2119, 2022. doi: 10.1021/acs.nanolett.2c00462. URL https://doi.org/10.1021/acs.nanolett.2c00462.

[23] Michelle Marie S Villamayor, Sajid Husain, Reinier Oropesa-Nuñez, Fredrik OL Johansson, Rebecka Lindblad, Pedro Lourenço, Romain Bernard, Nadine Witkowski, Geoffroy Prévot, Nomi LAN Sorgenfrei, et al. Wafer-sized ws 2 monolayer deposition by sputtering. *Nanoscale*, 14(17):6331–6338, 2022. doi: 10.1039/D1NR08375A. URL https://doi.org/10.1039/D1NR08375A.

[24] Christoph Kastl, Roland J. Koch, Christopher T. Chen, Johanna Eichhorn, Søren Ulstrup, Aaron Bostwick, Chris Jozwiak, Tevye R. Kuykendall, Nicholas J. Borys, Francesca M. Toma, Shaul Aloni, Alexander Weber-Bargioni, Eli Rotenberg, and Adam M. Schwartzberg. Effects of defects on band structure and excitons in ws2 revealed by nanoscale photoemission spectroscopy. *ACS Nano*, 13(2):1284–1291, 2019. doi: 10.1021/acsnano.8b06574. URL https://doi.org/10.1021/acsnano.8b06574.

[25] Joshua A. Robinson and Bruno Schuler. Engineering and probing atomic quantum defects in 2d semiconductors: A perspective. *Applied Physics Letters*, 119 (14):140501, 2021. doi: 10.1063/5.0065185. URL https://doi.org/10.1063/5.0065185.

[26] Yung-Chang Lin, Shisheng Li, Hannu-Pekka Komsa, Li-Jen Chang, Arkady V Krasheninnikov, Goki Eda, and Kazu Suenaga. Revealing the atomic defects of ws2 governing its distinct optical emissions. *Advanced Functional Materials*, 28 (4):1704210, 2018. doi: https://doi.org/10.1002/adfm.201704210. URL https://onlinelibrary.wiley.com/doi/abs/10.1002/adfm.201704210.

[27] KA Cochrane, T Zhang, A Kozhakhmetov, JH Lee, F Zhang, C Dong, JB Neaton, JA Robinson, M Terrones, A Weber Bargioni, et al. Intentional carbon doping reveals ch as an abundant charged impurity in nominally undoped synthetic ws2 and wse2. *2D Materials*, 7(3):031003, 2020. doi: 10.1088/2053-1583/ab8543. URL https://doi.org/10.1088/2053-1583/ab8543.

[28] Sara Barja, Sivan Refaely-Abramson, Bruno Schuler, Diana Y Qiu, Artem Pulkin, Sebastian Wickenburg, Hyejin Ryu, Miguel M Ugeda, Christoph Kastl, Christopher Chen, et al. Identifying substitutional oxygen as a prolific point defect in monolayer transition metal dichalcogenides. *Nature communications*, 10(1): 1–8, 2019. doi: 10.1038/s41467-019-11342-2. URL https://doi.org/10.1038/s41467-019-11342-2.

[29] Yu-Han Wang, Hsin-Mei Ho, Xuan-Long Ho, Li-Syuan Lu, Shang-Hsien Hsieh, Shuei-De Huang, Hsiang-Chih Chiu, Chia-Hao Chen, Wen-Hao Chang, Jonathon David White, et al. Photoluminescence enhancement in ws2 nanosheets passivated with oxygen ions: Implications for selective area doping. *ACS Applied Nano Materials*, 4(11):11693–11699, 2021. doi: 10.1021/acsanm.1c02265. URL https://doi.org/10.1021/acsanm.1c02265.

[30] Bruno Schuler, Diana Y Qiu, Sivan Refaely-Abramson, Christoph Kastl, Christopher T Chen, Sara Barja, Roland J Koch, D Frank Ogletree, Shaul Aloni, Adam M Schwartzberg, et al. Large spin-orbit splitting of deep in-gap defect states of engineered sulfur vacancies in monolayer ws 2. *Physical review letters*, 123(7):076801, 2019. doi: 10.1103/PhysRevLett.123.076801. URL https://link.aps.org/doi/10.1103/PhysRevLett.123.076801.

[31] Jingzhi Shang, Xiaonan Shen, Chunxiao Cong, Namphung Peimyoo, Bingchen Cao, Mustafa Eginligil, and Ting Yu. Observation of excitonic fine structure in a 2d transition-metal dichalcogenide semiconductor. *ACS nano*, 9(1):647–655, 2015. doi: 10.1021/nn5059908. URL https://doi.org/10.1021/nn5059908.

[32] Yongjun Lee, Seok Joon Yun, Youngbum Kim, Min Su Kim, Gang Hee Han, AK Sood, and Jeongyong Kim. Near-field spectral mapping of individual exciton complexes of monolayer ws 2 correlated with local defects and charge population. *Nanoscale*, 9(6):2272–2278, 2017. doi: 10.1039/C6NR08813A. URL http://dx.doi.org/10.1039/C6NR08813A.

[33] Zhenliang Hu, Jose Avila, Xinyun Wang, Jin Feng Leong, Qi Zhang, Yanpeng Liu, Maria C Asensio, Junpeng Lu, Alexandra Carvalho, Chorng Haur Sow, et al. The role of oxygen atoms on excitons at the edges of monolayer ws2. *Nano Letters*, 19(7):4641–4650, 2019. doi: 10.1021/acs.nanolett.9b01670. URL https://doi.org/10.1021/acs.nanolett.9b01670.

[34] Min Su Kim, Seok Joon Yun, Yongjun Lee, Changwon Seo, Gang Hee Han, Ki Kang Kim, Young Hee Lee, and Jeongyong Kim. Biexciton emission from edges and grain boundaries of triangular ws2 monolayers. *ACS nano*, 10(2):2399–2405, 2016. doi: 10.1021/acsnano.5b07214. URL https://doi.org/10.1021/acsnano.5b07214.

[35] Rahul Rao, Hyunil Kim, Nestor Perea-López, Mauricio Terrones, and Benji Maruyama. Interaction of gases with monolayer ws 2: an in situ spectroscopy study. *Nanoscale*, 13(26):11470–11477, 2021. doi: 10.1039/D1NR01483H. URL http://dx.doi.org/10.1039/D1NR01483H.

[36] Changjie Zhou, Weihuang Yang, and Huili Zhu. Mechanism of charge transfer and its impacts on fermi-level pinning for gas molecules adsorbed on monolayer

ws2. *The Journal of chemical physics*, 142(21):214704, 2015. doi: doi.org/10.1063/1.4922049. URL https://doi.org/10.1063/1.4922049.

[37] Hanyu Zhang, Jeremy R Dunklin, Obadiah G Reid, Seok Joon Yun, Sanjini U Nanayakkara, Young Hee Lee, Jeffrey L Blackburn, and Elisa M Miller. Disentangling oxygen and water vapor effects on optoelectronic properties of monolayer tungsten disulfide. *Nanoscale*, 12(15):8344–8354, 2020. doi: 10.1039/C9NR09326E. URL http://dx.doi.org/10.1039/C9NR09326E.

[38] Rahul Rao, Victor Carozo, Yuanxi Wang, Ahmad E Islam, Nestor Perea-Lopez, Kazunori Fujisawa, Vincent H Crespi, Mauricio Terrones, and Benji Maruyama. Dynamics of cleaning, passivating and doping monolayer mos2 by controlled laser irradiation. *2D Materials*, 6(4):045031, 2019. doi: 10.1088/2053-1583/ab33ab. URL https://doi.org/10.1088/2053-1583/ab33ab.

[39] Yuanzheng Li, Jiaxu Yan, Jinping Chen, Tong Yu, Hang Ren, Xiuling Liu, Weizhen Liu, Guochun Yang, Chunxiang Xu, Qiaoliang Bao, et al. Unraveling the synergetic mechanism of physisorption and chemisorption in laser-irradiated monolayer ws2. *Nano Research*, 14(11):4274–4280, 2021. doi: 10.1007/s12274-021-3667-6. URL https://doi.org/10.1007/s12274-021-3667-6.

[40] Ethan C Ahn. 2d materials for spintronic devices. *npj 2D Materials and Applications*, 4(1):1–14, 2020. doi: 10.1038/s41699-020-0152-0. URL https://doi.org/10.1038/s41699-020-0152-0.

[41] Mark A Lukowski, Andrew S Daniel, Caroline R English, Fei Meng, Audrey Forticaux, Robert J Hamers, and Song Jin. Highly active hydrogen evolution catalysis from metallic ws 2 nanosheets. *Energy & Environmental Science*, 7(8):2608–2613, 2014. doi: 10.1039/C4EE01329H. URL http://dx.doi.org/10.1039/C4EE01329H.

[42] Yang Li, Xin Wu, Huabin Zhang, and Jian Zhang. Interface designing over ws2/w2c for enhanced hydrogen evolution catalysis. *ACS Applied Energy Materials*, 1(7):3377–3384, 2018. doi: 10.1021/acsaem.8b00550. URL https://doi.org/10.1021/acsaem.8b00550.

[43] Branimir Radisavljevic, Aleksandra Radenovic, Jacopo Brivio, Valentina Giacometti, and Andras Kis. Single-layer mos2 transistors. *Nature nanotechnology*, 6(3):147–150, 2011. doi: 10.1038/nnano.2010.279. URL https://doi.org/10.1038/nnano.2010.279.

[44] S Thiele, W Kinberger, R Granzner, G Fiori, and F Schwierz. The prospects of transition metal dichalcogenides for ultimately scaled cmos. *Solid-State Electronics*, 143:2–9, 2018. doi: https://doi.org/10.1016/j.sse.2017.11.004. URL https://www.sciencedirect.com/science/article/pii/S0038110117306597.

[45] Zheng Meng, Robert M Stolz, Lukasz Mendecki, and Katherine A Mirica. Electrically-transduced chemical sensors based on two-dimensional nanomaterials. *Chemical reviews*, 119(1):478–598, 2019. doi: 10.1021/acs.chemrev.8b00311. URL https://doi.org/10.1021/acs.chemrev.8b00311.

[46] Nengjie Huo, Shengxue Yang, Zhongming Wei, Shu-Shen Li, Jian-Bai Xia, and Jingbo Li. Photoresponsive and gas sensing field-effect transistors based on multilayer ws2 nanoflakes. *Scientific reports*, 4(1):1–9, 2014. doi: 10.1038/srep05209. URL https://doi.org/10.1038/srep05209.

[47] Di Liu, Zilong Tang, and Zhongtai Zhang. Comparative study on no2 and h2s sensing mechanisms of gas sensors based on ws2 nanosheets. *Sensors and Actuators B: Chemical*, 303:127114, 2020. doi: https://doi.org/10.1016/j.snb.2019.127114. URL https://www.sciencedirect.com/science/article/pii/S0925400519313139.

[48] Yunhan Luo, Chaoying Chen, Kai Xia, Shuihua Peng, Heyuan Guan, Jieyuan Tang, Huiui Lu, Jianhui Yu, Jun Zhang, Yi Xiao, et al. Tungsten disulfide (ws 2) based all-fiber-optic humidity sensor. *Optics express*, 24(8):8956–8966, 2016. doi: 10.1364/OE.24.008956. URL http://opg.optica.org/oe/abstract.cfm?URI=oe-24-8-8956.

[49] D Simon Patrick, P Bharathi, M Krishna Mohan, C Muthamizchelvan, S Harish, and M Navaneethan. Liquid phase exfoliated ws2 nanosheet-based gas sensor for room temperature no2 detection. *Journal of Materials Science: Materials in Electronics*, 33(12):9235–9245, 2022. doi: 10.1007/s10854-021-07246-x. URL https://doi.org/10.1007/s10854-021-07246-x.

[50] Tongxin Chen, Yuewen Sheng, Yingqiu Zhou, Ren-jie Chang, Xiaochen Wang, Hefu Huang, Qianyang Zhang, Linlin Hou, and Jamie H Warner. High photoresponsivity in ultrathin 2d lateral graphene: Ws2: graphene photodetectors using direct cvd growth. *ACS applied materials & interfaces*, 11(6):6421–6430, 2019. doi: 10.1021/acsami.8b20321. URL https://doi.org/10.1021/acsami.8b20321.

[51] Jake D Mehew, Selim Unal, Elias Torres Alonso, Gareth F Jones, Saad Fadhil Ramadhan, Monica F Craciun, and Saverio Russo. Fast and highly sensitive ionic-polymer-gated ws2–graphene photodetectors. *Advanced Materials*, 29(23):1700222, 2017. doi: https://doi.org/10.1002/adma.201700222. URL https://onlinelibrary.wiley.com/doi/abs/10.1002/adma.201700222.

[52] Marco Bernardi, Maurizia Palummo, and Jeffrey C Grossman. Extraordinary sunlight absorption and one nanometer thick photovoltaics using two-

dimensional monolayer materials. *Nano letters*, 13(8):3664–3670, 2013. doi: 10.1021/nl401544y. URL https://doi.org/10.1021/nl401544y.

[53] Jinzi Ding, Ailing Feng, Xiaodong Li, Shijiu Ding, Liang Liu, and Wei Ren. Properties, preparation, and application of tungsten disulfide: A review. *Journal of Physics D: Applied Physics*, 54(17):173002, 2021. doi: 10.1088/1361-6463/abd9e8. URL https://doi.org/10.1088/1361-6463/abd9e8.

[54] Sanghyun Jo, Nicolas Ubrig, Helmuth Berger, Alexey B Kuzmenko, and Alberto F Morpurgo. Mono-and bilayer ws2 light-emitting transistors. *Nano letters*, 14(4):2019–2025, 2014. doi: 10.1021/nl500171v. URL https://doi.org/10.1021/nl500171v.

[55] Weihuang Yang, Jingzhi Shang, Jianpu Wang, Xiaonan Shen, Bingchen Cao, Namphung Peimyoo, Chenji Zou, Yu Chen, Yanlong Wang, Chunxiao Cong, et al. Electrically tunable valley-light emitting diode (vled) based on cvd-grown monolayer ws2. *Nano letters*, 16(3):1560–1567, 2016. doi: 10.1021/acs.nanolett.5b04066. URL https://doi.org/10.1021/acs.nanolett.5b04066.

[56] Yu Ye, Zi Jing Wong, Xiufang Lu, Xingjie Ni, Hanyu Zhu, Xianhui Chen, Yuan Wang, and Xiang Zhang. Monolayer excitonic laser. *Nature Photonics*, 9(11):733–737, 2015. doi: 10.1038/nphoton.2015.197. URL https://doi.org/10.1038/nphoton.2015.197.

[57] Han-Sen Zhong, Hui Wang, Yu-Hao Deng, Ming-Cheng Chen, Li-Chao Peng, Yi-Han Luo, Jian Qin, Dian Wu, Xing Ding, Yi Hu, et al. Quantum computational advantage using photons. *Science*, 370(6523):1460–1463, 2020. doi: 10.1126/science.abe8770. URL https://www.science.org/doi/abs/10.1126/science.abe8770.

[58] Peter Lodahl, Sahand Mahmoodian, and Søren Stobbe. Interfacing single photons and single quantum dots with photonic nanostructures. *Reviews of Modern Physics*, 87(2):347, 2015. doi: 10.1103/RevModPhys.87.347. URL https://link.aps.org/doi/10.1103/RevModPhys.87.347.

[59] Chitraleema Chakraborty, Nick Vamivakas, and Dirk Englund. Advances in quantum light emission from 2d materials. *Nanophotonics*, 8(11):2017–2032, 2019. doi: doi:10.1515/nanoph-2019-0140. URL https://doi.org/10.1515/nanoph-2019-0140.

[60] Brain spect scanning at sierra tucson increases diagnostic capabilities and motivates patients. URL http://www.prweb.com/releases/2009/tucson/prweb2737304.htm.

[61] Curty M. Lo H.K. and Tamaki K. Secure quantum key distribution. *Nature Physics*, 2014. doi: 10.1038/nphoton.2014.149. URL https://www.nature.com/articles/nphoton.2014.149.

[62] David M Toyli, Christoph D Weis, Gregory D Fuchs, Thomas Schenkel, and David D Awschalom. Chip-scale nanofabrication of single spins and spin arrays in diamond. *Nano letters*, 10(8):3168–3172, 2010. doi: 10.1021/nl102066q. URL https://doi.org/10.1021/nl102066q.

[63] Julian Klein, Lukas Sigl, Samuel Gyger, Katja Barthelmi, Matthias Florian, Sergio Rey, Takashi Taniguchi, Kenji Watanabe, Frank Jahnke, Christoph Kastl, et al. Scalable single-photon sources in atomically thin mos2. *arXiv preprint arXiv:2002.08819*, 2020. doi: 10.48550/ARXIV.2002.08819. URL https://arxiv.org/abs/2002.08819.

[64] Bruno Schuler, Katherine A Cochrane, Christoph Kastl, Edward S Barnard, Edward Wong, Nicholas J Borys, Adam M Schwartzberg, D Frank Ogletree, F Javier García de Abajo, and Alexander Weber-Bargioni. Electrically driven photon emission from individual atomic defects in monolayer ws2. *Science advances*, 6(38):eabb5988, 2020. doi: 10.1126/sciadv.abb5988. URL https://www.science.org/doi/abs/10.1126/sciadv.abb5988.

[65] Shogo Sasaki, Yu Kobayashi, Zheng Liu, Kazutomo Suenaga, Yutaka Maniwa, Yuhei Miyauchi, and Yasumitsu Miyata. Growth and optical properties of nb-doped ws2 monolayers. *Applied Physics Express*, 9(7):071201, 2016. doi: 10.7567/apex.9.071201. URL https://doi.org/10.7567/apex.9.071201.

[66] M. Born and R. Oppenheimer. Zur quantentheorie der molekeln. *Annalen der Physik*, 389(20):457–484, 1927. doi: https://doi.org/10.1002/andp.19273892002. URL https://onlinelibrary.wiley.com/doi/abs/10.1002/andp.19273892002.

[67] P. Hohenberg and W. Kohn. Inhomogeneous electron gas. *Phys. Rev.*, 136:B864–B871, Nov 1964. doi: 10.1103/PhysRev.136.B864. URL https://link.aps.org/doi/10.1103/PhysRev.136.B864.

[68] W. Kohn and L. J. Sham. Self-consistent equations including exchange and correlation effects. *Phys. Rev.*, 140:A1133–A1138, Nov 1965. doi: 10.1103/PhysRev.140.A1133. URL https://link.aps.org/doi/10.1103/PhysRev.140.A1133.

[69] L. H. Thomas. The calculation of atomic fields. *Mathematical Proceedings of the Cambridge Philosophical Society*, 23(5):542–548, 1927. doi: 10.1017/S0305004100011683. URL https://www.cambridge.org/core/article/calculation-of-atomic-fields/ADCA3D21D0FACD7077B5FDBB7F3B3F3A.

[70] E. Fermi. Un metodo statistico per la determinazione di alcune priorietá dell'atomo. *Rend. Accad. Naz. Lincei*, 6:602, 1927.

[71] P. A. M. Dirac. Note on exchange phenomena in the thomas-fermi atom. *Proc. Cambridge Phil. Roy. Soc.*, 26:376, 1930.

[72] Richard M. Martin. *Electronic Structure: Basic Theory and Practical Methods*. Cambridge University Press, 2004. doi: 10.1017/CBO9780511805769.

[73] D. M. Ceperley and B. J. Alder. Ground state of the electron gas by a stochastic method. *Phys. Rev. Lett.*, 45:566–569, Aug 1980. doi: 10.1103/PhysRevLett.45.566. URL `https://link.aps.org/doi/10.1103/PhysRevLett.45.566`.

[74] J. P. Perdew and Alex Zunger. Self-interaction correction to density-functional approximations for many-electron systems. *Phys. Rev. B*, 23:5048–5079, May 1981. doi: 10.1103/PhysRevB.23.5048. URL `https://link.aps.org/doi/10.1103/PhysRevB.23.5048`.

[75] John P. Perdew and Wang Yue. Accurate and simple density functional for the electronic exchange energy: Generalized gradient approximation. *Phys. Rev. B*, 33:8800–8802, Jun 1986. doi: 10.1103/PhysRevB.33.8800. URL `https://link.aps.org/doi/10.1103/PhysRevB.33.8800`.

[76] John P. Perdew, Kieron Burke, and Matthias Ernzerhof. Generalized gradient approximation made simple. *Phys. Rev. Lett.*, 77:3865–3868, Oct 1996. doi: 10.1103/PhysRevLett.77.3865. URL `https://link.aps.org/doi/10.1103/PhysRevLett.77.3865`.

[77] Denis Kochan, Susanne Irmer, and Jaroslav Fabian. Model spin-orbit coupling hamiltonians for graphene systems. *Physical Review B*, 95(16):165415, 2017. doi: 10.1103/PhysRevB.95.165415. URL `https://link.aps.org/doi/10.1103/PhysRevB.95.165415`.

[78] Pekka Pyykko. Relativistic effects in structural chemistry. *Chemical Reviews*, 88 (3):563–594, 1988. doi: 10.1021/cr00085a006. URL `https://doi.org/10.1021/cr00085a006`.

[79] H Hellmann. *Einführung in die quantumchemie*. 1937.

[80] R. P. Feynman. Force in molecules. *Phys. Rev.*, 56:340–343, 1939.

[81] Paolo Giannozzi, Stefano Baroni, Nicola Bonini, Matteo Calandra, Roberto Car, Carlo Cavazzoni, Davide Ceresoli, Guido L Chiarotti, Matteo Cococcioni, Ismaila Dabo, Andrea Dal Corso, Stefano de Gironcoli, Stefano Fabris, Guido Fratesi, Ralph Gebauer, Uwe Gerstmann, Christos Gougoussis, Anton Kokalj, Michele

Lazzeri, Layla Martin-Samos, Nicola Marzari, Francesco Mauri, Riccardo Mazzarello, Stefano Paolini, Alfredo Pasquarello, Lorenzo Paulatto, Carlo Sbraccia, Sandro Scandolo, Gabriele Sclauzero, Ari P Seitsonen, Alexander Smogunov, Paolo Umari, and Renata M Wentzcovitch. QUANTUM ESPRESSO: a modular and open-source software project for quantum simulations of materials. *Journal of Physics: Condensed Matter*, 21(39):395502, sep 2009. doi: 10.1088/0953-8984/21/39/395502. URL https://doi.org/10.1088/0953-8984/21/39/395502.

[82] D. R. Hamann, M. Schlüter, and C. Chiang. Norm-conserving pseudopotentials. *Phys. Rev. Lett.*, 43:1494–1497, Nov 1979. doi: 10.1103/PhysRevLett.43.1494. URL https://link.aps.org/doi/10.1103/PhysRevLett.43.1494.

[83] G. B. Bachelet, D. R. Hamann, and M. Schlüter. Pseudopotentials that work: From h to pu. *Phys. Rev. B*, 26:4199–4228, Oct 1982. doi: 10.1103/PhysRevB.26.4199. URL https://link.aps.org/doi/10.1103/PhysRevB.26.4199.

[84] Hendrik J. Monkhorst and James D. Pack. Special points for brillouin-zone integrations. *Phys. Rev. B*, 13:5188–5192, Jun 1976. doi: 10.1103/PhysRevB.13.5188. URL https://link.aps.org/doi/10.1103/PhysRevB.13.5188.

[85] Hannes Jonsson, Greg Mills, and Karsten W. Jacobsen. Nudged elastic band method for finding minimum energy paths of transitions. pages 385–404. doi: 10.1142/9789812839664_0016. URL https://www.worldscientific.com/doi/abs/10.1142/9789812839664_0016.

[86] Graeme Henkelman, Blas P Uberuaga, and Hannes Jónsson. A climbing image nudged elastic band method for finding saddle points and minimum energy paths. *The Journal of chemical physics*, 113(22):9901–9904, 2000. doi: 10.1063/1.1329672. URL https://doi.org/10.1063/1.1329672.

[87] P Giannozzi, O Andreussi, T Brumme, O Bunau, M Buongiorno Nardelli, M Calandra, R Car, C Cavazzoni, D Ceresoli, M Cococcioni, N Colonna, I Carnimeo, A Dal Corso, S de Gironcoli, P Delugas, R A DiStasio, A Ferretti, A Floris, G Fratesi, G Fugallo, R Gebauer, U Gerstmann, F Giustino, T Gorni, J Jia, M Kawamura, H-Y Ko, A Kokalj, E Küçükbenli, M Lazzeri, M Marsili, N Marzari, F Mauri, N L Nguyen, H-V Nguyen, A Otero de-la Roza, L Paulatto, S Poncé, D Rocca, R Sabatini, B Santra, M Schlipf, A P Seitsonen, A Smogunov, I Timrov, T Thonhauser, P Umari, N Vast, X Wu, and S Baroni. Advanced capabilities for materials modelling with quantum ESPRESSO. *Journal of Physics: Condensed Matter*, 29(46):465901, oct 2017. doi: 10.1088/1361-648x/aa8f79. URL https://doi.org/10.1088/1361-648x/aa8f79.

[88] Paolo Giannozzi, Oscar Baseggio, Pietro Bonfà, Davide Brunato, Roberto Car, Ivan Carnimeo, Carlo Cavazzoni, Stefano de Gironcoli, Pietro Delugas, Fabrizio

Ferrari Ruffino, Andrea Ferretti, Nicola Marzari, Iurii Timrov, Andrea Urru, and Stefano Baroni. Quantum espresso toward the exascale. *The Journal of Chemical Physics*, 152(15):154105, 2020. doi: 10.1063/5.0005082. URL https://doi.org/10.1063/5.0005082.

[89] Stefan Grimme, Jens Antony, Stephan Ehrlich, and Helge Krieg. A consistent and accurate ab initio parametrization of density functional dispersion correction (dft-d) for the 94 elements h-pu. *The Journal of Chemical Physics*, 132(15):154104, 2010. doi: 10.1063/1.3382344. URL https://doi.org/10.1063/1.3382344.

[90] D. R. Hamann. Optimized norm-conserving vanderbilt pseudopotentials. *Phys. Rev. B*, 88:085117, Aug 2013. doi: 10.1103/PhysRevB.88.085117. URL https://link.aps.org/doi/10.1103/PhysRevB.88.085117.

[91] W.J. Schutte, J.L. De Boer, and F. Jellinek. Crystal structures of tungsten disulfide and diselenide. *Journal of Solid State Chemistry*, 70(2):207–209, 1987. ISSN 0022-4596. doi: https://doi.org/10.1016/0022-4596(87)90057-0. URL https://www.sciencedirect.com/science/article/pii/0022459687900570.

[92] A Klein, S Tiefenbacher, V Eyert, C Pettenkofer, and W Jaegermann. Electronic properties of ws2 monolayer films. *Thin Solid Films*, 380(1):221–223, 2000. ISSN 0040-6090. doi: https://doi.org/10.1016/S0040-6090(00)01510-8. URL https://www.sciencedirect.com/science/article/pii/S0040609000015108.

[93] Luqing Wang, Alex Kutana, and Boris I. Yakobson. Many-body and spin-orbit effects on direct-indirect band gap transition of strained monolayer mos2 and ws2. *Annalen der Physik*, 526(9-10):L7–L12, 2014. doi: https://doi.org/10.1002/andp.201400098. URL https://onlinelibrary.wiley.com/doi/abs/10.1002/andp.201400098.

[94] A. Klein, S. Tiefenbacher, V. Eyert, C. Pettenkofer, and W. Jaegermann. Electronic band structure of single-crystal and single-layer ws_2 : influence of interlayer van der waals interactions. *Phys. Rev. B*, 64:205416, Nov 2001. doi: 10.1103/PhysRevB.64.205416. URL https://link.aps.org/doi/10.1103/PhysRevB.64.205416.

[95] Julia Gusakova, Xingli Wang, Li Lynn Shiau, Anna Krivosheeva, Victor Shaposhnikov, Victor Borisenko, Vasilii Gusakov, and Beng Kang Tay. Electronic properties of bulk and monolayer tmds: Theoretical study within dft framework (gvj-2e method). *physica status solidi (a)*, 214(12):1700218, 2017. doi: https://doi.org/10.1002/pssa.201700218. URL https://onlinelibrary.wiley.com/doi/abs/10.1002/pssa.201700218.

[96] Drew W. Latzke, Wentao Zhang, Aslihan Suslu, Tay-Rong Chang, Hsin Lin, Horng-Tay Jeng, Sefaattin Tongay, Junqiao Wu, Arun Bansil, and Alessandra Lanzara. Electronic structure, spin-orbit coupling, and interlayer interaction in bulk mos_2 and ws_2. *Phys. Rev. B*, 91:235202, Jun 2015. doi: 10.1103/PhysRevB.91.235202. URL https://link.aps.org/doi/10.1103/PhysRevB.91.235202.

[97] Y. C. Cheng, Z. Y. Zhu, M. Tahir, and U. Schwingenschlögl. Spin-orbit–induced spin splittings in polar transition metal dichalcogenide monolayers. *EPL (Europhysics Letters)*, 102(5):57001, jun 2013. doi: 10.1209/0295-5075/102/57001. URL https://doi.org/10.1209/0295-5075/102/57001.

[98] SB Zhang and John E Northrup. Chemical potential dependence of defect formation energies in gaas: Application to ga self-diffusion. *Physical review letters*, 67(17):2339, 1991. doi: 10.1103/PhysRevLett.67.2339. URL https://link.aps.org/doi/10.1103/PhysRevLett.67.2339.

[99] Mattia Salomone, Michele Re Fiorentin, Giancarlo Cicero, and Francesca Risplendi. Point defects in two-dimensional indium selenide as tunable single-photon sources. *The Journal of Physical Chemistry Letters*, 12(45):10947–10952, 2021. doi: 10.1021/acs.jpclett.1c02912. URL https://doi.org/10.1021/acs.jpclett.1c02912. PMID: 34735143.

[100] Saboura Salehi and Alireza Saffarzadeh. Atomic defect states in monolayers of mos2 and ws2. *Surface Science*, 651:215–221, 2016. ISSN 0039-6028. doi: https://doi.org/10.1016/j.susc.2016.05.003. URL https://www.sciencedirect.com/science/article/pii/S0039602816301686.

[101] Chih-Pin Lu, Guohong Li, Jinhai Mao, Li-Min Wang, and Eva Y. Andrei. Bandgap, mid-gap states, and gating effects in mos2. *Nano Letters*, 14(8):4628–4633, 2014. doi: 10.1021/nl501659n. URL https://doi.org/10.1021/nl501659n.

[102] Youngho Kang and Seungwu Han. An origin of unintentional doping in transition metal dichalcogenides: the role of hydrogen impurities. *Nanoscale*, 9:4265–4271, 2017. doi: 10.1039/C6NR08555E. URL http://dx.doi.org/10.1039/C6NR08555E.

[103] Florentino Lopez-Urias, Ana Laura Elias, Nestor Perea-Lopez, Humberto R Gutierrez, Mauricio Terrones, and Humberto Terrones. Electronic, magnetic, optical, and edge-reactivity properties of semiconducting and metallic ws2 nanoribbons. *2D Materials*, 2(1):015002, 2014. doi: 10.1088/2053-1583/2/1/015002. URL https://doi.org/10.1088/2053-1583/2/1/015002.

[104] F Fabbri, F Dinelli, S Forti, L Sementa, S Pace, G Piccinini, A Fortunelli, C Coletti, and P Pingue. Edge defects promoted oxidation of monolayer ws2 synthesized on epitaxial graphene. *The Journal of Physical Chemistry C*, 124(16): 9035–9044, 2020. doi: 10.1021/acs.jpcc.0c00350. URL `https://doi.org/10.1021/acs.jpcc.0c00350`.

[105] Viet Q Bui, Tan-Tien Pham, Duy A Le, Cao Minh Thi, and Hung M Le. A first-principles investigation of various gas (co, h2o, no, and o2) absorptions on a ws2 monolayer: stability and electronic properties. *Journal of Physics: Condensed Matter*, 27(30):305005, 2015. doi: 10.1088/0953-8984/27/30/305005. URL `https://doi.org/10.1088/0953-8984/27/30/305005`.